DEVELOPMENT AND TESTING OF A GALLIUM ELECTROMAGNETIC (GEM) THRUSTER

BY

ROBERT EDWARD THOMAS II

DISSERTATION

Submitted in partial fulfillment of the requirements
for the degree of Doctor of Philosophy in Aerospace Engineering
in the Graduate College of the
University of Illinois at Urbana-Champaign, 2010

Urbana, Illinois

Doctoral Committee:

Professor Rodney Burton, Chair
Professor Nick Glumac
Professor Greg Elliott
Professor George Miley
Dr. Kurt A. Polzin

Abstract

An ablative, quasi-steady electromagnetic plasma accelerator is tested to quantify various characteristics of its operation. An array of diagnostics are used to characterize a gallium plasma produced by an arc discharge with current levels in the range of 5.6 - 22.6 kA. Discharge current and arc voltage measurements yield arc impedance values in the range of 6 - 7 mΩ at peak current. The absence of high-frequency oscillations in the arc voltage trace indicates lack of the "onset" condition often seen in MPD arcs, suggesting that a sufficient number of charge carriers are present for current conduction. It is found that the mass bit varies quadratically with the discharge current which yields a calculated exhaust velocity of 20 km/s. A perpendicular probe and time-of-flight method yield exhaust velocities in the range of 15-22 km/s that is found to be invariant with the discharge current. Macroparticle ejection is unavoidable when testing with a central anode; this is possibly due to the presence of high-current density anode spots present on the gallium surface. A spatially and temporally broad spectroscopic survey in the 220-520 nm range is used to determine which species are present in the plasma. The spectra show that neutral, singly, and doubly ionized gallium atomic and ionic species are present in the discharge. Axial triple Langmuir probe measurements yield electron temperatures in the range of 0.8 - 3.6 eV and electron densities in the range of 8×10^{20} to 2×10^{22} m^{-3}. The plasma expands isentropically with divergence half-angles in the range of 16 - 20°. Spatially resolved magnetic field probe data reveals a symmetric arc discharge with no evidence of the current spoking instability. A power balance is coupled with a sheath model to yield values of the electric field, temperature, and current density at the surface of the cathode.

Acknowledgements

I would like to thank Dr. Rodney Burton, who provided valuable insight into many aspects of scientific investigation and communication, making me more prepared for my future research endeavors. I would like to extend a huge thanks to Dr. Kurt Polzin who served as a research co-advisor and contributed a vast body of knowledge to the research. Thanks to the rest of my Ph.D. committee: Dr. George Miley, Dr. Nick Glumac, and Dr. Greg Elliot. A special thanks to Dr. Glumac for providing his knowledge and spectroscopy equipment to the project. Thanks to Dr. James Polk for providing assistance to my cathode spot calculations. I would like to also acknowledge Jon Frus, who supplied electronic support and Dr. Jason Cassibry who provided equilibrium calculations. A big thanks to Matt Giacomi for lending his design expertise and to Julia Laystrom for proof-reading my dissertation. The entire Aerospace Engineering staff is thanked. Kent Elam, David Foley, and Greg Milner provided mechanical support, and Staci Tankersley and Diane Jeffers provided immense help throughout my tenure as a grad student. Finally, I would like to thank my U of M mentors, Dr. Alec Gallimore and Dr. Mitchell Walker. Support for the research was provided by the Alabama and Illinois Space Grant Consortium, and the NASA GSRP Fellowship program.

Table of Contents

List of Figures

List of Tables

Nomenclature

α	Charge carrier parameter
β	Empirical parameter relating mass bit to discharge current
χ	Non-dimensional potential $e(\phi - \phi_p)/kT_e$
η	Resistivity, Ω-m
f	Frequency, Hz
Γ	Atomic mass flux [m^{-2} s^{-1}]
μ_o	Permeability of free space [H-m^{-1}]
ϕ_p	Space Potential [V]
ϕ_w	Work function [eV]
ψ	Current Action Integral [A^2-s]
ρ	Density [kg-m^{-3}]
σ	Stefan Boltzmann constant [W m^{-2} K^{-4}]
A_p	Probe Area [m^2]
c_p	Specific heat [J kg^{-1} K^{-1}]
D	Electron Tunneling Probability

E	Electric field [V-m^{-1}]
e	Elementary charge [C]
E_r	Erosion rate [μg/C]
h_{vap}	Enthalpy of Vaporization [J]
I	Discharge current [A]
I_{sp}	Specific Impulse [s]
j_e	Electron Current Density [A-m^{-2}]
k	Boltzmann's constant [J/K]
L	Inductance [H]
m_i	Ion mass [kg]
N	Electron Supply Function
R	Thruster radius [m]
R_L	Larmor radius [m]
T	Temperature [K]
t	Time [s]
u_e	exhaust velocity [m-s^{-1}]
$v(y)$	Elliptical function
V_{arc}	Arc Voltage [V]
Z	Ion charge state
Z_{arc}	Arc Impedance [mΩ]

Chapter 1

Introduction

1.1 MPD Thrusters

Magnetoplasmadynamic (MPD) thrusters are electromagnetic accelerators that rely on kiloampere-level currents and magnetic fields to accelerate propellant to high velocities (1-10 km/s). In typical self-field MPD thrusters, a gaseous propellant is fed into a discharge chamber and is ionized by a high-current arc struck between coaxial electrodes. A self-induced azimuthal magnetic field interacts with the current, producing an axial Lorentz body force, which accelerates the propellant for thrust. A schematic of the MPD thruster illustrating the electromagnetic force interactions is shown in Fig. 1.1 [1].

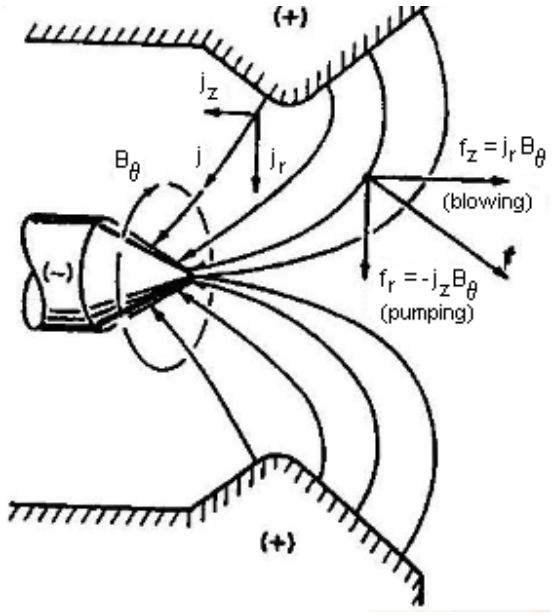

Figure 1.1: Schematic of MPD thruster.

MPD thrusters provide a wide range of exhaust velocities and high thrust densities ($\mathcal{O}$ 10^5 N/m^2) that make them potentially attractive for a wide range of space missions. The ability to generate high thrust densities reduces the number of thrusters required to perform a given mission and relieves the system complexity associated with thruster arrays. A comparison of thrust densities and thrust areas for several different high-power systems operating at a baseline of 1 MW are shown in Table 1.1. While ion and Hall thrusters require 10 m^2 per MW, electromagnetic thrusters such as the MPD and pulsed inductive thruster (PIT) are considerably smaller. Though the arcjet also has a high thrust density, its specific impulse is only 1000 seconds because the propellant is accelerated through gasdynamic expansion.

Table 1.1: Comparison of high-power thruster types.

Thruster Type	Acc. Mechanism	Isp [sec]	T/A $[N/m]^2$	Area $[m^2]$ at 1 MW
Ion	E-field	4000	5	10
Hall	E, B-fields	4000	5	10
MPD	j × B	4000	150	0.3
PIT	j × B	4000	50	1.0
H_2 Arcjet	gasdynamic	1000	150	0.3

Studies have concluded that MPD propulsion systems could be used for attitude control and station keeping of very large space structures, cost-effective cargo transport to lunar and Mars bases, asteroid and outer planet sample return, deep space robotic exploration, and piloted missions to Mars and the outer planets [2, 3, 4, 5].

MPD thrusters have been operated in both steady-state and pulsed quasi-steady modes. The quasi-steady mode has been motivated by the fact that the thrust scales with the discharge current squared, and better performance is attained at higher power levels. Unfortunately, in most cases, thruster efficiencies above 40% have rarely been obtained. The low efficiencies can largely be attributed to frozen flow and plasma sheath losses. Additionally, electrode erosion, which is enhanced at higher power levels, is the chief lifetime issue. The gallium electromagnetic (GEM) thruster development was motivated by a need for a high efficiency thruster that did not suffer from life-limiting electrode erosion.

1.2 GEM Thruster Inception

The GEM thruster was initially conceived as a pulsed multi-stage thruster (Fig. 1.2). In this design, liquid gallium is pumped through a porous tungsten electrode, coating the surface with a thin layer of liquid. A pulsed discharge ($\mathcal{O}$ (10-50) J/pulse) in the first stage vaporizes and ionizes the liquid gallium surface layer, ejecting it into the second stage. A high-energy ($\mathcal{O}$ (500-2000) J/pulse) discharge begins once the gallium plasma from the first stage reaches the outer electrode, effectively shorting it to the inner electrode. A current sheet forms and the Lorentz force accelerates most of the propellant in the axial direction. The first stage (20 Joule) proof-of-concept experiments are presented in Appendix A.

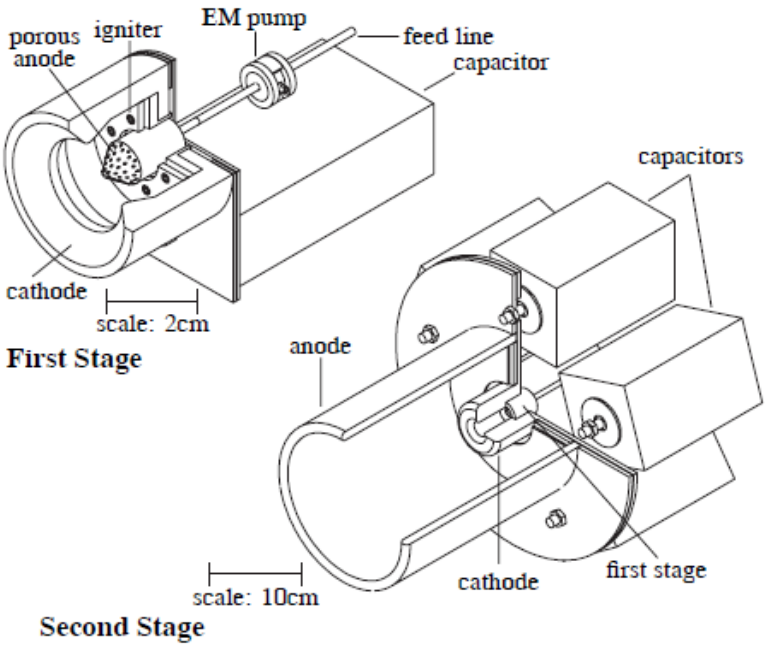

Figure 1.2: Schematic illustrations of a two-stage gallium electromagnetic thruster.

It should be noted that several experimental changes were ultimately made in the present experiment to simplify the testing apparatus as described above. A solid gallium electrode was used as opposed to a continuously fed liquid gallium electrode. This eliminated the need for matching the liquid metal feed rate to the pulse rate and allowed for measurement of the

mass bit. It also allowed the physical of examination of the gallium electrode after firings. The enthalpy of fusion is several orders of magnitude less than the enthalpy of vaporization, so the phase difference (solid vs. liquid) is not expected to significantly alter the results. Heat conduction calculations (Chapter 3) indicate that the gallium electrode melts within microseconds of the discharge initiation. The multi-stage design was also eliminated and a spark igniter was used to trigger the discharge. The rest of the design changes are discussed in later chapters.

1.3 Motivation and Advantages

1.3.1 Physical Properties of Gallium

A number of electric thrusters have used metallic elements as propellants in the past. These have included lithium-fed thrusters [6, 7], mercury [8, 9], cesium [10] and indium-fed electrostatic thrusters (ion engines and field emission electric propulsion) [11], and bismuth-fed Hall thrusters [12, 13]. The physical properties of gallium lead us to believe that it may be a very good propellant option in an electromagnetic accelerator. The most beneficial of these properties are as follows.

1. *Non-toxic and easily handled*: The element gallium is plentiful as a by-product of coal and bauxite processing. It is also relatively safe and easy to handle. Toxicity has limited the application of other promising liquid metal propellants (e.g., mercury, cesium) because of the hazards associated with laboratory testing and environmental contamination. Similarly, some attractive metallic propellants, such as lithium, are highly reactive and pose a fire and explosion hazard. The ease with which gallium can be handled greatly simplifies testing and validation procedures relative to the more reactive metals listed above. While gallium does alloy with and dissolve some metals (copper, aluminum), it has been observed that 316L stainless steel contains it without degradation.

2. *Storability*: Gallium has a density of 5.91 kg/liter (an order of magnitude more than

supercritical xenon), a melting point of 30 °C, and a boiling point of 2400 °C giving it the largest liquid range of any element. This compares to a melting point of 271 °C and a boiling point of 1560 °C for bismuth. Gallium may be stored as either a solid or dense liquid, requiring only minimal tankage mass. The temperature range over which gallium remains a liquid implies that minimal thermal management is required, and any leakage or boil-off losses should be negligible. Its high density leads to low storage volume, and because it is electrically conductive, propellant flow can be controlled using electromagnetic pumps [14].

3. *Ionization Potential*: The first ionization potential of gallium is 6.0 eV while the second ionization potential is 20.5 eV, implying that the plasma can remain singly ionized at low temperature, minimizing the losses associated with the creation of multiply-charged ions.

4. *High molecular weight*: The molecular weight of gallium is 69.7 gm/mole, which when combined with the low first ionization potential helps to predict low frozen flow and sheath losses, the primary loss mechanisms in an electromagnetic thruster.

1.3.2 Mitigation of Critical Issues

A gallium-fed pulsed accelerator may circumvent issues that are inherent to steady-state thrusters presently under development. More specifically, the issues we seek to address are:

1. *Electrode erosion*: The high temperature levels inherent to arc discharges cause evaporation, and consequently long-term degradation, of the metallic electrodes. The GEM thruster is designed to use electrode erosion as an intrinsic aspect of its operation rather than viewing it as an unavoidable, detrimental side effect. Since both the current conduction path and the propellant source are the molten metal covering the electrode surface, we are, in essence, using electrode erosion products as the propellant. Previous investigators have used tin and aluminum foil to protect the underlying cathode from erosion [15].

2. *Propellant injection*: The GEM thruster electrode is ablated to inject propellant. This injection mode eliminates a pulsed valve, which currently cannot operate reliably in a high temperature environment for 10^{10} pulses (which is the number required for outer-planetary

missions) lasting 100 μs each. As demonstrated experimentally in this dissertation, the mass bit can be controlled by changing either the geometry of the thruster or the discharge current.

3. *Current switching*: Gas-fed pulsed plasma thrusters (GFPPTs) and quasi-steady MPD thrusters require a high-speed, high-current switch to electrically isolate the discharge chamber from a capacitor bank prior to discharge initiation. As with the valves, the performance requirements on the high-current switches are strenuous: current rise rates of $\mathcal{O}$ (10^{11}) A/sec, peak current levels of $\mathcal{O}$ $(10^4 - 10^5)$ A and lifetimes of $\mathcal{O}$ $(10^9 - 10^{10})$ pulses. Current state-of-the-art switches, including solid state devices, cannot meet these specifications. The demands for a high-current switch are alleviated in the two-stage scheme, where the lower energy, lower current ($\mathcal{O}$ $(10^2 - 10^3)$ A) first-stage pulse can be switched using current state-of-the-art technology. The high-energy second stage is self-switched when the gallium plasma from the first stage bridges the gap between the inner and outer electrodes. The present experiment uses a spark igniter to trigger the discharge, eliminating the need for a high-current PFN switch.

4. *Facility requirements*: Another beneficial property of gallium is that it exists as a low vapor pressure liquid over a wide range of temperatures, which means that it can be condensed (pumped) on simple, water-cooled plates during thruster testing under vacuum. This type of system can be operated at relatively low-cost (both in terms of facility and propellant cost) for long periods of time. This is a significant advantage when compared to the facility requirements and costs associated with operating large cryopumps for lifetime testing and validation of high-power, gas-fed thrusters (e.g. xenon-fed Hall thrusters) for long duration (e.g. ten year) missions.

1.4 Dissertation Overview

The motivation of this research is to ascertain the basic behavior of gallium in a high-current arc discharge and to determine its utility as an electromagnetic thruster propellant. The mass

ablated per pulse and voltage-current characteristics of the discharge are measured. The voltage, current, and mass bit data are used to calculate the exhaust velocity and estimate the thruster efficiency. Emission spectroscopy is used to find the ionic species present in the discharge. A triple Langmuir probe and magnetic field probe are used to find time-resolved values of the electron temperature, density and magnetic field. A crossed electrostatic and time-of-flight probe are used to measure the exhaust velocity in the plume of the thruster. A power balance model is used to predict the sheath properties at the cathode surface and estimate the fraction of current carried by the ions.

The outline of the dissertation is as follows. The next chapter contains a brief review of MPD thruster performance and the scaling relations of previously developed ablative electromagnetic thrusters are also discussed. The following chapter details the testing facilities, thruster design and pulse forming network (PFN) used for the present experiment. The following two chapters present the data and numerical analysis. The dissertation is completed by the conclusions and recommendations for further studies.

Chapter 2

MPD Thruster Review and Electromagnetic Scaling Relations

2.1 Introduction

This chapter contains a comparison of the propellant injection method and thruster efficiency of previously developed electromagnetic thrusters (EMTs). A current conduction parameter is defined and the ion Larmor radius is discussed in connection with the thruster efficiency. The electromagnetic scaling relations are reviewed and then applied to previously developed ablative thrusters.

2.2 Mass Injection Comparison

A key feature of interest in the operation of the GEM thruster is that of mass injection. Previous electromagnetic accelerators have operated in various modes, which can be classified by the injection scheme of the propellant. The detonation (snowplow) acceleration mode is established when the thruster barrel is pre-filled with gas and a moving current sheet accelerates the propellant. Gas-fed deflagration MPDs employ a stationary $\mathbf{j} \times \mathbf{B}$ force distribution, such that the propellant is fed from the back, ionized, and then pumped through the current sheet in a relatively efficient acceleration process. In both solid-fed pulsed plasma thrusters (PPT) and the Teflon MPD, insulator material is ablated and entrained in an accelerating current sheet to produce thrust. A literature review reveals that only one other thruster has operated by purposely ablating the electrode for propellant, the graphite MPD [16]. In both the graphite MPD and the GEM thruster, the central electrode is vaporized by the dis-

charge current to provide the ionized material, and the arc thus controls the mass flow rate. A summary of various accelerators along with their corresponding injection schemes is given in Table 2.1. Also tabulated is the arc impedance Z_{arc}, which is calculated by dividing the arc voltage (the potential difference across the electrodes during the pulse) by the discharge current.

Table 2.1: Comparison of pulsed coaxial EM accelerator injection modes.

Accelerator Type	Propellant	Injection Mode	Fast Valve	Injector/ Switch	Z_{arc} [mΩ]
Marshall Gun [17]	Deuterium	Gas-puff	Yes	No	6
Deflagration Gun [18]	Hydrogen	Gas-fed	Yes	No	50
Solid-fed PPT [19]	Teflon	Ablation	No	Yes	14
Gas-fed PPT [20]	Argon	Gas-fed	Yes	Yes	10
Lorentz Accelerator [21]	Lithium	Vapor-fed	No	No	59
Self-field MPD [22]	Argon	Gas-fed	Yes	Yes	10
Solid-fed MPD [23]	Teflon	Ablation	No	Yes	9
Solid-fed MPD [16]	Graphite	Ablation	No	No	5
GEM	**Gallium**	**Ablation**	**No**	**Yes**	**6**

2.3 Survey of Past Performance Data

From the data collected in the MPD and PPT literature, it is observed that high efficiency is only achieved when the ionized propellant flow has enough charge carriers to conduct the discharge current. In the absence of sufficient current carriers, severe erosion of the electrodes and insulator occurs (the "onset" instability). A second requirement for high-efficiency operation is that the ion Larmor radius must be smaller than the radius of the thruster. A review of the literature data, a sampling of which is shown in Table 2.2, reveals that both requirements appear to have a significant effect on performance. The experimental data spans a wide range of propellant atomic weights, with data on hydrogen (AW=1), argon (AW=40), and xenon (AW=131) taken from Ref. [24] and data for nitrogen (AW=14) from

Ref. [22]. The last two columns in Table 2.2 were derived from the literature data to provide quantitative measures of high-efficiency EMT operation. The charge carrier parameter α is calculated from the particle flow rate $\mathrm{d}n/\mathrm{d}t$ (mass flow rate divided by the ion mass m_i) and the discharge current

$$\alpha = \left(\frac{Ze}{m_i I}\right)\left(\frac{dm}{dt}\right) \tag{2.1}$$

where Ze is the total ion charge, I is the discharge current, and m_i is the ion mass. The ratio defined by α represents the fraction of the discharge current that can be carried by the ionized propellant based on the number of charge carriers present. The calculations of α for each propellant reveal that singly-ionized hydrogen and nitrogen possess enough charge carries to conduct the discharge current ($\alpha > 1$) while argon and xenon do not ($\alpha < 1$). These data also show that α correlates with efficiency, yielding higher efficiencies for increasing values of α.

Table 2.2: Experimental MPD performance using various propellants, with calculated parameters α and R_L.

Propellant	AW	I [kA]	$\dot{m}$ [g/s]	I_{sp} [s]	Efficiency [%]	α	R_L [cm]
Hydrogen	1	20	0.5	16000	52	4.80	1.3
Nitrogen	14	18	4.0	4000	37	1.60	5.0
Argon	40	20	6.0	2800	20	0.72	8.8
Xenon	131	20	6.0	1400	10	0.22	14.4

The Larmor radius is defined as $R_L = mu_e/ZeB$ where B is the magnetic field strength and u_e is the particle axial exhaust velocity. Using the discharge parameters in Table 2.2, we estimate the Larmor radius as

$$R_L = 2\pi\left(\frac{m_i u_e}{Ze\mu_o I}\right)R \tag{2.2}$$

where μ_o is the magnetic permeability of free space, and R is taken as the average radius of the coaxial thruster

$$R \equiv (R_{anode} + R_{cathode})/2 \tag{2.3}$$

The Larmor radius R_L in Table 2.2 is calculated using $R = 3$ cm, which is consistent with Refs.[22] and [24]. For efficient thruster operation, the discharge current and resulting self-induced magnetic field must be high enough to allow ions that are driven radially by the **E** field to turn and drift axially out of the thruster without hitting an electrode. This will occur in thrusters where the value of $R_L < R$; the data in Table 2.2 shows that higher thrust efficiency is obtained in electromagnetic thrusters when this condition is satisfied.

2.3.1 Predictions for High-Performance Using Heavy Propellants

Using the above approach, we analyze the use of heavy propellants (gallium, xenon, bismuth) in more detail for the purpose of estimating EMT operating conditions that will result in high thrust efficiency. The estimates, summarized in Table 2.3 along with data from literature, are computed by fixing $\alpha = 1.6$ and $R_L = R$.

Table 2.3: EMT operating conditions using different propellants with measured(*) or predicted(**) efficiencies.

Propellant	At. Weight	I [kA]	$\dot{m}$ [g/s]	I_{sp} [s]	Efficiency [%]	α	R_L
Hydrogen*	1	20	0.50	16000	52	4.80	1.3
Lithium	7	9	0.45	4500	55	0.70	5.4
Nitrogen*	14	18	4.00	4000	37	1.60	5.0
Nitrogen	14	21	13.0	2800	50	1.60	3.0
Gallium**	70	75	140	2000	50	1.60	3.0
Gallium**	70	56	105	1500	43	1.60	3.0
Xenon	131	140	240	2000	50	1.60	3.0
Xenon	131	105	142	1500	43	1.60	3.0
Bismuth**	209	224	624	2000	50	1.60	3.0
Bismuth**	209	168	468	1500	43	1.60	3.0

For high-thrust near-Earth missions using electric propulsion, where shorter transfer times are important, the optimum specific impulse is roughly 1500-2000 seconds. We observe that to maintain the selected values of α and R_L, both thruster current and propellant flow rate must increase significantly with the propellant atomic weight. Bismuth and xenon (which work well in electrostatic thrusters because they increase thrust density) can be used in an efficient EMT, but the drawback is that the required discharge current exceeds 100 kA. At these current levels, internal capacitor and transmission line losses become significant, while the high power level drives the thruster towards short pulse lengths and unsteady flow. Propellant flow rates of up to 600 g/s, even for microsecond time scales, can only be achieved using an ablative (as opposed to a valved) feed system. In Table 2.3 for lighter propellants (N, Li, H) the I_{sp} is too high for near-Earth missions, and for heavier propellants (Xe, Bi) the current is too high. If we were to consider lower current levels, the I_{sp} would then be too low. However, operation with gallium appears possible since can we can achieve an I_{sp} of 1500-2000 s at reasonable currents (50 - 75 kA) and mass flow rates.

In Table 2.4 we consider the effect on the discharge current and mass flow rate of having a plasma comprised of either singly (Ga II), doubly (Ga III), or triply (Ga IV) ionized gallium (we later show both Ga II and Ga III are observed spectroscopically). The operating conditions shown are necessary for an efficiency of 50%. To hold α constant in a doubly ionized gallium plasma, the current would be reduced by a factor of two and the propellant flow lowered by a factor of four relative to a plasma comprised only of singly ionized gallium. This also means for a given pulse energy, the pulse length is quadrupled for a doubly ionized propellant. However, the presence of higher ionization states reduces the frozen flow efficiency. The effect of ionization on the frozen flow efficiency is shown in Table 2.5. Note that the frozen flow efficiency of Ga III at 2000 seconds is the same as lithium at 6000 seconds, indicating potentially high efficiency for gallium.

Summarizing, we contend that efficient operation of electromagnetic thrusters occurs when there are enough charge carriers present to conduct the current and when the Larmor radius

Table 2.4: Conditions for efficient EMT operation with singly,doubly, and triply ionized gallium propellant.

Ga Ion State	I [kA]	$\dot{m}$ [g/s]	I_{sp} [s]	Efficiency [%]	α	R_L [cm]
Ga II	75	140	2000	50	1.60	3.0
Ga II	56	105	1500	50	1.60	3.0
Ga III	37	35	2000	50	1.60	3.0
Ga III	28	26	1500	50	1.60	3.0
Ga IV	25	18	2000	50	1.60	3.0
Ga IV	19	13	1500	50	1.60	3.0

Table 2.5: Estimated frozen flow efficiency in EMTs operating on gallium and lithium.

Propellant	Ion AW	I_{sp} [s]	Kinetic Energy [eV]	Ion. Potential [eV]	Frozen Flow Eff. [%]
Li	7	6000	132	5.4	96
Ga II	70	2000	146	6.0	96
Ga II	70	1500	82	6.0	83
Ga III	70	2000	146	26.4	85
Ga III	70	1500	82	26.4	76
Ga IV	70	2000	146	57.1	61
Ga IV	70	1500	82	57.1	30

is smaller than thruster channel. For heavier propellants, the implications are:

- The discharge current must scale with the ion mass and exhaust velocity to keep the Larmor radius small. This was not done in previous experiments [24] with xenon, which should have been operated at higher current levels than argon or nitrogen to achieve high efficiency.

- The propellant mass flow rate must scale with the ion mass and discharge current to maintain a high number of charge carriers, i.e. $\alpha > 1$. Thrusters using heavier propellants such as xenon and gallium need to be operated at much higher mass flow rates than argon or hydrogen to provide enough current-carrying particles.

The requirement for relatively large discharge currents fueled the design of the pulse forming network used to produce the current pulse in the GEM thruster (Appendix B). From Table

2.4, it can be seen that currents as high as 70 kA may be necessary to keep the Larmor radius smaller than the radius of the outer electrode (for a singly ionized plasma).

2.4 Review of Electromagnetic Scaling Relations

In this section, the basic scaling relations for electromagnetic thrusters are briefly reviewed. The thrust follows a quadratic dependence on the discharge current [1]

$$T = \frac{1}{2} L' I^2, \text{where } L' = \left[\frac{\mu_o}{2\pi} \left(\ln \frac{r_o}{r_i} + c \right) \right] \tag{2.4}$$

where L' is the inductance gradient and is a function of the thruster geometry. The exhaust velocity is found by dividing the thrust by the mass flow rate

$$u_e = \frac{T}{\dot{m}} = \frac{\int T}{m} \tag{2.5}$$

where m is the mass ablated per pulse (mass bit). For ablative-type thrusters, it is convenient to write the mass flow rate as following a power law dependence with the discharge current

$$\dot{m} \propto I^{\beta} \tag{2.6}$$

where β is an empirical ablation exponent introduced in order to characterize the dependence of the ablative mass flow rate on the discharge current. Note that for gas-fed thrusters, the mass flow rate is independent of the discharge current and $\beta = 0$. Substituting Eqns. (2.4) and (2.6) into (2.5), we find

$$u_e \propto I^{2-\beta} \tag{2.7}$$

The power across the discharge is given by

$$P = IV_{arc} \propto \frac{1}{2}\dot{m}u_e^2 \tag{2.8}$$

From which we find

$$V_{arc} \propto I^{3-\beta} \tag{2.9}$$

The voltage-current characteristics have been examined in a gas-fed MPD over a wide range of current levels by Boyle [25] as shown in Fig. 2.1. It can be seen that the V-I characteristic splits into three distinct regions (slopes). The first region corresponds to an electrothermal regime of operation, where the voltage scales linearly with the current. The second region corresponds to the electromagnetic regime described by Eqn. 2.9 (with $\beta = 0$). At the highest current levels, the voltage reverts back to a linear dependence. This was due to the entrainment of backplate insulator materials being ablated during the pulse.

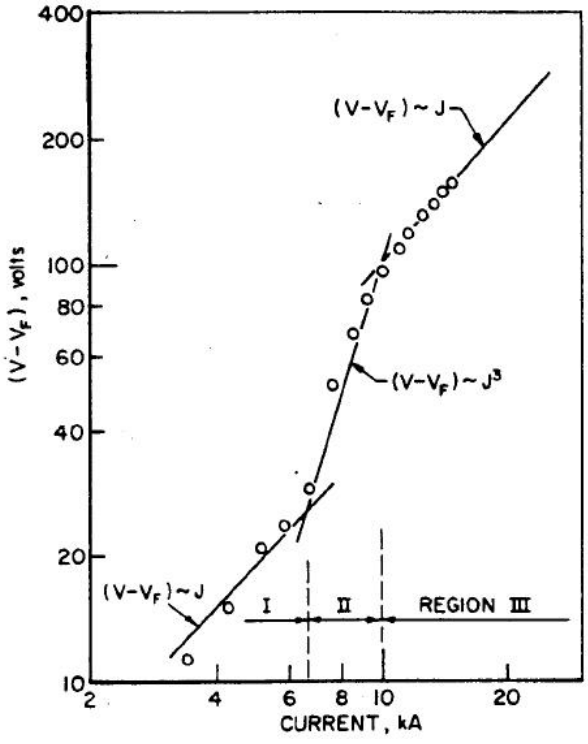

Figure 2.1: V-I comparison for a self-field, gas-fed MPD.

2.5 Ablative Thruster Comparison

The performance of three previously developed ablative EMT's are now examined: the Teflon PPT [19], Teflon MPD [23], and graphite MPD [16]. The propellant rests between the metal electrodes for both Teflon thrusters, and is ablated when an arc is struck between the electrodes. The graphite MPD is similar to the GEM thruster in that the ablated central electrode serves as the propellant source. In order to compare thrusters with different current levels and pulse lengths, the current action integral ψ is introduced

$$\psi \equiv \int_0^{\tau_p} I^2 dt \tag{2.10}$$

The current of the unsteady PPT pulse is taken to be $(\psi/\tau_{1/2})^{1/2}$ where $\tau_{1/2}$ is taken to be the amplitude of the first positive half cycle of the current pulse (9 μs). The voltage-current characteristics are shown in Fig. 2.2. Both MPD thrusters have linear slopes, which suggests that the ablated mass varies quadratically with the discharge current ($\beta = 2$) and that the exhaust velocity is invariant with the discharge current. The Teflon PPT has a slightly higher slope, suggesting increased performance as the current is increased.

A plot of the ablated mass per pulse vs. ψ is shown in Fig. 2.3. The mass bit dependence of the three thrusters is in accord with equations (2.6) - (2.9) and Fig. 2.2. The mass ablated per pulse indeed scales quadratically with the discharge current for both MPD thrusters, while $\beta = 1.4$ for the Teflon PPT. The velocities and thruster efficiencies of the three thrusters are tabulated in Table 2.5. Thrust measurements were obtained with both the Teflon PPT and graphite MPD, and the velocity was calculated by dividing the impulse bit by the mass ablated per pulse. The velocity of the Teflon MPD was measured using a time-of-flight technique. The velocity varies by less than 10% and the efficiency is nearly constant for the thrusters that exhibit $\beta = 2$ behavior, while the Teflon PPT has an increase in both the exhaust velocity and efficiency as the discharge current is increased.

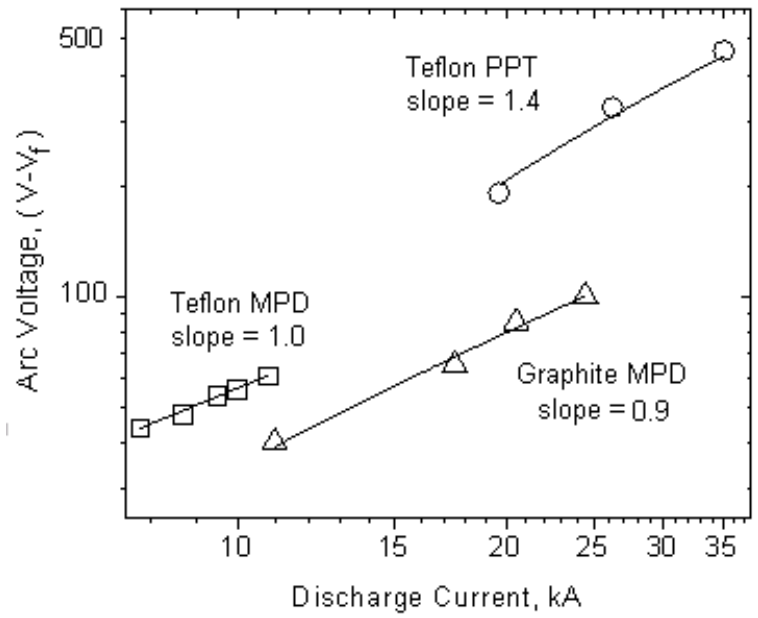

Figure 2.2: Voltage-current characteristic for Teflon PPT, Teflon MPD, and graphite MPD thrusters.

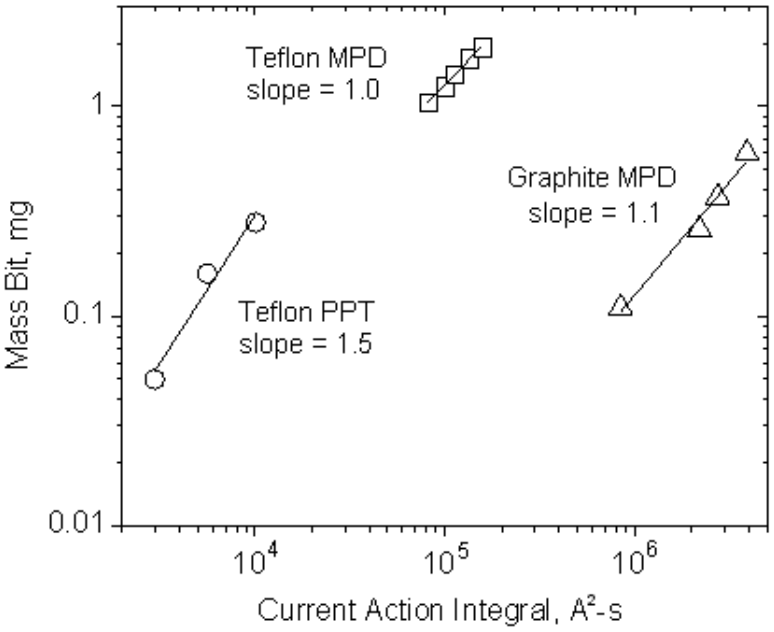

Figure 2.3: Comparison of mass bit vs. current action integral for Teflon PPT, Teflon MPD, and graphite MPD thrusters.

Of interest is the Alfvén critical velocity [26], which has been correlated with MPD performance [27, 28, 29]. Alfvén hypothesized that when the relative velocity of neutral particles with respect to the plasma reaches a critical value, an abrupt increase in the degree of ion-

Table 2.6: Ablative thruster exhaust velocity and thruster efficiency (η) comparison.

Teflon PPT			Teflon MPD			Graphite MPD		
I [kA]	u_e [km/s]	η [%]	I [kA]	u_e [km/s]	η [%]	I [kA]	u_e [km/s]	η [%]
18.3	8.9	8.0	7.7	15.5	12	11.0	31.1	7.0
24.7	13.6	14	8.7	16.3	16	17.5	31.5	7.0
33.5	15.0	15	9.5	16.0	15	20.5	30.5	7.0
			10	15.1	14	24.5	27.8	7.0
			10.8	16.6	16			

ization occurs. This critical velocity is often viewed at as an upper limit on the exhaust velocity for a partially ionized gas and is given by

$$u_c = \left(\frac{2\epsilon_i}{m_i}\right)^{1/2} \tag{2.11}$$

The MPD thrusters both exceed this critical velocity, while the Teflon PPT approaches and exceeds u_c ($u_c \approx 13.5$ km/s) as the current is increased. This suggests a high degree of ionization as the input power is increased, because the presence of neutrals would constrain the velocity to the u_c value.

The results of the above analysis show that for two out of the three ablative thrusters selected from the literature, the mass flow rate scales quadratically with the discharge current. This also appears to be the case for the gas-fed MPD when significant insulator erosion occurs. This is significant because it suggests moderate gains in performance as the power level (discharge current) is increased. In later chapters this analysis will be performed on the GEM thruster and it will be shown that $\dot{m} \propto I^2(\beta = 2)$.

Chapter 3

Experimental Apparatus

3.1 Introduction

A description of the facilities, thruster, and experimental layout is presented. A qualitative ion trajectory model is presented conjunction with the electrode polarity. The design criteria for the GEM thruster are discussed in detail.

3.2 Vacuum Facilities

Tests are conducted at the University of Illinois Electric Propulsion Laboratory. The thruster is mounted into a 5-way vacuum cross, which is attached to the main vacuum chamber. A baffle is inserted into the 5-way cross to condense ejected gallium particles before they reach the main chamber. Vacuum is maintained by a TPH1500 turbomolecular pump, which is backed by two Roots blowers and two Kinney mechanical displacement pumps. The base pressure of the facility during testing is 5×10^{-5} Torr.

3.3 Pulse Forming Network

A ten-section, 5-line pulse forming network (PFN) was designed and fabricated to power the thruster. Each section consists of ten 88 μF capacitors capable of a charging voltage of 1.2 kV, each in series with a 85 nH inductor, for a total of 50 capacitors yielding a maximum bank energy of 3.2 kJ. A copper sheet with punched holes is laid over the capacitors to provide a common ground (ground plane). Brass standoffs with a height of 3.8 cm provide spacing

between the stage inductors and the ground plane. The section inductors are composed of two 9 cm long, 0.32 cm (1/8") diameter copper rods, yielding the section inductance of 85 nH. The five PFN lines are connected in parallel using a bus fabricated from a 2.5 cm wide copper strip. To minimize stray inductance in the charging circuit, the PFN is mounted close to the vacuum chamber, as shown in Fig 3.1. A 7.0 cm wide strip of copper sheet forms the transmission line. The capacitors are charged using a Hipotronics DC power supply. A 20 J spark igniter is used to initiate plasma breakdown and discharge the capacitors; that is, the capacitor bank does not contain a switch. This simplifies the testing apparatus and eliminates the circuit resistance associated with a switch (which could have potentially led to an impedance mismatch). A detailed description of the PFN design, including the PSPICE model is presented in Appendix B.

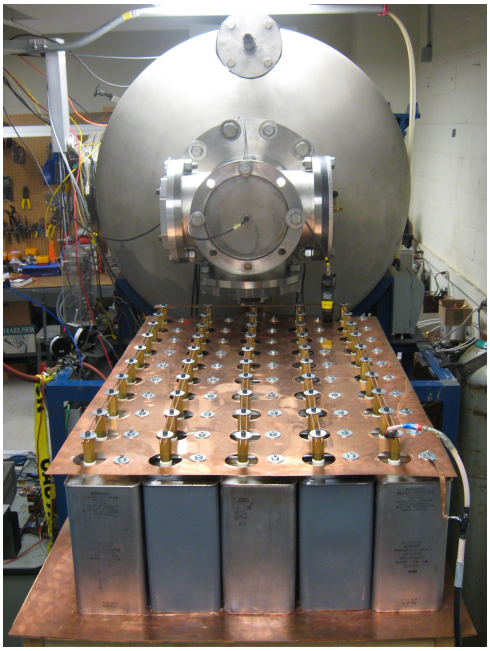

Figure 3.1: 3.2 kJ Pulse Forming Network.

An experimental and simulated discharge current pulse is shown in Fig. 3.2. As detailed by Clark [30], quasi-steady operation is characterized by a constant arc voltage, a stabilized, fixed current distribution within the discharge, and a steady plasma efflux at velocities on

the order of 10 km/s. The arc voltage, spatially and time-resolved magnetic field probe measurements, and electrostatic probe measurements detailed in Chapter 5 are consistent with aforementioned criteria.

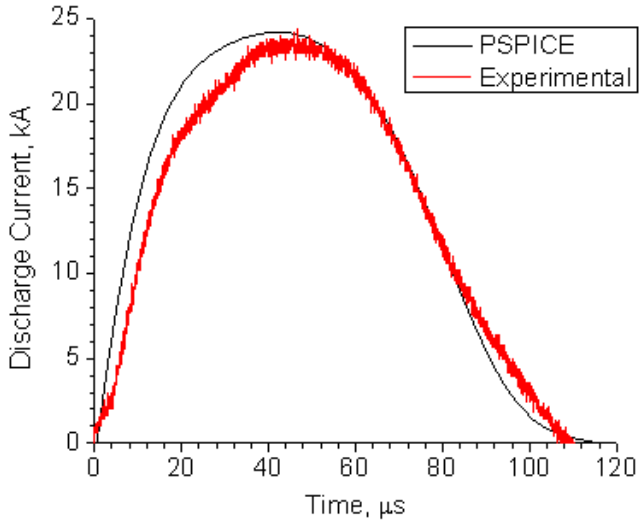

Figure 3.2: Experimental and simulated current pulse taken at I = 22.6 kA.

3.4 Discharge Initiation

Arc initiation in a vacuum environment is difficult due to the extremely low vapor pressure of the gallium propellant. Initial 20 J experiments (Appendix A) used a thin layer of graphite to bridge the cathode and anode, creating a conductive path for the discharge current. While successful at initiating breakdown, a fraction of the discharge energy was lost in excited and ionized carbon atomic states. As a remedy, a plasma spark igniter plug is used to initiate the discharge. Such an approach is typically used in PPT experiments and other thrusters using a low vapor pressure propellant. The igniter plug used is a semiconductor-type aircraft turbine combustor spark plug [31] mounted 5-10 cm from the face of the thruster. The igniter is powered by a 20 J power supply, shown in Fig. 3.3.

By placing the igniter along the center-line of the the thruster, operation at 50 μTorr is

possible and a symmetric discharge is achieved. It was found that after several hundred shots, the spark plug became clogged with gallium and would no longer fire. This was remedied by firing the igniter plug several hundred times in between tests to keep it clean. A photograph of the thruster and igniter mounted inside the 5-way cross is shown in Fig 3.4.

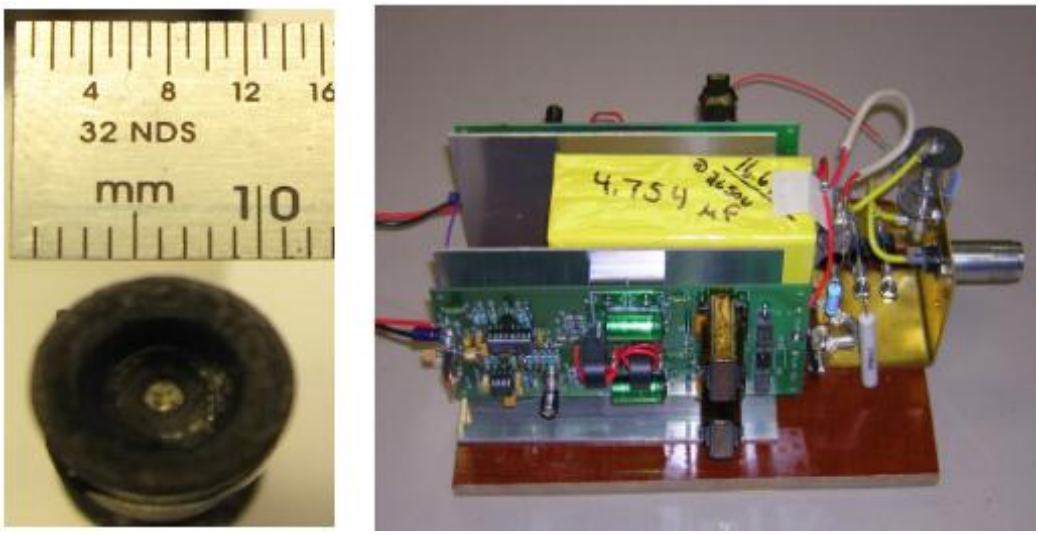

Figure 3.3: Photograph of igniter (left) and 20 J power supply (right).

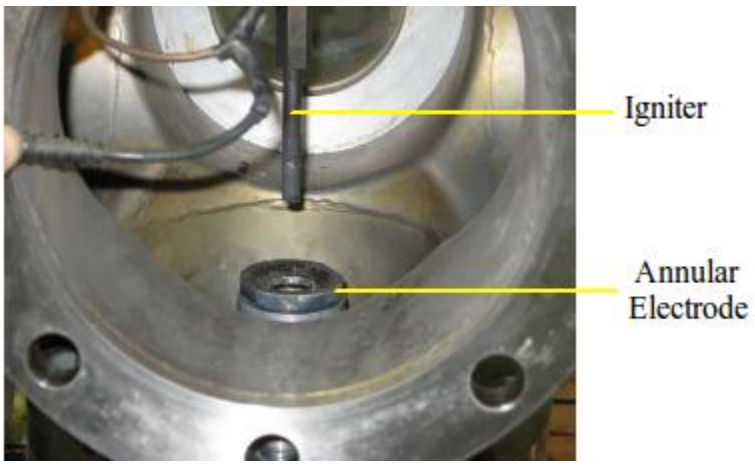

Figure 3.4: GEM thruster and spark igniter mounted inside 5-way cross in vacuum chamber.

3.5 Electrode Polarity

In an attempt to gain additional insight into the acceleration process, a qualitative description of the plasma dynamics in the GEM thruster is presented. Two cases are presented; that for which the central electrode is the cathode (normal polarity) and the anode (reversed polarity). Since ions carry the momentum, it is important to understand the ion acceleration mechanism. The ions gain energy from the electric field. When operating with a central cathode, ions that form near the outer anode are accelerated radially inward and deflected downstream by the e$\mathbf{u}_i \times \mathbf{B}$ force as shown in Fig. 3.5a. For a reversed polarity, ions are generated near the central electrode and similarly turned downstream. The difference between the normal and reversed polarity is that in the former, the ion enters the region of strong B-field as it is accelerated radially inward by the radial electric field. For the latter case, the ion is created in the region of strong B-field, possessing a smaller Larmor radius and turning downstream more easily because its radial velocity is not nearly as high as in the central cathode case.

The other important factor in determining the ion trajectory is the axial electric field, also shown in Fig. 3.5. For a thruster with a long outer electrode and a short central electrode, E_z along the axis opposes the ion motion in the central cathode polarity case, but is in the same direction as the exhaust velocity vector when polarity is reversed. Finally, in either case, the boundary condition that $\mathbf{E}$ is perpendicular to the conducting outer electrode reduces E_z to zero in the outer regions.

Due to the above considerations, experiments were initially conducted using a central anode. However, the ejection of gallium macroparticles while using a central anode led operation using a central cathode. Results of the experiments using both polarities are discussed in Chapter 5.

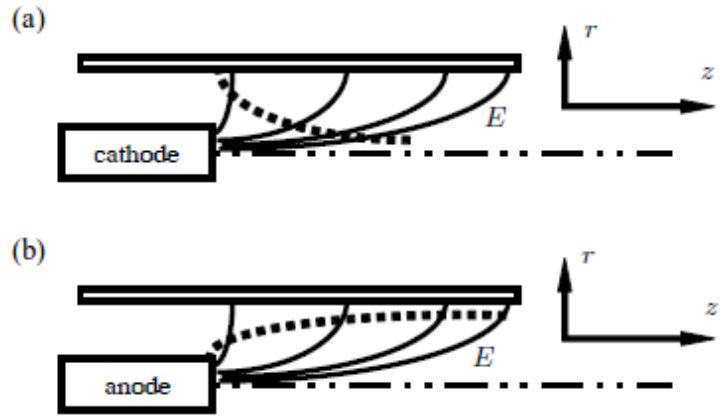

Figure 3.5: Schematic showing ion trajectories (dotted lines) for when the central electrode is (a) the cathode (normal polarity) and (b) the anode (reversed polarity).

3.6 Thruster Design

3.6.1 Gallium Injector Design

As discussed in Chapter 1, the original GEM design utilized a two-stage thruster geometry. The design of the 20 Joule gallium injector is now described. Minor modifications were made to the central electrode of the gallium injector for the high-powered tests and are discussed in the next section.

A coaxial geometry is employed, with the choice of materials playing a strong role in the design of the thruster. A literature review [32] reveals that gallium alloys with copper, aluminum and various other common metals. 316L stainless steel is therefore used for the annular electrode and for the thruster parts that have repeated contact with the liquid gallium. At the heart of the design is a 0.5" porous tungsten disk press fit inside a threaded 0.75" stainless steel fitting (supplied by NASA MSFC). The porous disk served as the (underlying) central electrode. A connecting hollow stainless steel tube was then machined to provide a channel for the injected liquid gallium, which is supplied from outside the chamber. A photograph of the porous tungsten electrode and connecting stainless steel fitting is shown in Fig 3.6.

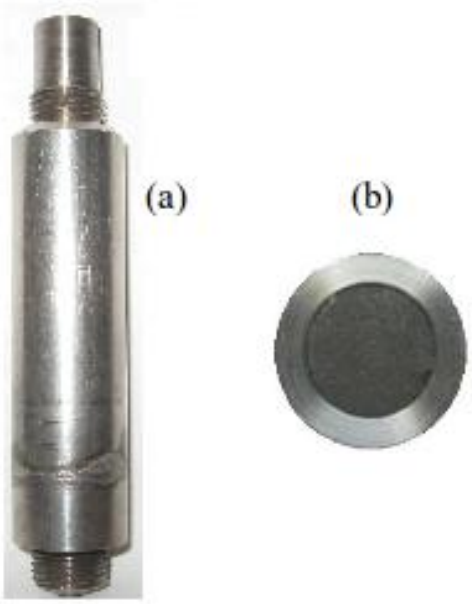

Figure 3.6: Photograph of (a) stainless steel connecting channel and (b) top view of porous inner electrode.

Boron nitride is used to electrically isolate the inner and outer electrodes due to its wear resistance at high temperatures. The annular electrode is composed of 316L stainless steel with a 30° chamfer. The thruster is electrically isolated from the chamber by mounting it in a 0.75" thick Lexan window as shown in Fig 3.8. A schematic and photograph of the coaxial injector is shown in figures 3.7 and 3.9.

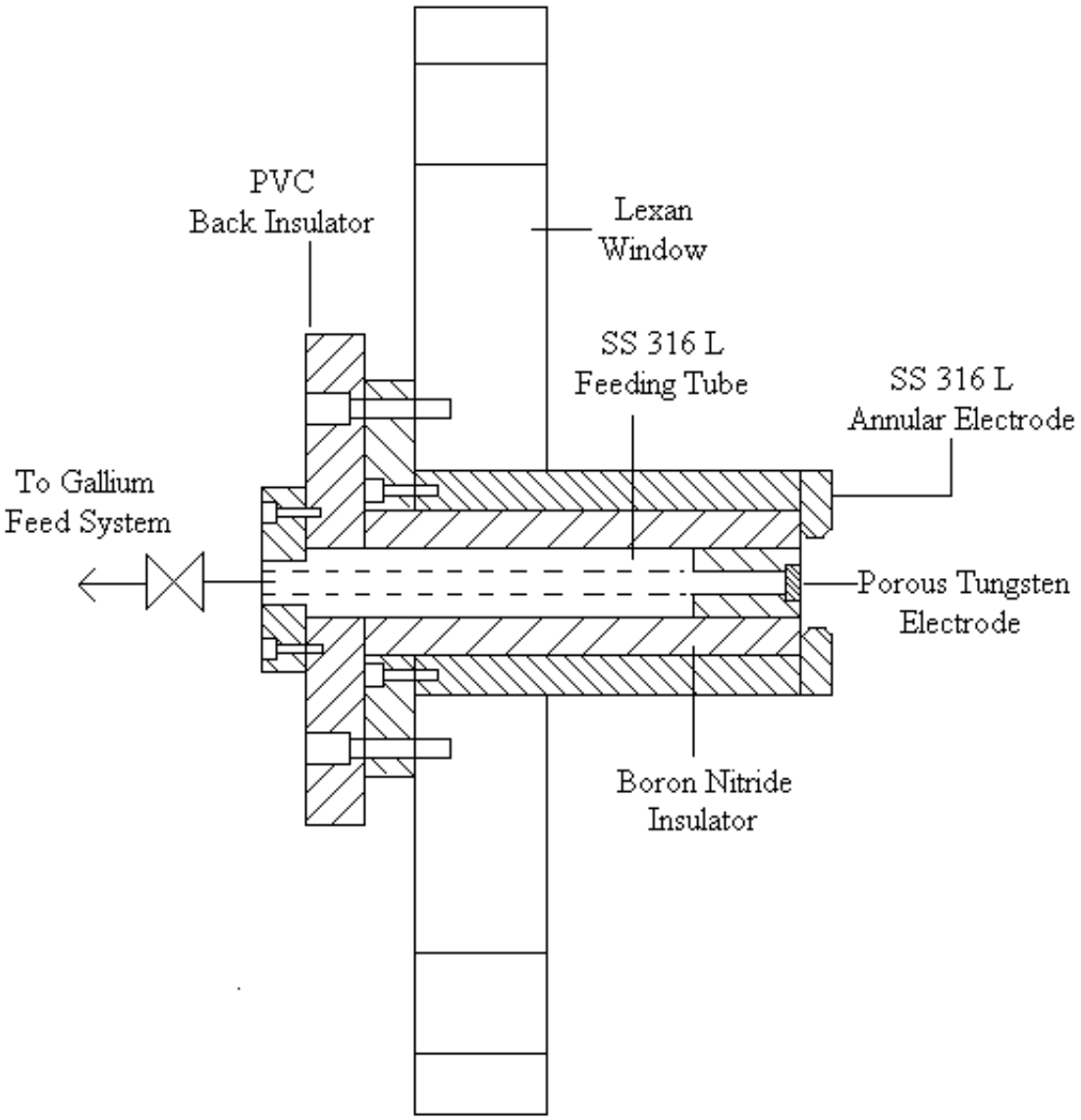

Figure 3.7: Schematic of gallium injector stage.

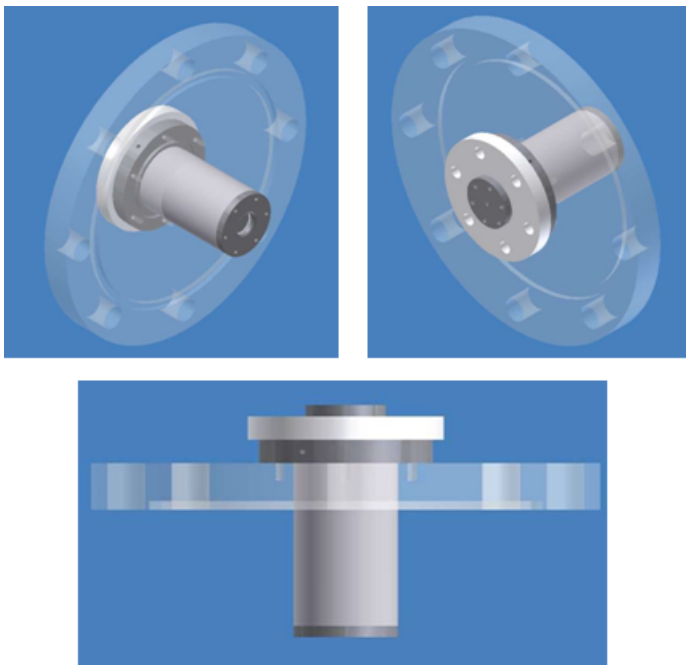

Figure 3.8: Three CAD views of gallium injector mounted in Lexan chamber window.

Figure 3.9: Photograph of coaxial gallium injector with a porous tungsten center electrode.

3.6.2 Final Thruster Design

After the completion of the 20 J proof-of-concept experiments (described in Appendix A), several changes were made to the multi-stage design of the GEM thruster described in Chapter 1. The multi-stage thruster design was eliminated, and a single-stage coaxial geometry was used. Additionally, a spark igniter was used to initiate the arc. These changes were made to simplify the testing apparatus and the performance measurements.

Of primary interest is the mass ablated per pulse, which is extremely difficult to measure using a continuously-fed propellant system. By using a solid electrode, the mass ablated per pulse is easily measured by weighing the gallium before and after a prescribed number of shots. Additionally, physical inspection of the gallium electrode (e.g. postmortem craters) is only possible using a solid electrode. Additionally, the charging time of the capacitor bank used in the present experiment is on the order of 30 seconds. The small amount of gallium ablated per pulse (< 0.5 mg) combined with relatively low pulse rate make matching the propellant feed rate to the discharge current pulses impractical for the present experiment. Therefore, a solid gallium electrode replaced the continuously fed gallium electrode. The enthalpy of fusion is much less than the enthalpy of vaporization (5.6 kJ/mol vs. 243 kJ/mol) so operating with a solid electrode is not expected to have a significant effect on the experimental results.

The final consideration left in the design of the thruster is the actual size of the gallium electrode. As shown in the previous chapter, the performance of a coaxial electromagnetic thruster scales with inductance gradient L'

$$L' = \frac{\mu_o}{2\pi}\left(\ln\frac{r_o}{r_i} + c\right) \tag{3.1}$$

It is therefore beneficial to maximize the electrode radius ratio. However, it has been found that when the electrode radius ratio exceeds 5, the MPD thruster becomes prone to a spoking instability [33, 34]. This sets an upper limit for electrode radii during the course of

experiments.

The ion flux to the gallium electrode and the resulting surface temperature increase must also be considered. It is desirable to vaporize the gallium on a time scale comparable to the rise time of the current pulse. The surface temperature as a function of time can be found by considering the heat equation [35]

$$c_p \rho \frac{\partial T}{\partial t} - \nabla(\lambda \nabla T) = (J \cdot E) \tag{3.2}$$

where c_p is the specific heat capacity, ρ is the density, and λ is the thermal conductivity of the gallium cathode. For current densities below 10^{10} A/m^2, Joule heating $(J \cdot E)$ can be neglected and Eqn. 3.2 and be integrated to yield an implicit expression for the time needed to vaporize the semi-infinite cathode surface

$$T_{vap} = T_o + \frac{1}{\lambda}\sqrt{\frac{\alpha}{\pi}} \int_{t=0}^{t_{vap}} \frac{P_{in}}{(t-s)^{1/2}}\, \mathrm{d}s \tag{3.3}$$

where P_{in} is the incoming power flux of ions, α is the thermal diffusivity $(\lambda/\rho c_p)$, and s is a dummy variable for time. The power density flux is expressed as [35]

$$P_{in} = j_{ion}(Ze\phi_c + 2kT_i + Ze(\phi_i - \phi_w) + h_{vap}) \tag{3.4}$$

where ϕ_c, ϕ_i, ϕ_w are the sheath, ionization, and work function potentials, and h_{vap} is the enthalpy of vaporization. The ion current density j_{ion} is estimated from

$$j_{ion} = B_f Ze\Gamma \tag{3.5}$$

where B_f is a back-flow coefficient on the order or 0.5, and Γ is the atomic mass flux given by [36]

$$\Gamma = \frac{p_v}{2\pi m_i k T_s} \tag{3.6}$$

The possible presence of anode/cathode spots, the movement of such spots, and the convection of heat between the spots complicate this problem. For the purpose of this calculation, it is assumed that the current density is constant over the entire electrode surface (Fig. 3.10). The surface vaporization time can be calculated implicitly using Eqn. 3.3. The vaporization time as a function of the discharge current is shown in Fig. 3.11. The input power is modeled by using a linear region (corresponding to the current pulse rise time of 12 μs) followed by a constant power input, which corresponds to the quasi-steady portion of the pulse. For a 20 kA current pulse, the vaporization time is on the order of 2 μs.

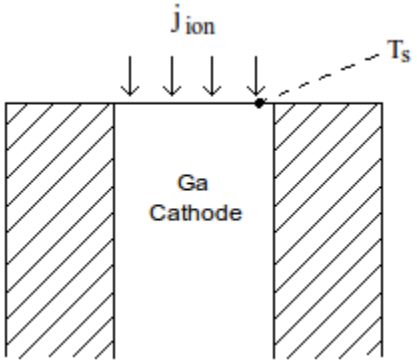

Figure 3.10: Uniform current density model used in heat conduction model.

From the above analysis (Eqn. 3.3), a central gallium electrode with a diameter of 5 mm was chosen for the initial experiments. It was found during the low-energy experiments (Appendix A) that the arc preferentially struck the stainless steel surrounding the porous tungsten electrode (Fig. 3.9). It was therefore beneficial to completely eliminate all exposed metal surfaces except the gallium and annular stainless steel. The gallium was thus contained within a hollow 0.75" boron nitride tube as shown in Fig. 3.12.

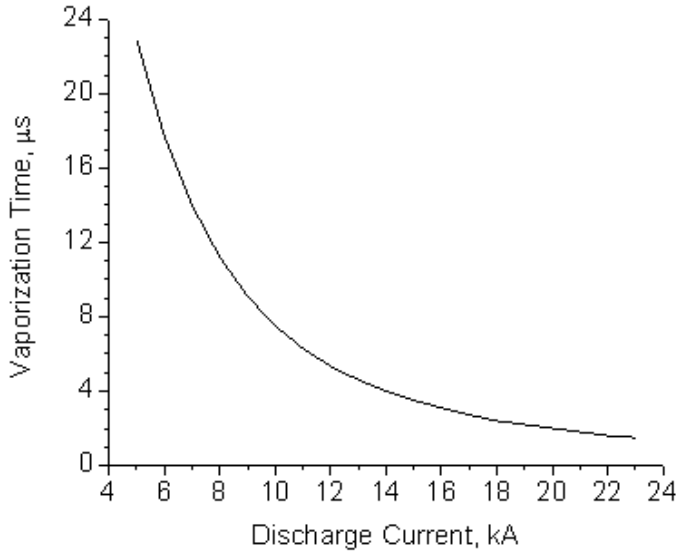

Figure 3.11: Time needed to vaporize gallium electrode as a function of input current.

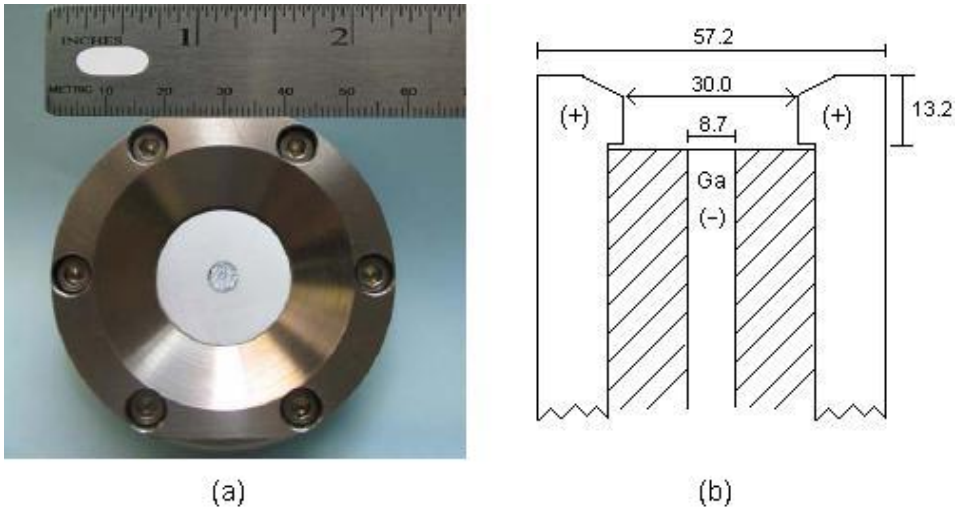

Figure 3.12: Final thruster design with solid gallium electrode (dimensions in cm).

Chapter 4

Diagnostics

4.1 Introduction

In this chapter the diagnostics used to characterize the gallium plasma are described. The discharge current and arc voltage are measured and used to calculate an arc impedance, which gives important information about the electromagnetic acceleration efficiency. The mass ablated per pulse is a fundamental characteristic of an ablative thruster, and is measured by post-test weighing of the electrodes. Emission spectroscopy is used to determine the ion species present within the discharge plume and are also used to calculate an electron temperature. Several electrostatic probe techniques are employed to obtain spatially resolved values of the electron temperature, density and exhaust velocity. Magnetic field probe data is used to infer information about the current density within the inter-electrode region.

4.2 Current Monitoring

A Pearson (model 4418) current-monitoring transformer is used to measure the discharge current. The discharge current is measured during all experiments and is used as the trigger for the oscilloscope measurements, and for synchronization in the spectroscopy measurements.

4.3 Voltage Measurements

The time-varying voltage across the cathode and anode (arc voltage) is measured using a P6015A high-voltage probe. During the course of experiments, the central gallium electrode

is grounded, and the the high voltage lead was attached to the outer anode. The probe has a bandwidth of 75 MHz, an attenuation ratio of 1000×, and a maximum peak-to-peak voltage of 40 kA. The probe was calibrated using the standard procedures described in the instruction manual.

4.4 Emission Spectroscopy

Spectroscopic data were measured from the discharge to determine which species were present. These spectra were obtained using a 25 mm focal length spectrometer with 5 micron inlet slit, yielding 0.7 nm resolution over the range of 220 nm to 520 nm. Emission was collected using a 12 mm diameter f/2 quartz plano convex lens which was focused onto the end of a 400 micron diameter silica fiber. The spectrum was time-integrated over several discharge pulses and spatially integrated over a broad region. The output of the spectrometer was wavelength-calibrated using a mercury lamp and corrected for relative spectral efficiency using a deuterium lamp. A schematic of the spectroscopic apparatus is shown in Fig.4.4. The emission spectrum is integrated over a path length of 20 cm, and the measured signal consists of the cold, warm, and hot regions of the discharge.

4.5 Ablated Mass Measurements

The mass ablated per pulse is measured by weighing both the gallium and annular stainless steel electrode (Fig. 3.12) before and after a prescribed number of shots using a Mettler AG245 measurement scale. The scale has a resolution of 0.1 mg, therefore a minimum of 10 mg is ablated in between measurements, leaving the error due to experimentation at less than 1%. The central gallium electrode and surrounding boron nitride insulator are exposed to the arc, therefore both are weighed simultaneously. Visual inspection of the insulator combined with a lack of boron and nitrogen emission lines suggests that very little boron nitride is ablated during each pulse.

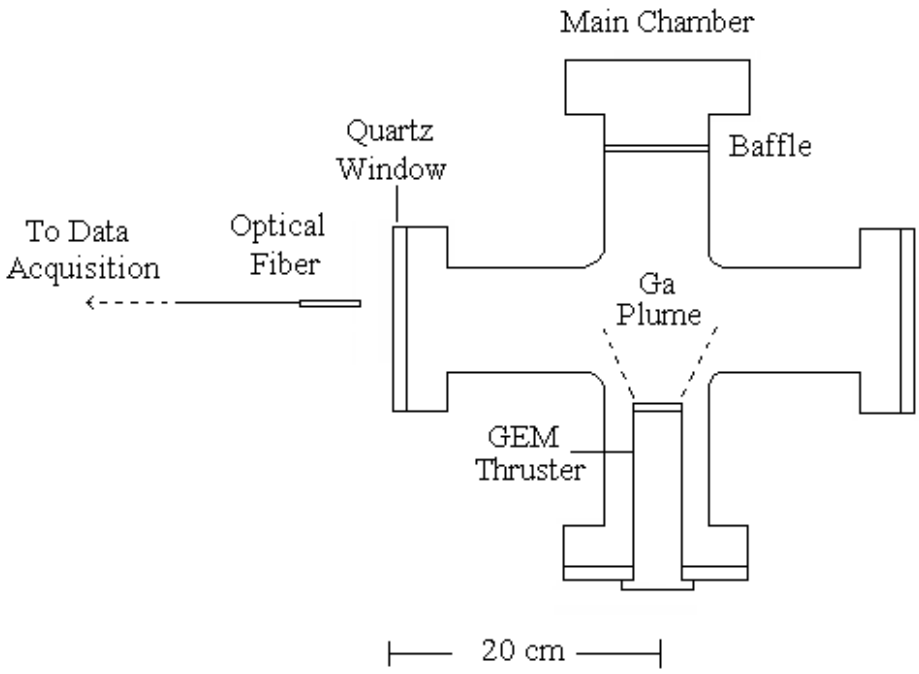

Figure 4.1: Schematic of spectroscopy apparatus.

4.6 Triple Langmuir Probe Measurements

The triple Langmuir probe has been used extensively in MPD and PPT plumes to determine the electron density and temperature [37, 38, 39]. Triple probe measurements have compared favorably to those of single probes, double probes, and optical measurements (Ref. [40] and references therein). The triple probe used in this study consists of three 0.191 mm tungsten wires with an exposed length of 6 mm and a probe separation distance of $s = 1$ mm. Two floating voltages are supplied by using lead-acid rechargeable batteries. A 30 A power supply was initially used to supply the voltage, however the supply was unable to supply a constant voltage during the beginning of the pulse. The probe currents are measured using Pearson current 1:1 current transformers.

The theory of triple probes was originally developed by Chen and Sekiguchi [41] and a summary is now briefly presented. The triple probe consists of three electrodes, two of which are biased negatively with respect to probe 1 (Fig. 4.2).

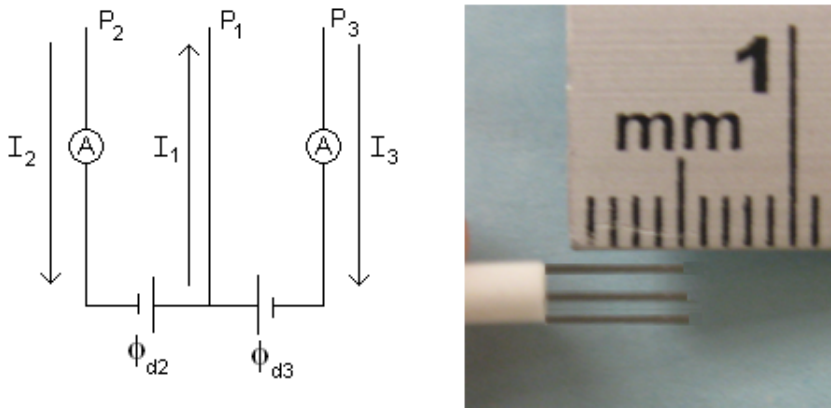

Figure 4.2: Schematic and photograph of triple probe.

The current flowing into each probe is the sum of the random electron current J_e and the ion current j_i.

$$\begin{aligned} -I_1 &= -A_p j_e \exp(\chi_1) + A_p j_i(\chi_1) \\ I_2 &= -A_p j_e \exp(\chi_2) + A_p j_i(\chi_1) \\ I_3 &= -A_p j_e \exp(\chi_3) + A_p j_i(\chi_1) \end{aligned} \tag{4.1}$$

(4.2)

where

$$\chi \equiv \frac{e(\phi - \phi_p)}{kT_e} \tag{4.3}$$

$$j_e = \frac{1}{4} n_e e \left(\frac{8kT_e}{\pi m_e} \right)^{1/2} \tag{4.4}$$

and ϕ_p is the plasma space potential. Assuming the ion saturation currents collected by each probe are equal, the Bohm sheath criteria can be used to derive an expression for the ion current, which is independent of the applied voltage

$$j_i = \exp\left(-\frac{1}{2}\right) e n_e \left(\frac{kT_e}{m_i}\right)^{1/2} \tag{4.5}$$

Solving (4.1) - (4.5) yields time-resolved values of n_e, T_e, and ϕ_p. These equations make use of the following assumptions

1) The electron energy distribution is Maxwellian.

2) The ion sheath surrounding the probe is small compared to the ion mean free path (collisionless sheath).

3) The ion sheath is much smaller than the radius of the probe (thin sheath) and the separation distance of the probes.

To check the validity of these assumptions, several length scales must be calculated. The first of which is the Debye length, the maximum distance over which an ionized gas may be non-neutral. The thickness of the ion sheath is typically taken to be on the order of the electron Debye length

$$\lambda_D = \left(\frac{\epsilon kTe}{e^2 n_e}\right)^{1/2} \tag{4.6}$$

The mean free path is defined as $\lambda_{mfp} = 1/(n\sigma)$ where σ is the relevant Coulomb cross section. From prior MPD research data, the electron density is expected to be in the range of $10^{18} - 10^{22}$ m^{-3}, electron temperatures in the range of 1-5 eV, and ion temperatures on the order of the electron temperature. The table below summarizes the relevant length scale ratios. The ratio s/λ_D is the ratio of the probe separation to the Debye length and the ion Knudsen number (Kn) is the ratio of the ion mean free path to the probe radius. From these preliminary calculations, it appears the thruster will operate in thin sheath, collisionless regime under most operating conditions. Also tabulated is the electron-electron mean free path λ_{ee}. Electron-electron collisions force the electron distribution to a Maxwellian if the density is high enough such that collisions between electrons produce an equilibrium.

Table 4.1: Triple probe length scale calculations for $T_e = T_i = 1$ eV.

n_e, m^{-3}	r_p/λ_D	s/λ_D	λ_{ii}/λ_D	λ_{ii}/r_p	λ_{ee}, m
10^{18}	26	161	2.1e3	83	8.9e-03
10^{19}	82	510	7.6e2	9.3	1.0e-03
10^{20}	257	1613	2.7e3	1.1	1.2e-04
10^{21}	812	5101	1.0e2	0.1	1.3e-05
10^{22}	2568	16131	3.8e1	0.01	1.6e-06

Table 4.2: Triple probe length scale calculations for $T_e = T_i = 5$ eV.

n_e, m^{-3}	r_p/λ_D	s/λ_D	λ_{ii}/λ_D	λ_{ii}/r_p	λ_{ee}, m
10^{18}	11	72	1.9e4	1675	1.8e-01
10^{19}	36	228	6.7e3	184	1.9e-02
10^{20}	115	721	2.3e3	20	2.2e-03
10^{21}	363	2281	8.3e2	2.3	2.5e-04
10^{22}	1148	7214	3.0e2	0.3	2.5e-05

4.6.1 Triple Probe Corrections

Numerical corrections have been made to improve on the original triple probe theory. The expressions for the electron temperature and density are derived assuming that the ion current collected by each probe is equal. This is not strictly true; the ion saturation current increases as the magnitude of the negative probe potential increases. The error associated with the ion current increase depends on the thin sheath approximation, $r_p >> \lambda_D$. Chen [42] showed that when the probe radius exceeds the Debye length by several orders of magnitude, the error associated with assuming a constant ion saturation current is small. For $5 < r_p/\lambda_D < 100$ Peterson and Talbot [43] provided a numerical fit using the exact calculations of Laframboise [44]. The corrected equations for the probe currents become

$$-I_1 = -Sj_e \exp(\chi_1) + Sj_i(\beta + \chi_1)^\alpha \tag{4.7}$$

$$I_2 = -Sj_e \exp(\chi_2) + Sj_i(\beta + \chi_2)^\alpha \tag{4.8}$$

$$I_3 = -Sj_e \exp(\chi_3) + Sj_i(\beta + \chi_3)^\alpha \tag{4.9}$$

where the curve fit parameters α and β are given by

$$\alpha = \frac{2.9}{\ln(r_p/\lambda) + 2.3} + 0.07\left(\frac{T_i}{ZT_e}\right)^{0.75} - 0.34 \tag{4.10}$$

$$\beta = 1.5 + \left(\frac{T_i}{ZT_e}\right)\left(0.85 + 0.135\left[\ln\left(\frac{r_p}{\lambda_D}\right)\right]^3\right) \tag{4.11}$$

The electron temperature and density were thus computed using either (4.1) or (4.7) - (4.10) depending on the ratio of r_p/λ_D. Other possible sources of error in calculating the electron temperature and density are discussed in the Error Analysis section in the following chapter.

4.7 Crossed Electrostatic Probe Velocity Measurement

In a flowing plasma, the ion current collected by the probe is a function of the angle between the longitudinal probe axis and the plasma velocity vector. Assuming a Maxwellian velocity distribution and a thin cylindrical sheath, the current collected in a flowing plasma by a cylindrical probe is given by [45]

$$I = \left(\frac{kT}{2\pi m}\right)^{1/2} n_e e A \frac{2}{\sqrt{\pi}} \exp(-(\kappa)^2) \sum_{n=0}^{\infty} \left(\frac{\kappa^n}{n!}\right)^2 \Gamma\left(n + \frac{3}{2}\right) \tag{4.12}$$

where $\kappa = v/c_m \sin(\theta)$ and Γ is the gamma function. The ratio v/c_m is the ratio of the local flow velocity to the most probable ion thermal speed ($c_m = (2kT_i/m_i)^{1/2}$) and θ is the angle between the probe axis and the velocity flow vector. When the probe is aligned with the flow velocity, eqn (4.12) reduces to

$$I_{\parallel} = n_e e A_{\perp} \left(\frac{kT}{2\pi m}\right)^{1/2} \tag{4.13}$$

The ratio of the current collected by both probes is thus given by

$$\frac{I_\perp}{I_\parallel} = \frac{2}{\pi^{1/2}} \frac{A_\perp}{A_\parallel} \exp -(v/c_m)^2 \sum_{n=0}^{\infty} \left[\frac{(v/c_m)^2}{n!} \right]^2 \Gamma \left(n + \frac{3}{2} \right) \tag{4.14}$$

At supersonic flow velocities, a wake area is formed at the back of the perpendicular probe thus reducing the probe area by a factor of π [46, 47]. A plot of equation (4.14) is shown in figure 4.3. It can be seen that a velocity ratio of 2.8 corresponds to a current ratio of 1.

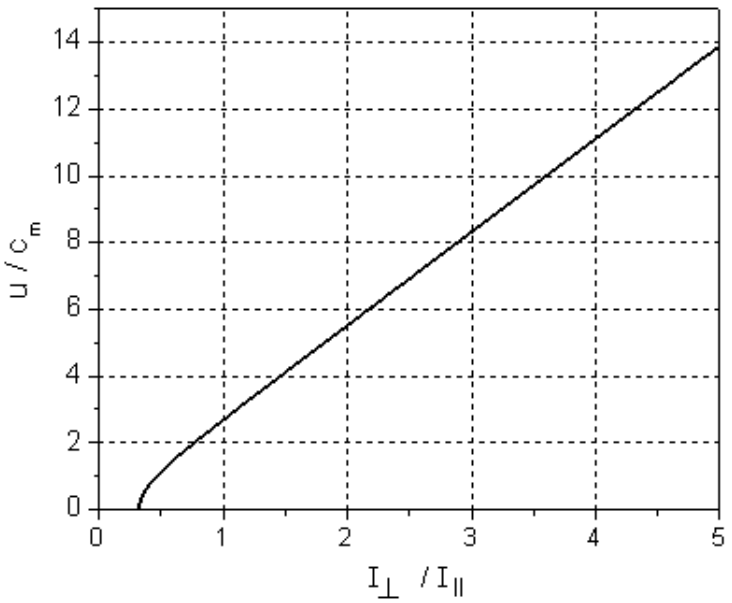

Figure 4.3: Velocity ratio (flow velocity to most probable speed) vs. the ratio of perpendicular to parallel probe currents.

When $I_\perp/I_\parallel > 1$, the flow velocity can be determined from the perpendicular probe measurement [39]. This can be seen by taking the limit of equation (4.12) as the velocity ratio v/c_m goes to infinity. Dividing both sides of (4.12) by $\kappa\sqrt{2kT_e/m_i}$ yields

$$\frac{I_\perp}{Zen_e v} = \frac{1}{\pi} \frac{\exp(-(\kappa)^2}{\kappa} \sum_{n=0}^{\infty} \left(\frac{\kappa^n}{n!} \right)^2 \Gamma(n + 3/2) \tag{4.15}$$

A plot of (4.15) is shown in Fig. 4.16. It can be seen that for $v/c_m > 2$, the current ratio reaches a constant value of $1/\pi$, reducing (4.15) to

$$\frac{I_\perp}{Zen_e v} = \frac{1}{\pi} \tag{4.16}$$

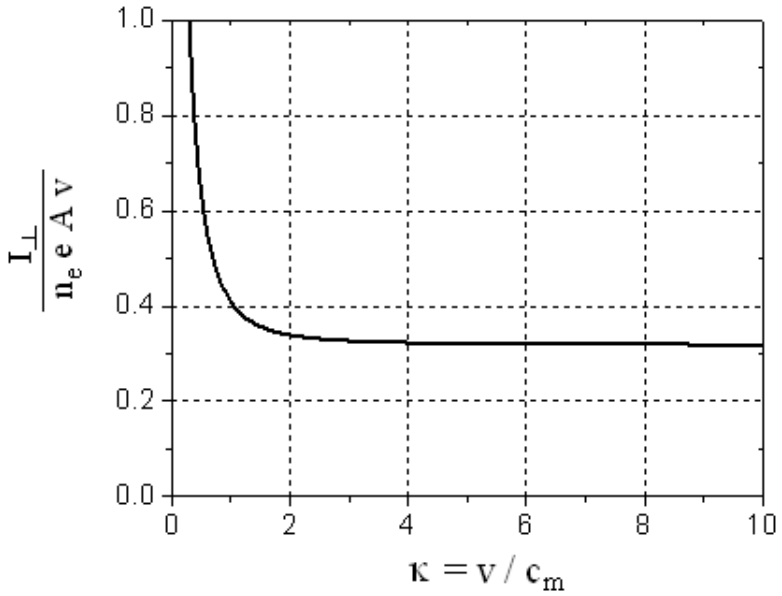

Figure 4.4: The current ratio reaches an asymptotic value of $1/\pi$ as the velocity ratio goes to infinity.

By examining figure (4.4), it can be seen that equation (4.16) is valid when $I_\perp/I_\parallel > 1$.

4.8 Magnetic Field Measurements

A magnetic field probe is used to measure the time varying magnetic field within the discharge region of the plume. A "b-dot" probe is simply a small coil of wire encapsulated within a thin glass sheath. The voltage induced on the coil is proportional to the number of turns n, coil area A_{coil}, and the time rate change of the magnetic field

$$\phi = -NA_{coil}\frac{dB}{dt} \tag{4.17}$$

The probe used in the present study consists of 3 turns of # 36 magnet wire. The coil has a diameter of 0.9 mm and is enclosed within a 1.4 mm Pyrex tube (Figs. 4.5 and 4.6). The probe is radially swept throughout the discharge by manually moving it between tests. The

signal is highly repeatable and is unaffected by the thin layer of gallium deposited on the outside of the Pyrex sheath after testing.

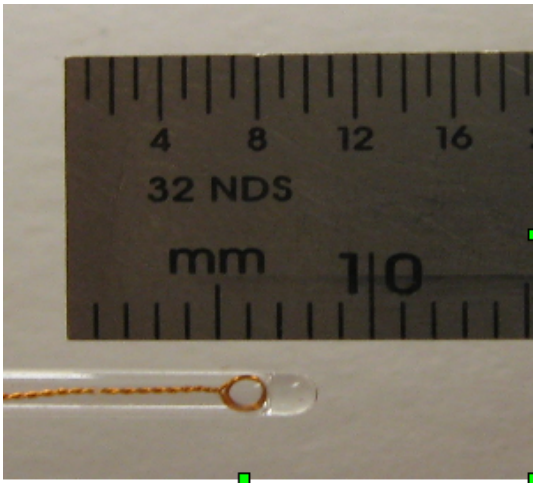

Figure 4.5: Three turn magnetic field probe probe enclosed within 1.4 mm Pyrex tube.

The two chief parameters in the design of the probe coil are its radius and the number of turns. In order to keep the probe as small as possible, these two parameters are kept as small as physically possible. Additionally, the coil inductance is proportional to the number of turns squared, so this provides another incentive to keep the probe small. This is somewhat offset by the reduced sensitivity of using a probe with a small diameter (Eqn. 4.17). Fortunately, this was not a concern in the present experiment due to the large current levels involved and the relatively fast rise time.

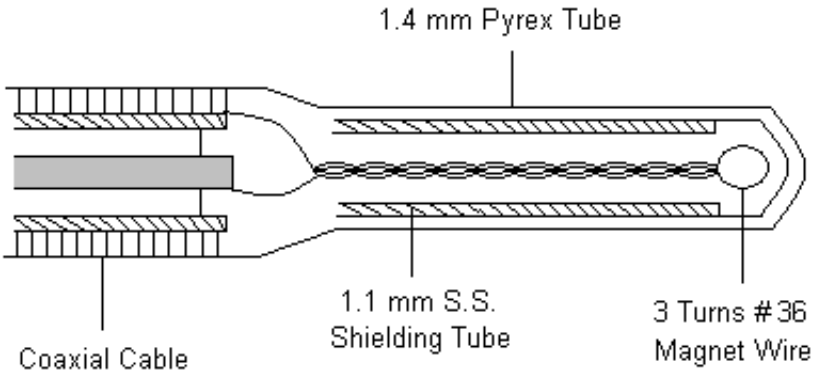

Figure 4.6: Schematic of magnetic field probe.

Chapter 5

Experimental Results

5.1 Introduction

Tests were initially conducted using a 5 mm central gallium (99.999% purity) anode with discharge current levels ranging from 20 - 54 kA. However, the ejection of gallium macroparticles (observed from post-firing mass bit measurements) led to a series of design changes. It was found that macroparticle ejection was unavoidable when using a central anode, therefore the electrode polarity was reversed. The gallium cathode radius was then increased until tests could be conducted above 20 kA without sputtering of the electrode. The inner diameter of the stainless steel electrode was initially 22.6 mm, and was later increased to 30 mm. The bulk of tests were thus conducted using a electrode radius ratio of 3.4 (= 30/8.7) at current levels ranging from 5.6 - 22.6 kA. A summary of the testing conditions are summarized in Table 5.1. The PFN charging voltage was varied in 50 Volt increments with a maximum input energy of 270 J. The discharge currents and instantaneous power levels in the table correspond to peak values taken at t = 45 μs.

Table 5.1: Summary of testing conditions using a 8.7 mm central cathode.

V_o, V	E_o, J	P_{in}, MW	I, kA	ψ, A^2-s	Z_{arc}, mΩ
150	50	0.2	5.6	3.6×10^3	7.2
200	88	0.4	7.3	7.3×10^3	7.1
250	138	1.4	14.2	1.3×10^4	6.8
300	198	2.1	17.8	2.0×10^4	6.7
350	270	3.3	22.6	3.0×10^4	6.5

5.2 Arc Voltage and Discharge Current

Current and voltage measurements across the discharge provide information on the thruster impedance, which is related to the efficiency of the thrust generating process. A representative current trace is shown in Fig. 5.1.

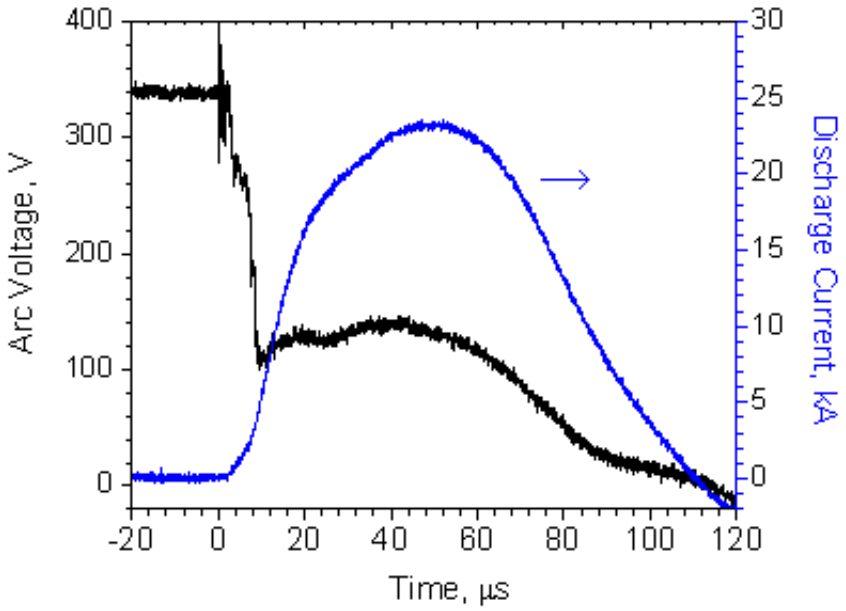

Figure 5.1: Representative discharge current and arc voltage trace taken at $E_o = 270$ J.

The transfer efficiency of the stored capacitor energy to discharge energy can be calculated using the time-varying waveforms

$$\eta_{tr} = \frac{\int_0^\infty I(t) \cdot V_{arc}(t)\ \mathrm{d}t}{\frac{1}{2}CV_o^2} \tag{5.1}$$

The PFN is well matched to the discharge and transfer efficiencies exceeding 90% are achieved under all testing conditions. The voltage-current characteristic exhibits a linear dependence as shown in Fig 5.2. Revisiting the scaling relations presented in Chapter 2, the linearity of the V-I curve suggests a quadratic dependence of the ablated mass with discharge current ($\beta = 2$). The arc impedance varies between 6 - 7 mΩ as shown in Fig. 5.3. The energy, arc impedance, and current action integral ψ are related by

$$E_o = \int I^2 Z_{arc} \, \mathrm{d}t = Z_{arc}\psi \tag{5.2}$$

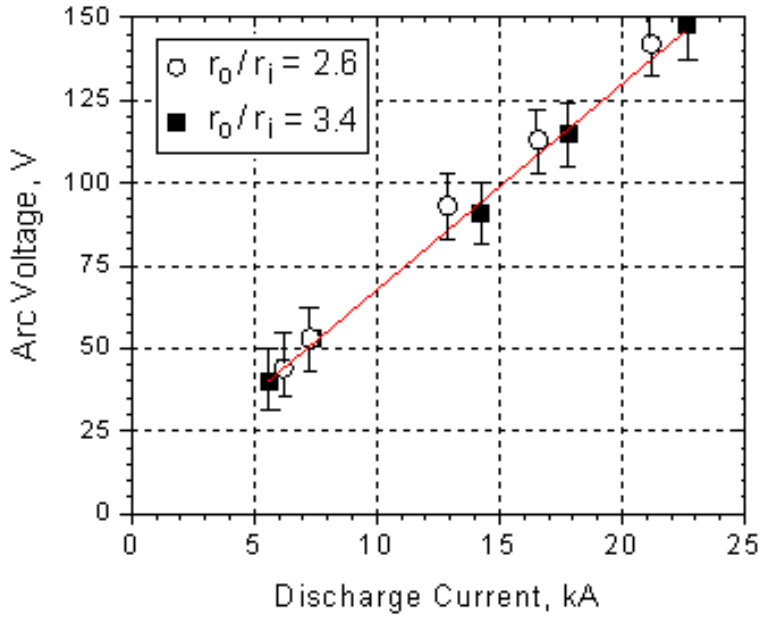

Figure 5.2: Comparison of arc voltage vs discharge current using two different electrode geometries.

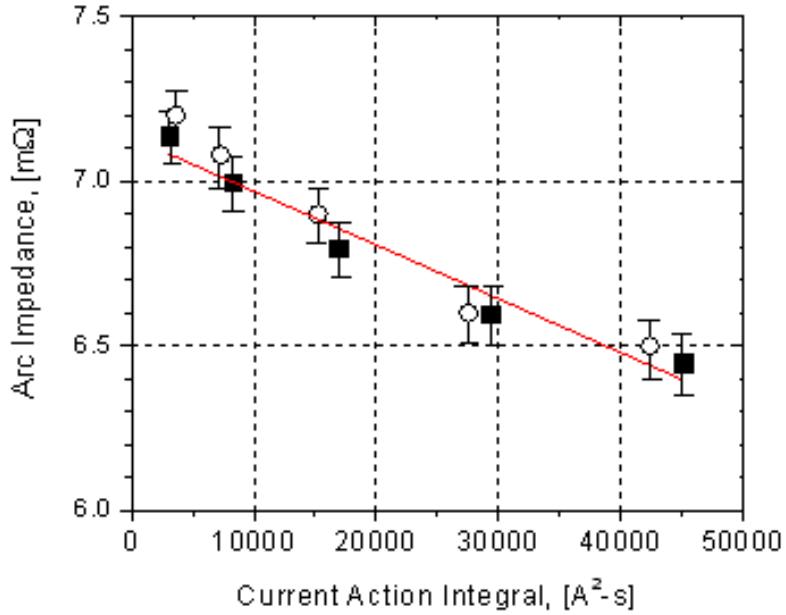

Figure 5.3: Arc impedance vs. current action integral for two different electrode geometries.

The total voltage across the discharge is the sum of the sheath voltage ϕ_c, electrothermal (resistive) contribution ϕ_t, and electromagnetic contribution ϕ_{EM} [30]

$$V_{arc} = \phi_s + \phi_t + \phi_{EM} \tag{5.3}$$

The electromagnetic voltage contribution is estimated as

$$\phi_{EM} = \frac{\text{electromagnetic thrust power}}{\text{discharge current}} = \frac{T_{EM}^2}{2\dot{m}I} \tag{5.4}$$

The electrothermal power input takes into account the ionization of the flow, internal excitation, random thermal and radiation processes which attend it, as well as Joule dissipation. The electrothermal contribution is expressed as

$$\phi_t = \frac{\dot{m}}{Im_i}\left(Ze\phi + \frac{3}{2}kT_e\right) \tag{5.5}$$

Table 5.2 shows the individual voltage components for each current level assuming a $Z = 3$ plasma, which is calculated from the triple probe data and the corresponding Saha calculations. The sheath potential is taken to be a multiple of the first ionization potential, a result that has been found experimentally in vacuum arc research for a wide range of electrode materials [48]. Despite these somewhat crude approximations, the calculated voltage is within 10% of the experimental value, and suggests that roughly 20 - 25% of the total voltage can be attributed to electromagnetic acceleration, while ionization constitutes the major energy loss mechanism.

Table 5.2: Components of calculated arc voltage.

I [kA]	ϕ_{EM} [V]	ϕ_t [V]	$2\phi_s$ [V]	V_{arc} [V] (calc.)	V_{arc} [V] (exp.)
5.6	7	17	12	36	40
7.3	10	23	24	57	53
14.2	15	47	36	98	91
17.8	22	50	36	108	115
22.6	30	66	36	139	148

5.2.1 Central Anode Data

Tests were initially conducted using a 5 mm central anode with discharge currents in the range of 20- 54 kA. Representative current and voltage traces are shown in Figs. 5.4 and 5.5. The V-I trace is shown in Fig. 5.6. The voltage carries linearly with the discharge current with arc impedances in the range of 6 - 7 mΩ. The electrical characteristics of the arc are identical for both electrode polarities; this was also observed with the carbon MPD [16].

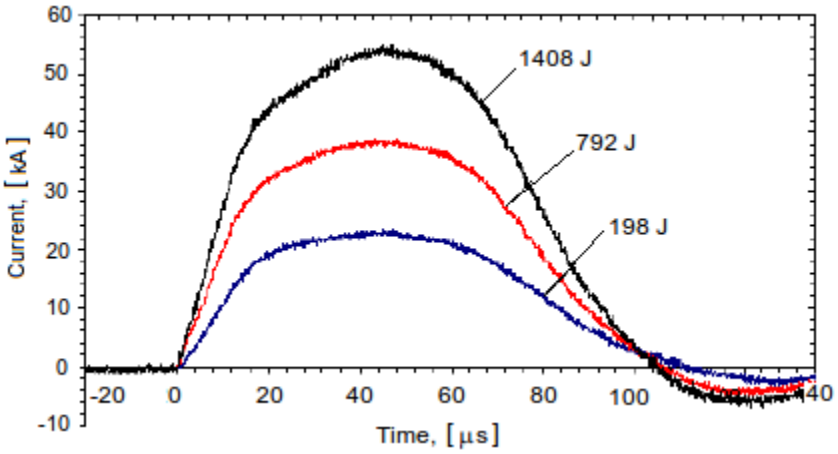

Figure 5.4: Discharge currents corresponding to charging voltages of 300, 600, and 800 V obtained using a 5 mm central gallium anode.

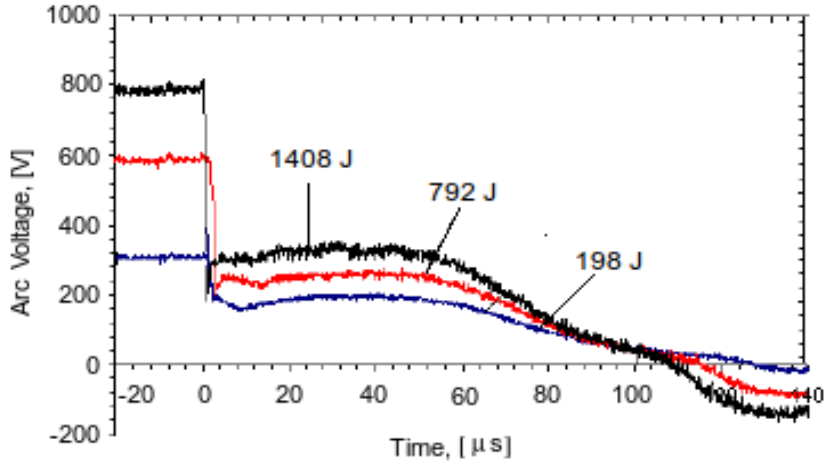

Figure 5.5: Arc voltages corresponding to charging voltages of 300, 600, and 800 V obtained using a 5 mm central gallium anode.

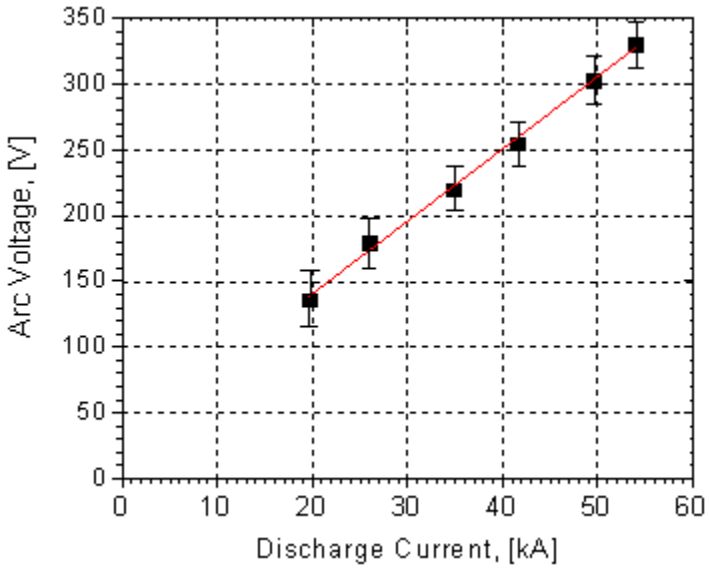

Figure 5.6: Arc voltage vs discharge current obtained using a 5 mm diameter gallium anode.

5.2.2 Possible Sources of Error

The voltage and current measurements are relatively straightforward, however there are several possible sources of error. During the course of experiments with the graphite MPD [16], it was found that a significant fraction of input energy was lost as resistive heating inside the carbon electrodes. This resistive loss not only led to artificially high arc impedance measurements, but also significantly lowered the efficiency of the thruster. While the resistivity of gallium is significantly lower than the carbon grade used in the graphite experiments (14×10^{-8} Ω-m vs. 1.77×10^{-5}), it is still informative to calculate the resistance of the gallium electrode. At high frequencies, the current through a conductor distributes itself such that the current is greater near the surface than at the core (Fig. 5.7). This "skin depth effect" thus effectively increases the resistance of the conductor through the reduction of area through which the current flows. The skin depth can be expressed as [49]

$$\delta = \sqrt{\frac{\eta}{\pi \mu f}} \tag{5.6}$$

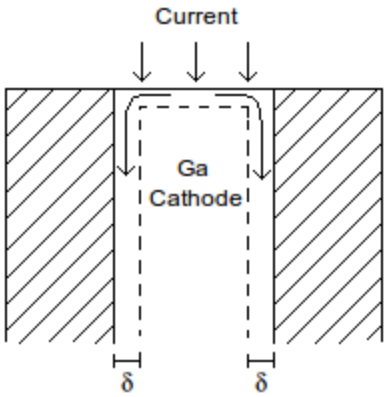

Figure 5.7: Illustration of skin depth effect within gallium cathode.

where f is the frequency and μ is the relative permittivity. Using the pulse rise time to estimate the frequency $f \sim (10\mu s)^{-1} = 0.1$ MHz, a skin depth of 0.6 mm is obtained. This increase in current density increases the resistance from 0.02 to 0.1 mΩ. Thus, for a discharge current of 23 kA, the resulting voltage drop through the gallium is only 2 V, less than 2% of the measured signal.

The largest source of difficulty in the arc voltage measurements was found to be related to the thruster arcing to the vacuum chamber during part of the pulse. When this occurred, a fraction of the discharge energy was not deposited into the central gallium electrode, leading to erroneous mass measurements and voltage-current data. An example is shown in Fig 5.8. The high frequency oscillations present in the voltage trace suggest that an insufficient amount of mass was being supplied to the arc (the "onset" instability). The low mass bit measurements corresponding to this voltage trace indeed show that the arc was striking the vacuum chamber as opposed to the gallium electrode. An insulating sleeve was placed around the outside of the thruster, and care was taken to insulate all edges present in the chamber. These precautions led to repeatable arc voltage measurements, and mass bits in close agreement with calculated values.

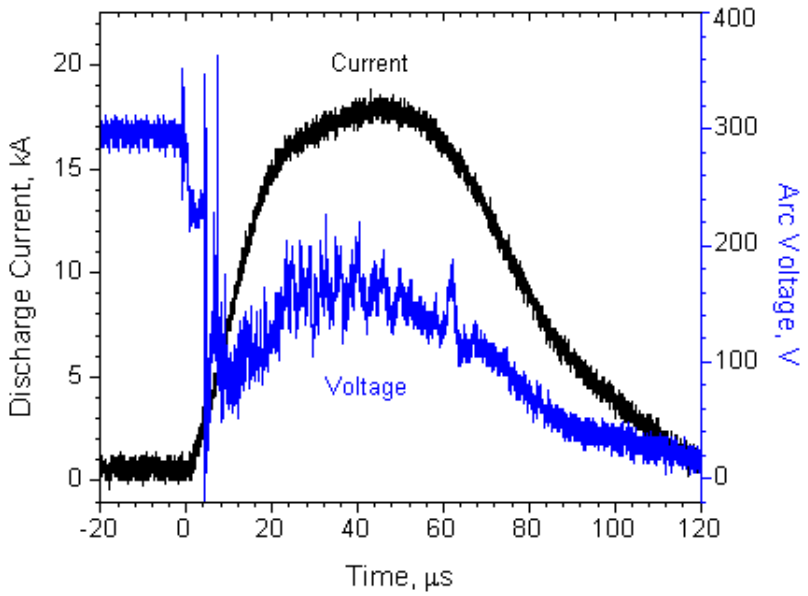

Figure 5.8: Current and voltage trace when outer electrode arcs to vacuum chamber.

5.3 Mass Bit Measurements

The mass ablated per pulse (mass bit) was measured by weighing the gallium and annular stainless steel electrodes before and after several hundred shots. It should be noted that while the mass measurement in principle is quite simple, previous investigators have experienced a number of difficulties. For the Teflon PPT and graphite MPD experiments, atmospheric moisture absorption led to inconsistent and unreproducible results. This was alleviated by heating the Teflon and graphite after firings to eliminate any water, and quickly weighing the specimens. Fortunately, neither solid gallium or stainless steel readily absorb water, and water absorption for boron nitride is on the order of 0.5 - 3.0%. While the solid gallium electrode did not visibly oxidize in between experiments, it was found that an oxidation layer does form on the surface of liquid gallium during the loading phase (Fig. 5.9). This oxidation layer persists when the gallium is initially frozen, and examination of the discharge current and voltage trace reveal this contamination layer affects the discharge properties. However, after 3-5 shots, the opaque oxidation layer disappeared and the current and voltage traces reverted to a consistent signal.

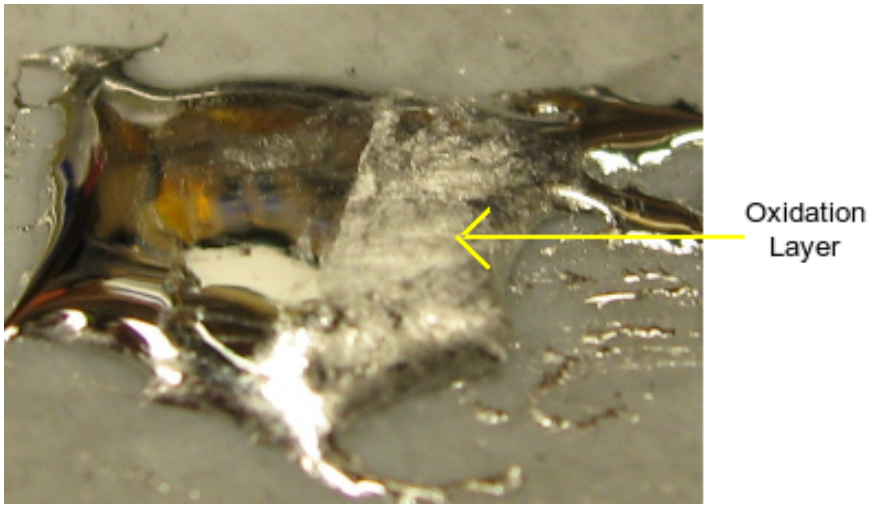

Figure 5.9: An opaque oxidation layer begins to form on the right side of the liquid gallium after being exposed to the air.

Tests were initially conducted using a central anode. It was found that gallium macroparticles were deposited on the annular electrode after firings (Fig 5.10). The corresponding mass bit is on the order of 10-20 mg, resulting in very low calculated exhaust velocities (e.g. 200 m/s). Macroparticle ejection is prevalent in vacuum arc thrusters and experimenters [50] have attempted to reduce their emission by a) active cooling of the cathode, b) application of external magnetic fields (to increase cathode spot motion), c) operation in a reactive gas background, and d) decreasing the current density. Decreasing the current density is the only viable alternative in the present experiment, and the current density was first reduced by simply lowering the discharge current level. When this failed to eliminate the macroparticles, the diameter of the gallium electrode was increased from 5 mm to 10 mm in 1 mm increments. This also proved unsuccessful in eliminating anode macroparticle ejection.

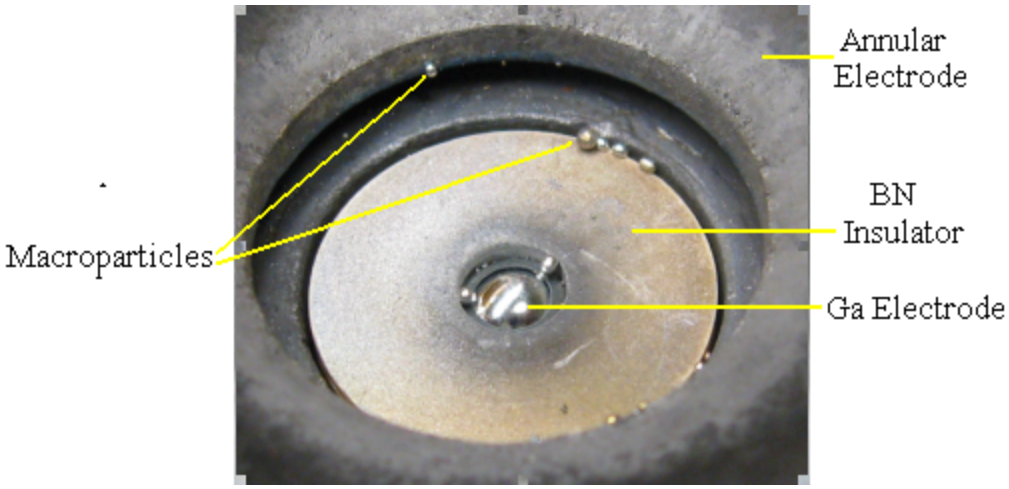

Figure 5.10: Photograph of gallium macroparticles deposited on insulator and annular electrode after 20 kA tests with a central anode.

Aluminum foam metal purchased from ERG Materials and Aerospace Corporation was then used as an underlying porous electrode and a small amount of gallium was used to coat the surface. It was hoped that by changing the underlying surface tension forces, macroparticle ejection could be avoided. Unfortunately, gallium macroparticles were ejected from the surface after a few shots leaving the underlying electrode severely damaged. Consequently, it was decided to reverse the discharge polarity. Tests were then conducted using a 5 mm cathode, and gradually increased until macroparticles were no longer present. A 8.7 mm diameter electrode provided the smallest diameter at which macroparticle ejection was avoided. Still photographs comparing the two different polarities are shown in Fig 5.11.

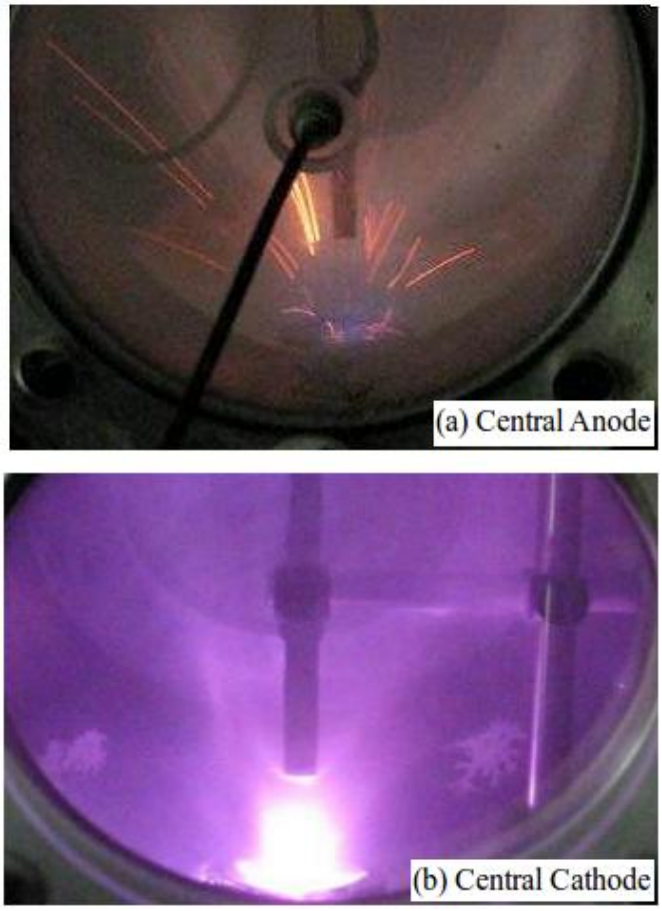

Figure 5.11: Comparison of macroparticle ejection with electrode polarity.

The Mettler AG245 scale used to weigh the electrodes has a resolution of 0.1 mg, therefore it was desired to ablate at least 10 mg in between tests. The PFN takes roughly 30 seconds to charge, and the small amount of gallium ablated per pulse (0.05 - 0.3 mg) suggests that several hundred shots are necessary to ablate a measurable amount of mass. The set-up was automated as follows. An HP 3312A function generator capable of pulse rates as low as 0.01 Hz was used to trigger a HP 8011A pulse generator. The HP pulse generator in turn, provides the 15 V TTL pulse necessary to trigger the spark plug (and thus discharge the capacitors). Therefore, the function generator was set to fire every 30 seconds and the voltage on the power supply was adjusted accordingly. A direct count 555 IC timer was connected in series with the function generator, and this proved to be a reliable and repeatable method of triggering the discharge over the course of several hours (Fig. 5.12).

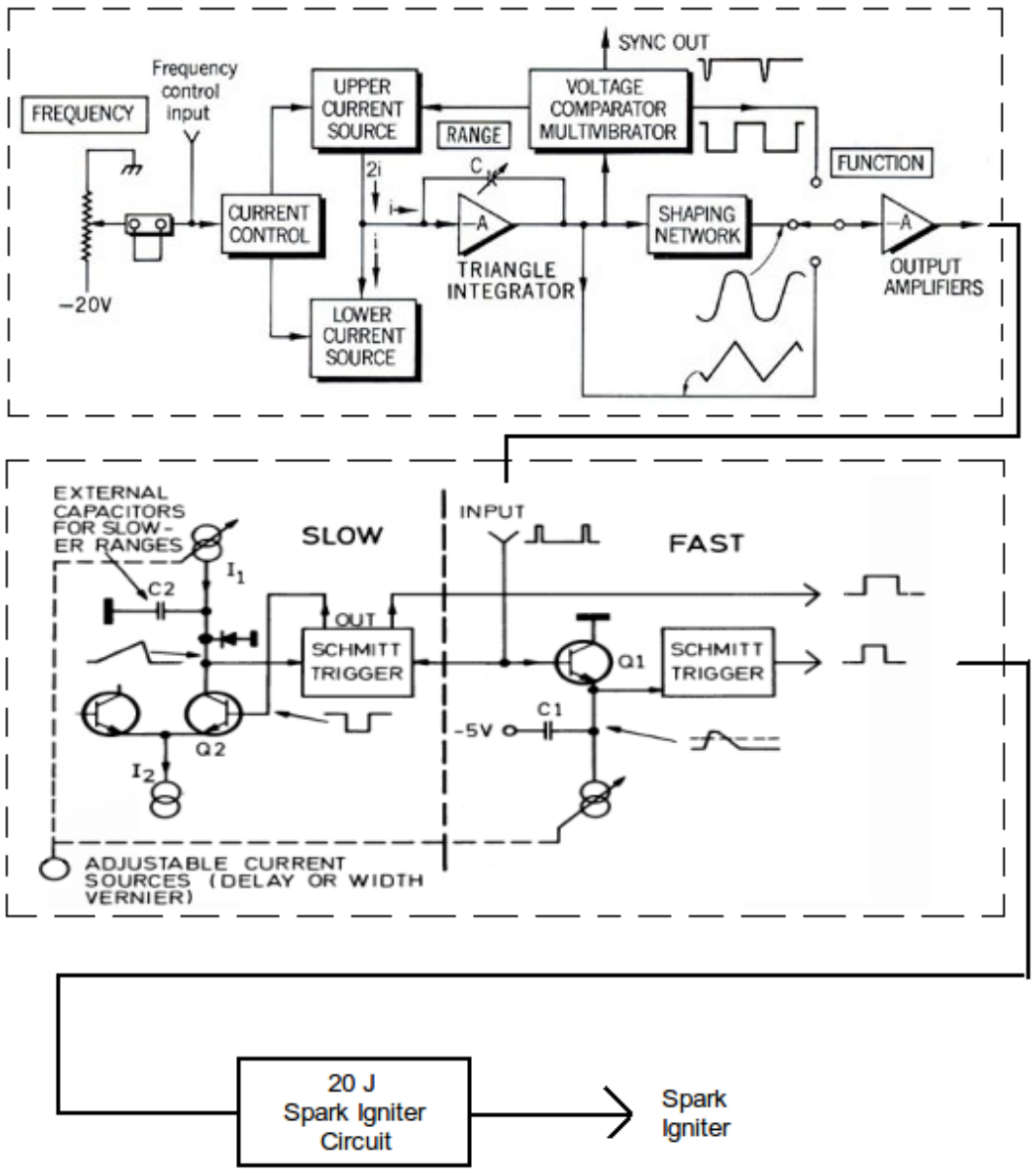

Figure 5.12: Schematic of circuitry used to trigger the spark igniter.

The mass ablated per per pulse plotted against the current action integral is shown in Fig 5.13. Tests were repeated 10 times at each energy level, and the ablated mass measurements were found to be highly repeatable. The mass of the annular stainless steel electrode decreased slightly after each test run. However, the total amount of mass lost (i.e. 0.3 mg after 250 shots) was small compared to the total mass of ablated gallium. The linearity of the plot is consistent with the V-I plot and also yields a mass ablation coefficient of $\beta = 2$.

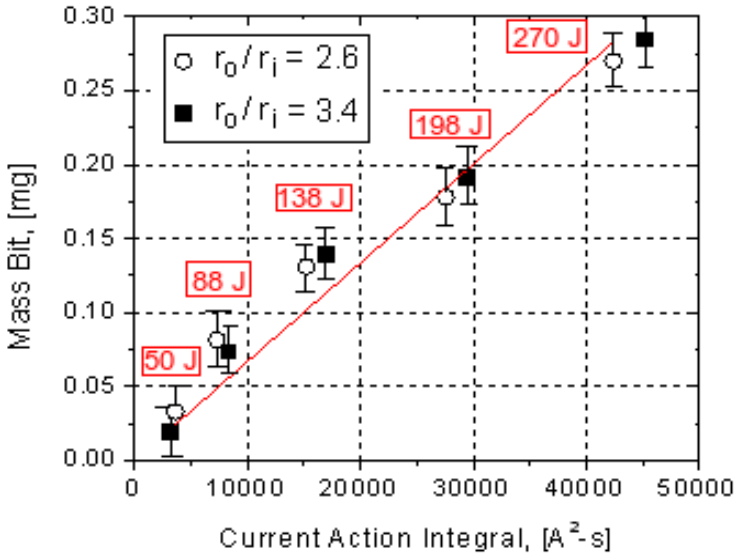

Figure 5.13: Ablated mass per pulse vs. current action integral, with corresponding PFN energies.

The erosion rate can be calculated from the mass bit and discharge current data using

$$E_r = \frac{m}{\int_0^\infty I \, \mathrm{d}t} \tag{5.7}$$

Equation 5.7 yields an erosion rate of 196 μg/C. This is roughly 40$\times$ higher than the tungsten erosion rate found in MPD thrusters [51]. This can be explained by the current conduction mechanism at the cathode surface. Refractory electrodes are able to reach a much higher surface temperature, which allows higher thermionic emission. Non-refractory materials are unable to reach such temperatures, and vaporization of the cathode material must take place to provide the arc with a sufficient number of charge carriers. The differences between refractory and non-refractory materials are discussed in detail in Chapter 6.

5.4 Emission Spectroscopy

The emission spectra were obtained at energy levels ranging from 85-270 J. Emission from neutral, singly, and doubly ionized Ga species were observed in the discharge. Iron, removed

from the outer electrode, was also obtained. Spectra from the 85 and 20 J cases are shown in Figs. 5.14 and 5.15. They are largely similar, however the 270 J case exhibits several iron lines as well as additional Ga III lines.

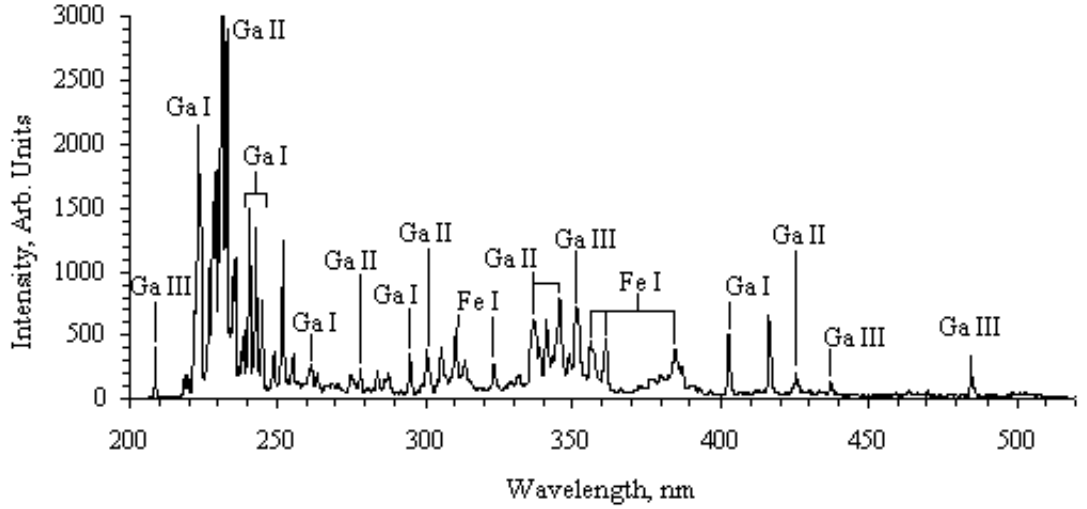

Figure 5.14: Emission spectrum of gallium plasma plume obtained at E = 85 J

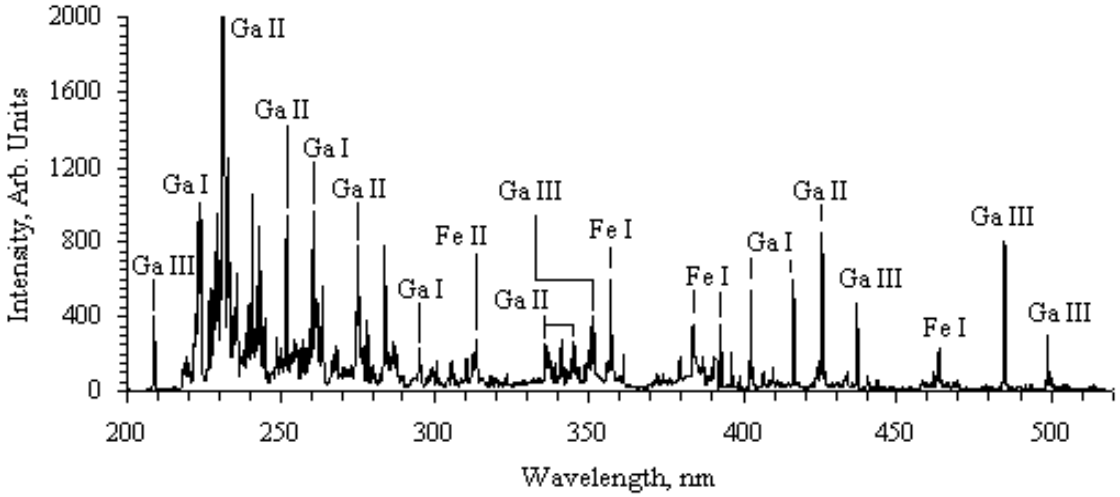

Figure 5.15: Emission spectrum of gallium plasma plume obtained at E_o = 270 J.

Table 5.3: Neutral and ionic gallium species present in 22.6 kA arc discharge.

Specie	Wavelength [nm]	Upper Energy Level [cm^{-1}]	Lower Level	Upper Level
Ga I	223.592	45071.75	$3d^{10}4s^24p$	$4s^29s$
Ga I	229.786	44332.27	$3d^{10}4s^24p$	$4s^28s$
Ga I	233.824	43580.44	$3d^{10}4s^24p$	$4s^26d$
Ga I	245.007	40802.86	$3d^{10}4s^24p$	$4s^25d$
Ga I	260.734	38341.72	$3d^{10}4s^24p$	$4s4p^2$
Ga I	294.417	34787.85	$3d^{10}4s^24p$	$4s^24d$
Ga I	403.298	24.788.53	$3d^{10}4s^24p$	$4s^25s$
Ga I	417.204	24788.53	$3d^{10}4s^24p$	$4s^25s$
Ga II	231.727	113842.30	4s4p	4s4d
Ga II	235.532	156327.39	4s4d	4s7f
Ga II	251.403	147485.46	$4p^2$	4s5f
Ga II	277.997	106662.37	4s4p	4s5s
Ga II	299.265	151923.93	4s5p	4s8s
Ga II	337.595	137342.57	$4p^2$	4s4f
Ga II	347.208	147520.34	4s5p	4s6d
Ga II	425.593	137332.28	4s4d	4s4f
Ga III	208.948	209148.01	$3d^{10}5p$	$3d^{10}7s$
Ga III	236.866	227637.2	$3d^{10}4f$	$3d^{10}7g$
Ga III	241.787	185432.59	$3d^{10}4d$	$3d^{10}4f$
Ga III	242.454	185432.59	$3d^{10}4d$	$3d^{10}4f$
Ga III	351.737	189187.72	$3d^{10}5p$	$3d^{10}5d$
Ga III	438.184	208254.14	$3d^{10}4f$	$3d^{10}5g$
Ga III	486.303	161304.40	$3d^{10}5s$	$3d^{10}5p$
Ga III	499.393	160765.56	$3d^{10}5s$	$3d^{10}5p$

5.4.1 Saha Equilibrium Calculations

The presence of doubly ionized gallium species in the emission spectra suggest a high degree of ionization within certain regions of the plume. The ionization state of the gallium plasma can be calculated using the Saha equation

$$\frac{n_e n_i^{Z+1}}{n_i^Z} = 2\left(\frac{2\pi m_e k T_e}{h^2}\right)^{3/2}\left[\frac{Q_i^{Z+1}(T_e)}{Q_i^Z(T_e)}\right]\exp\left(-\frac{\epsilon_i}{kT_e}\right) \tag{5.8}$$

where m_e is the electron mass, h is Planck's constant, and $Q_i(T_e)$ is the partition function, given by

$$Q_i = \sum_j g_j exp\left(-\frac{\epsilon_j}{kT_e}\right) \tag{5.9}$$

where the sum is performed over all j (electron excitation) states of the ion, and g is the statistical degeneracy of state j. The summation of the partition function over the energy states must be bounded. The National Institute of Standards and Technology (NIST) provides an online JavaScript applet which calculates the partition function for an input electron temperature [52]. The partition function is tabulated for Ga I-IV as a function of the electron temperature in Table 5.4.1.

Table 5.4: Partition functions for atomic and ionic gallium species.

T_e, eV	Ga I	Ga II	Ga III	Ga IV
1	7.80	1.02	2.00	1.00
2	42.25	1.56	2.10	1.00
3	103.56	3.52	2.51	1.04
4	168.89	8.04	3.44	1.23
5	229.62	15.40	5.14	1.71

The Saha equation can be extended to calculate multiple species by writing similar expressions for each degree of ionization, and substituting n_i^Z and Q_i^Z for the higher degree of ionization instead of the i-associated variable. A plot of the ionization fraction for the electron temperature and pressures of interest is shown in Fig. 5.16. The electron temperatures

of 0.8 and 3.6 eV were chosen because they correspond to the range of values found using the triple probe.

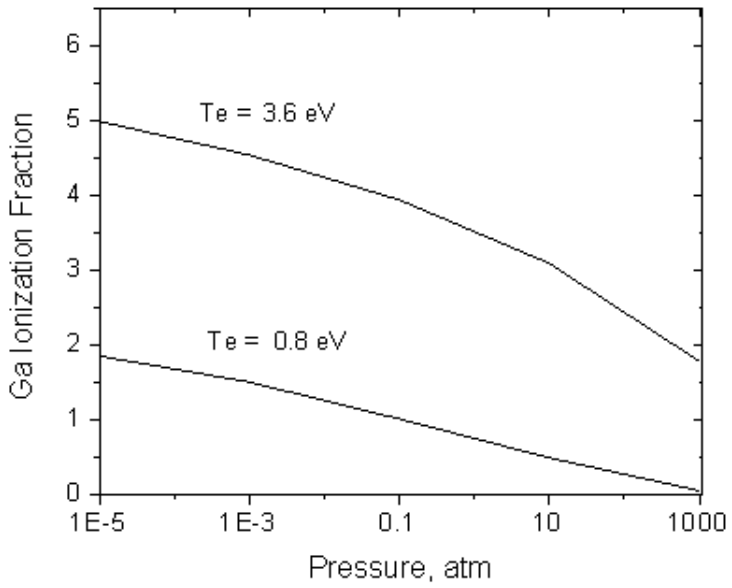

Figure 5.16: Calculated Ga ionization state as a function of plasma pressure.

5.5 Triple Langmuir Probe Measurements

A triple Langmuir probe is used to find the axial and radial variation of the electron temperature and density in the exhaust plume as a function of discharge current. The signal-to-noise ratio at the lowest current level (5.6 kA) is poor, and is therefore omitted. Initially, a GW Instek 30 A power supply connected through an isolation transformer was used to supply the floating probe voltage. However, the measured triple probe current exhibited high-amplitude oscillations, particularly towards the beginning of the pulse. This was due to the power supply being unable to supply the current on the microsecond time scale. Instead of the power supply, lead acid batteries ($I_{max} > 100$ A) were then installed and the oscillations disappeared. The probe locations for the axial and radial measurements are shown in Fig. 5.17.

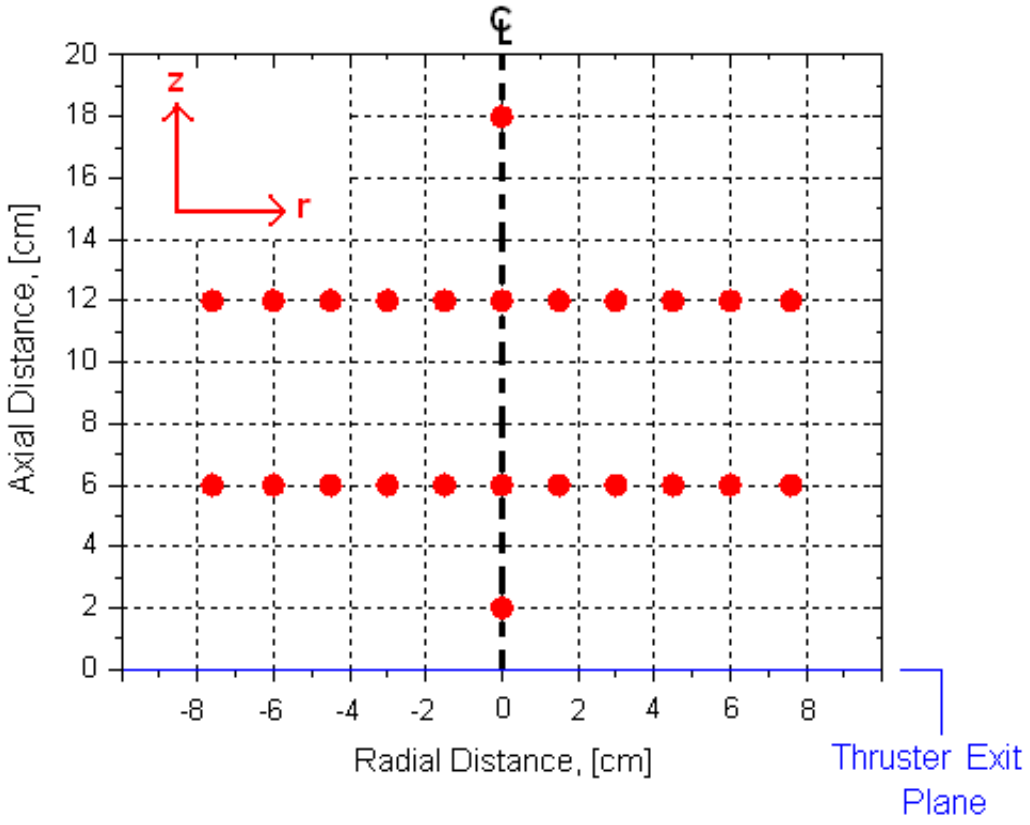

Figure 5.17: Location of triple probe for axial and radial measurements.

5.5.1 Axial Measurements

Data was obtained at axial locations of 2, 6, 12, and 18 cm from the exit plane of the thruster. Representative triple probe traces are shown in Fig. 5.18. The signals are both relatively noise free and highly repeatable. The axial variation of the electron density is shown in Fig. 5.19. The electron density has a peak value of 2.2×10^{22} m^3 two centimeters from the exit plane of the thruster, and drops by roughly a factor of 10 at an axial distance of 18 cm. The electron densities follow similar trends as the discharge current is decreased (Fig. 5.20).

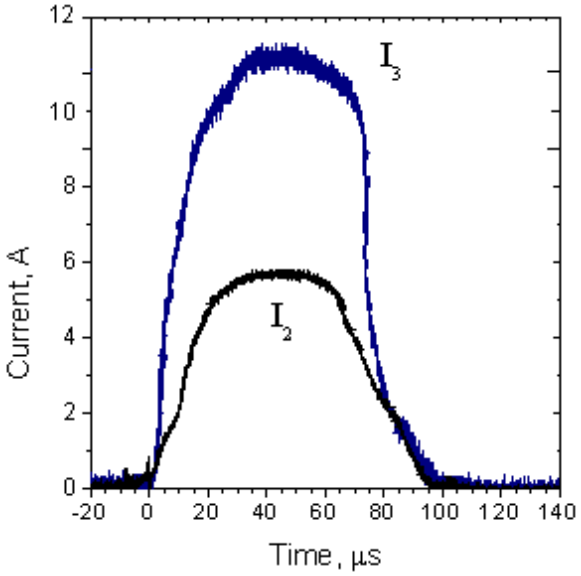

Figure 5.18: Triple probe current traces taken at z = 2 cm at $I = 22.6$ kA.

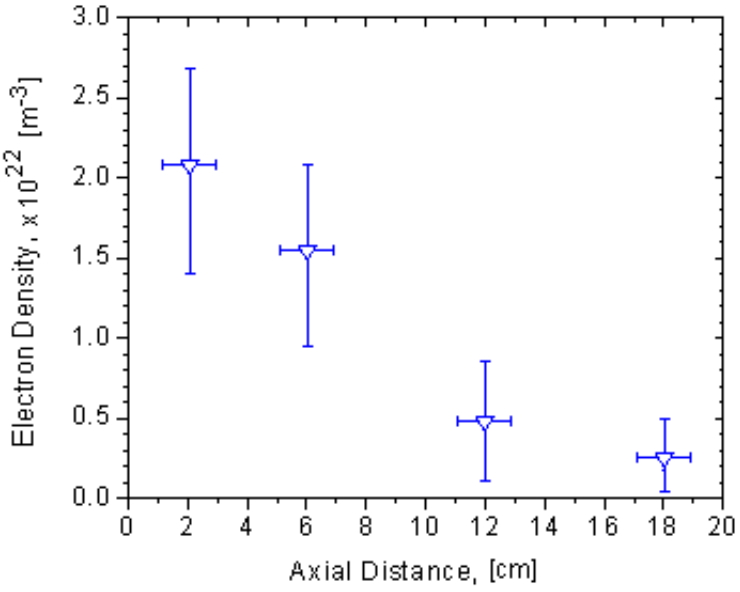

Figure 5.19: Axial distribution of electron density obtained at a discharge current of 22.6 kA.

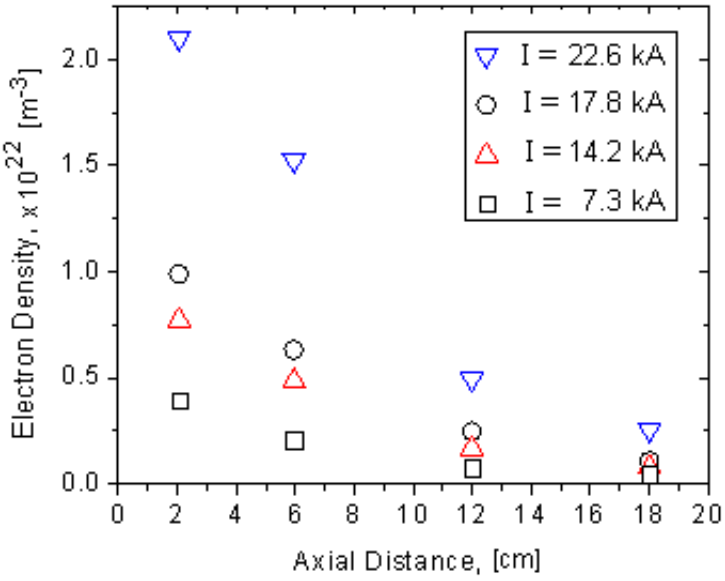

Figure 5.20: Axial distribution of electron densities (±40%) for different discharge current levels.

The plume divergence half-angle can be estimated by considering the continuity equation

$$n_e u_e A = \text{constant} \tag{5.10}$$

The divergence angle γ can be calculated by using the electron density and the exhaust velocity measured using the crossed perpendicular probe (Fig 5.21). Using Eqn. 5.10, it is found that the divergence angle increases from 16° at 22.6 kA to 19° at 5.6 kA.

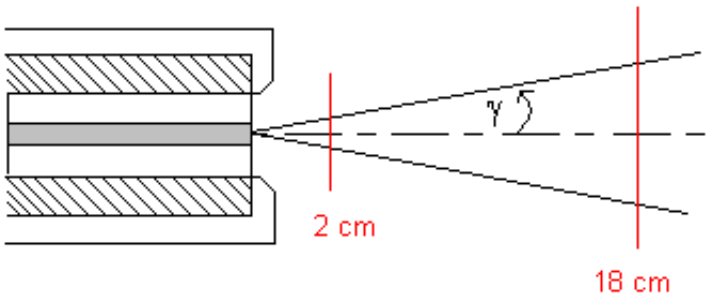

Figure 5.21: Plume divergence for GEM thruster.

The axial variation of the electron temperature for a discharge current of 22.6 kA is shown in Fig. 5.22. It is interesting to note that the electron temperature at each axial station

varies by less than 15% as the discharge current is decreased. This is a remarkably small change which is predicted through the electrical conductivity calculations presented below.

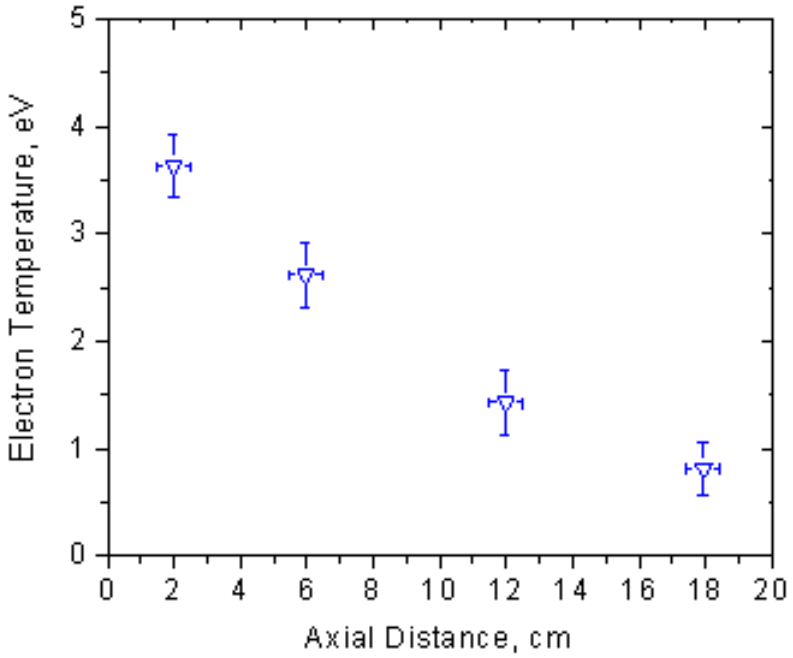

Figure 5.22: Axial distribution of the electron density obtained at I = 22.6 kA.

5.5.2 Radial Measurements

Radial measurements of the electron density and temperature were obtained in 1.5 - 2 cm increments at an axial distance of 6 and 12 cm from the face of the thruster. In order to minimize errors associated with probe misalignment, the triple probe was rotated in 10° increments (up to 60°) until the minimum current was obtained. To obtain a quantitative idea for the error associated with probe misalignment, we recall that the current collected by a cylindrical probe is dependent on the ratio of the flow velocity to the ion thermal velocity $\kappa = v/c_m \sin(\theta)$.

$$I = \left(\frac{kT}{2\pi m}\right) n_e e A \frac{2}{\sqrt{\pi}} \exp(-(\kappa)^2) \sum_{n=0}^{\infty} \left(\frac{\kappa^n}{n!}\right)^2 \Gamma\left(n + \frac{3}{2}\right) \tag{5.11}$$

The probe alignment current ratio as a function of θ is shown in Fig. 5.23. A plasma flow velocity of 20 km/s and ion temperature of 3.6 eV ($= T_e$) is used. For a 10° misalignment error, the error in the probe current is less than 5%, therefore the 10° probe increments should not lead to significant errors.

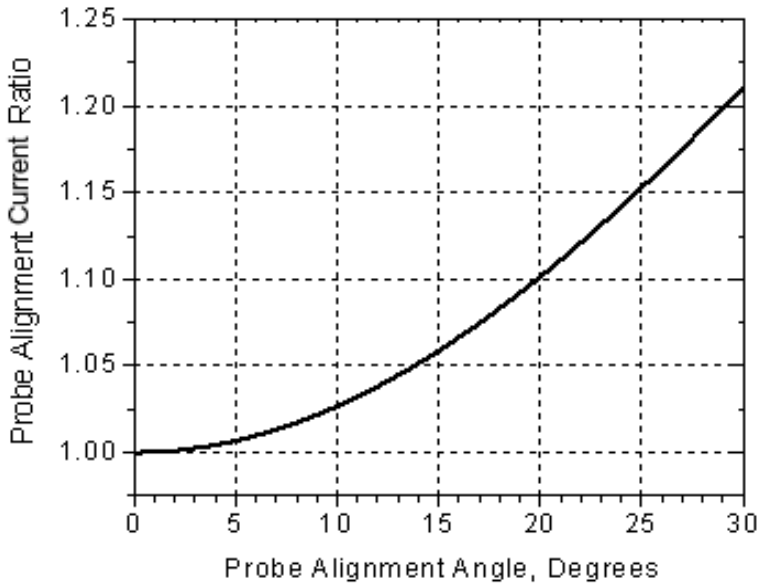

Figure 5.23: Error in collected probe current as a function of misalignment angle.

Figures 5.24 - 5.24 show the radial density profiles for the four different discharge current levels investigated. It can be seen there is a slight asymmetry in the density data; this is likely due to the spark igniter being slightly off-center. In all cases the full width at half max (FWHM) changes very little between the axial stations, this is evidence of a highly collimated ion beam created by electromagnetic acceleration. The radial temperature profile is shown in Fig. 5.28. The electron temperature is invariant with current so only the I = 22.6 kA profile is shown. The electron temperature (Fig. 5.28) drops by roughly 40% at $r = 2$ cm and remains constant as the probe is moved radially outwards.

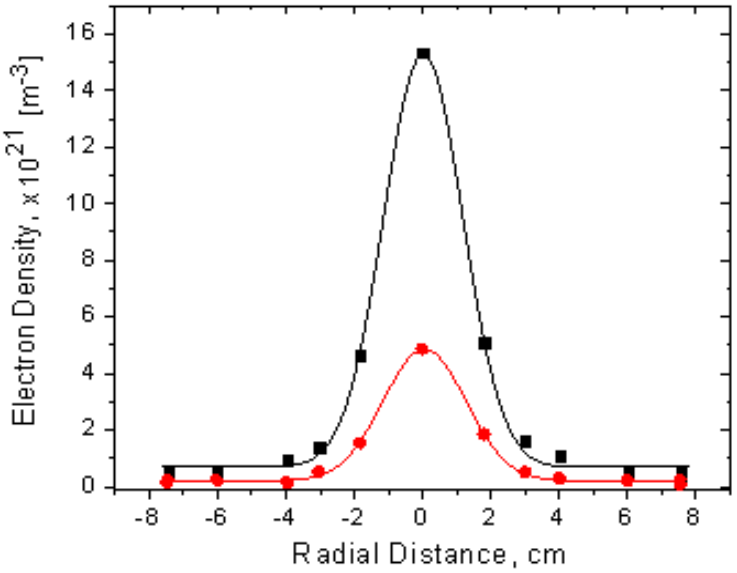

Figure 5.24: Radial variation of the electron density (±40%) obtained at I = 22.6 kA.

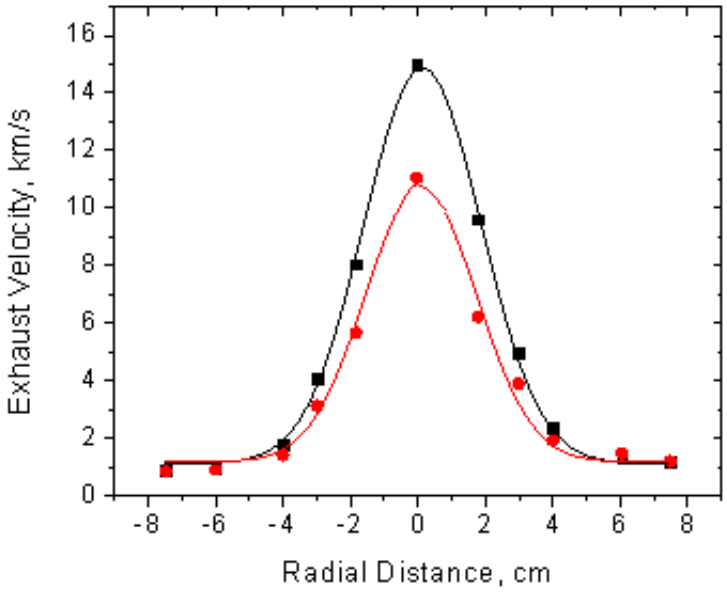

Figure 5.25: Radial variation of the electron density (±40%) obtained at I = 17.8 kA.

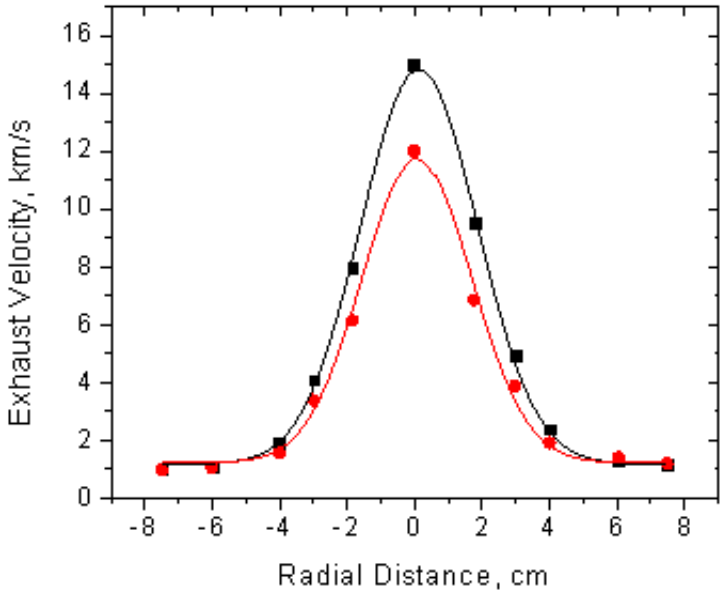

Figure 5.26: Radial variation of the electron density (±50%) obtained at I = 14.3 kA.

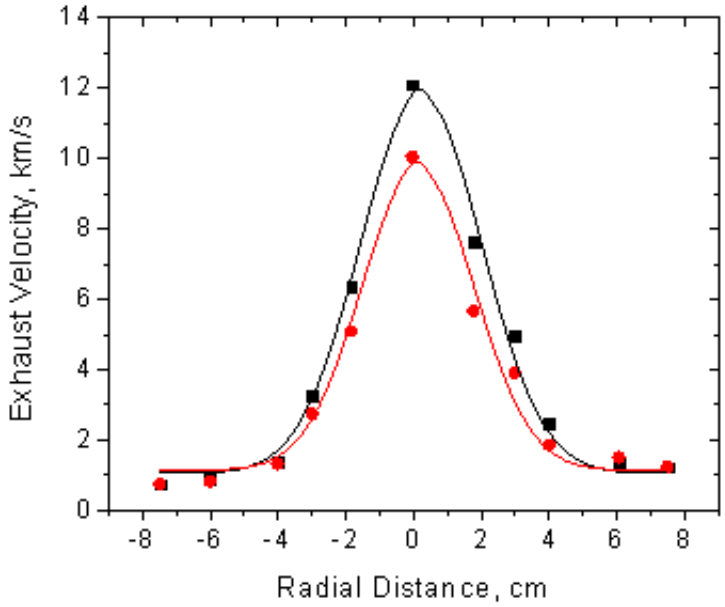

Figure 5.27: Radial variation of the electron density (±50%) obtained at I = 7.3 kA.

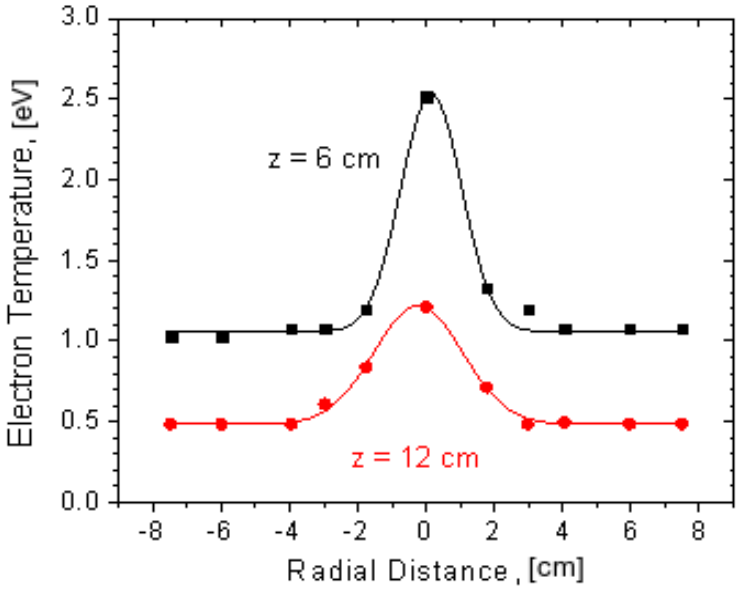

Figure 5.28: Radial variation of the electron temperature (±15%) obtained at I = 22.6 kA.

5.6 Scalar Conductivity and Temperature Calculation

The electron temperature can be calculated through use of Ohm's Law. To see this, we consider Coulomb's Law, which exhibits a $1/r^2$ dependence

$$E(r) = \frac{C_1}{r^2} \tag{5.12}$$

Noting the electric field is the gradient of the electric potential, the constant C_1 can be found

$$\Delta V = -\int_{r_i}^{r_o} \frac{C_1}{r^2}\, \mathrm{d}r \Longrightarrow C_1 = \Delta V \left(\frac{1}{r_i} - \frac{1}{r_o}\right)^{-1} \tag{5.13}$$

The current density is also assumed to follow a $1/r^2$ dependence

$$j = \frac{I}{\pi r^2} \tag{5.14}$$

Ohm's Law relates the current density to the electric fields

$$j = \sigma_o(\mathbf{E} + \mathbf{u} \times \mathbf{B}) + \frac{\Omega}{B}(\mathbf{j} \times \mathbf{B}) \tag{5.15}$$

The calculated hall parameter is small so the last term is neglected, and assuming u is radial, equations (5.12 - 5.15) yields

$$\sigma = \frac{I}{\pi \Delta V}\left(\frac{1}{r_i} - \frac{1}{r_o}\right) \tag{5.16}$$

The electron temperature is related to the scalar conductivity through the relation [53]

$$\sigma = \frac{e^2 n_e}{m_e \nu_{ei}} \approx 1.3 \times 10^4 \frac{T_e^{3/2}}{Z \ln \Lambda} \text{ (S/m)} \tag{5.17}$$

where ν_{ei} is the electron-ion collision frequency and Λ is calculated using

$$\Lambda = \left(\frac{8\pi\epsilon_o \lambda_D \varepsilon}{e^2}\right) \tag{5.18}$$

where ε is the relative kinetic energy of the particles before the collision. The electrode radii, discharge current, arc voltage and measured electron density can therefore be used to calculate the electrical conductivity and electron temperature. To be consistent with prior calculations, a $Z = 3$ plasma is used and the calculated and experimental electron temperatures are shown in the Table below.

Table 5.5: Comparison of calculated and experimental electron temperature taken at z = 2 cm.

I , kA	V_{arc}, V	Z_{arc}, mW	σ_o, S/m	T_e, eV (calc.)	T_e, eV (exp.)
5.6	40	7.2	7216	3.7	3.4
7.3	52	7.1	7317	3.7	3.4
14.2	97	6.8	7640	3.9	3.5
17.8	120	6.7	7754	3.9	3.5
22.6	148	6.5	7932	4.0	3.6

5.7 Velocity Measurements

Axial and radial velocity measurements were made as a function of discharge current. Both a crossed electrostatic probe and time of flight double probes were used to measure the

velocity, and are described below.

5.7.1 Crossed Electrostatic Probe Velocity Measurements

Recalling the discussion from Section 4.6, if the perpendicular probe current exceeds the parallel probe current then the following equation can be used to calculate the velocity

$$\frac{I_{\perp}}{Zen_e v} = \frac{1}{\pi} \tag{5.19}$$

This requirement is met for all operating conditions, thus Eqn. 5.19 is used to calculate exhaust velocity for both the axial and radial measurements.

5.7.1.1 Axial Probe Measurements

The axial perpendicular probe measurements for $I = 22.6$ kA is shown in Fig. 5.29. The crossed probe technique is subject to the same errors of the electron density, with error bars of 40%. The exhaust velocity for discharge currents from 7.3 - 22.6 kA is shown in the Fig. 5.30 below. At the three highest energy levels, the velocity varies by less than 10% (well within the experimental error). This experimental results is in agreement with the arc voltage and mass measurements, which predicted an invariant velocity for increasing current levels. Recalling the scaling relations from Chapter 2

$$P = IV_{arc} \propto \frac{1}{2}\dot{m}u_e^2;\ V_{arc} = I^{3-\beta};\ \text{and}\ u_e \propto I^{2-\beta} \tag{5.20}$$

It is seen that a constant exhaust velocity is consistent with a mass ablation exponent of $\beta = 2$.

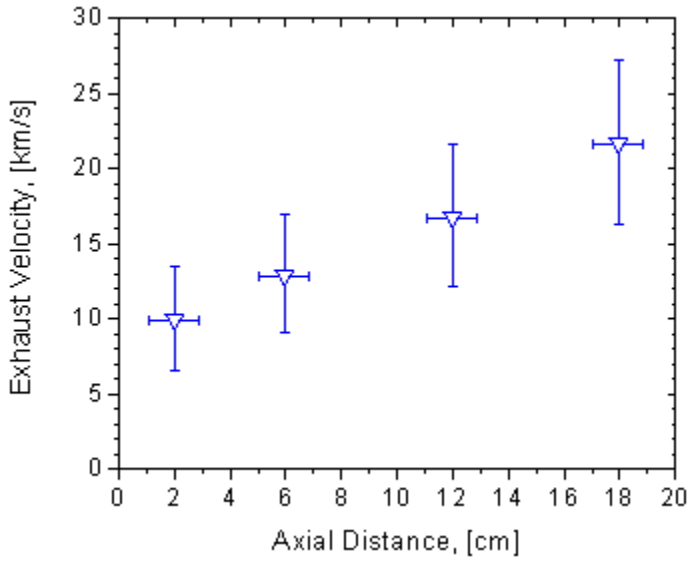

Figure 5.29: Axial variation of the exhaust velocity measured using crossed electrostatic probes for I = 22.6 kA.

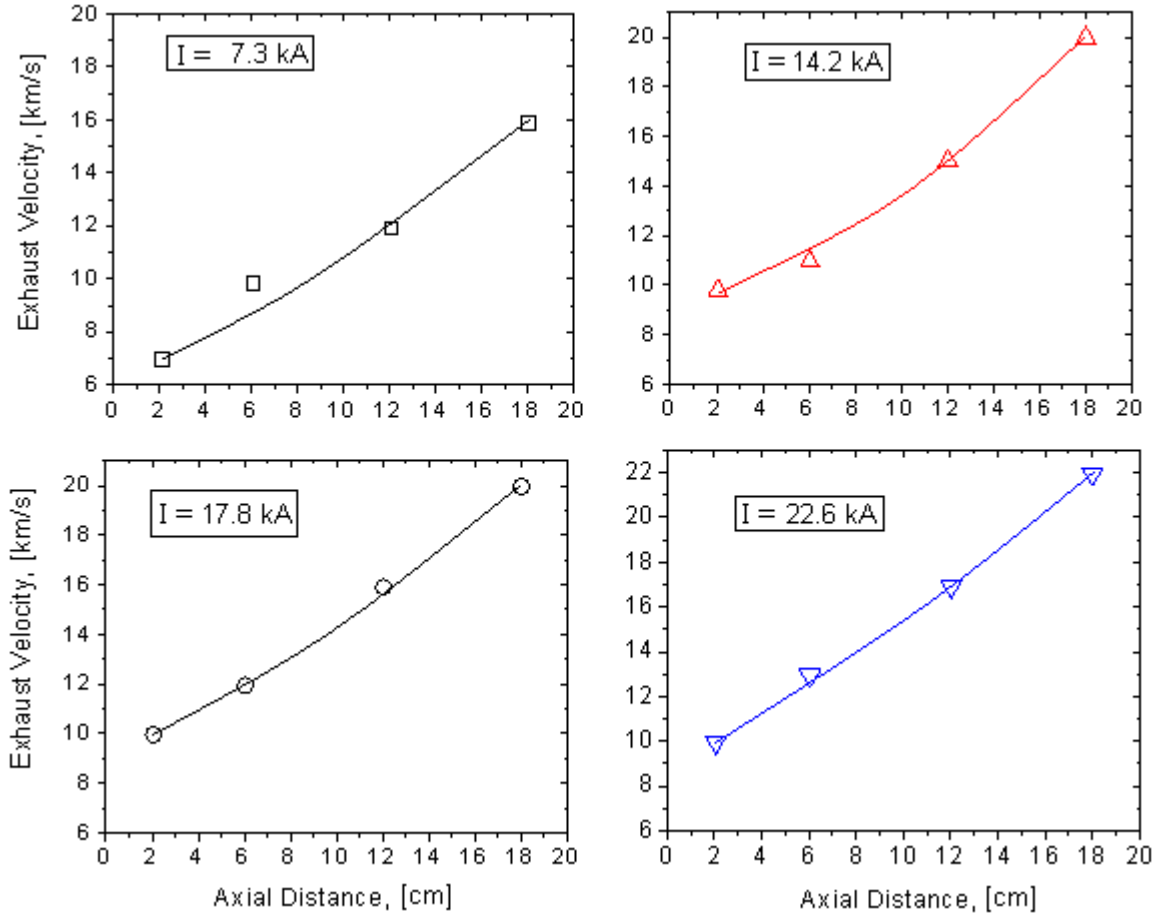

Figure 5.30: Axial variation of exhaust velocity (±40%) as a function of discharge current.

5.7.1.2 Radial Probe Measurements

The radial distribution of the exhaust velocity obtained generally show the same trends as the electron density data. The velocity is roughly 20 -30% higher than predicted using the continuity Eqn. 5.10, which is within the error bars of the measurements. It was found that the perpendicular probe current was more sensitive to the velocity vector alignment than the parallel probe; this is the largest source of error for the velocity measurements. Figures 5.31 to 5.34 show the radial velocity distribution for the four discharge current levels tested.

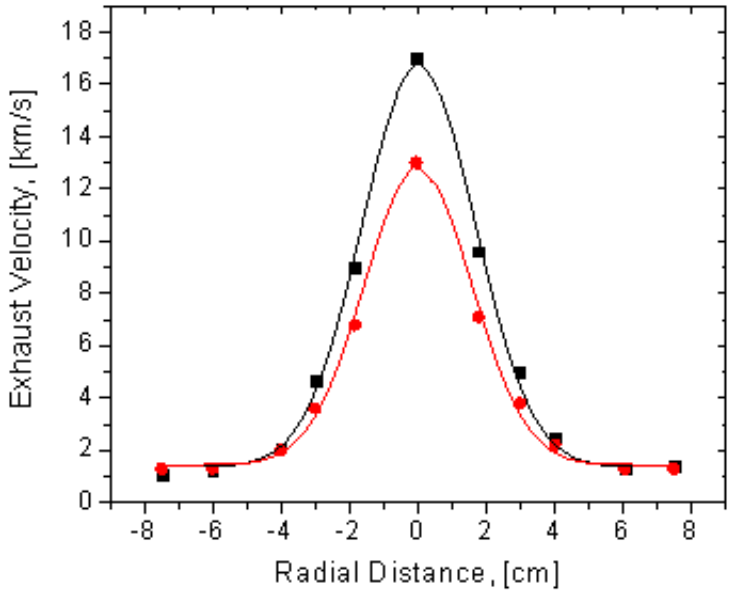

Figure 5.31: Radial profile of exhaust velocity (±50%) obtained at a current level of 22.6 kA.

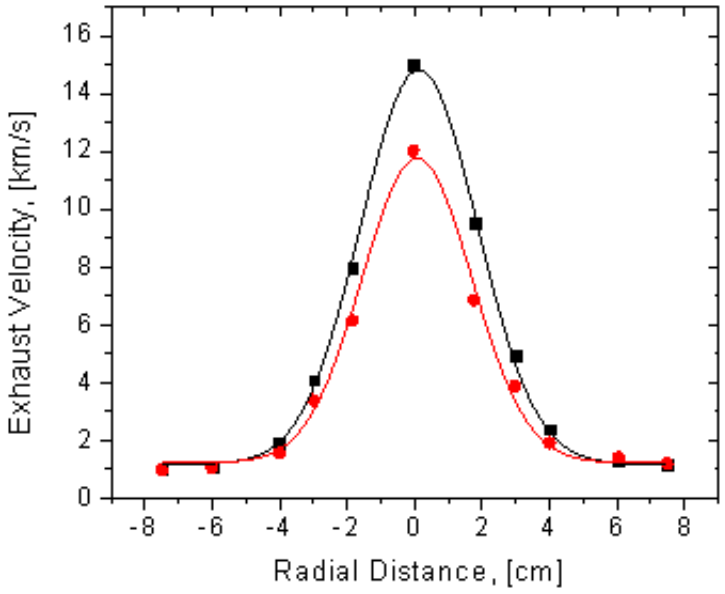

Figure 5.32: Radial profile of exhaust velocity (±50%) obtained at a current level of 17.8 kA.

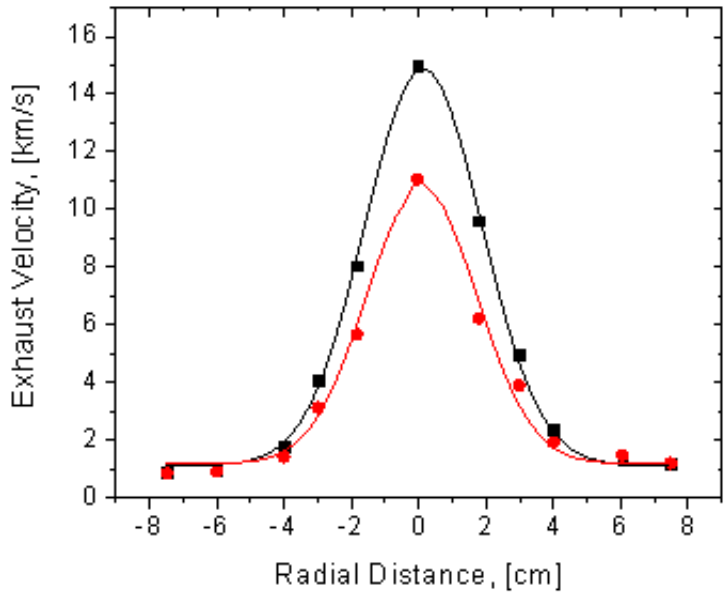

Figure 5.33: Radial profile of exhaust velocity (±50%) obtained at a current level of 17.8 kA.

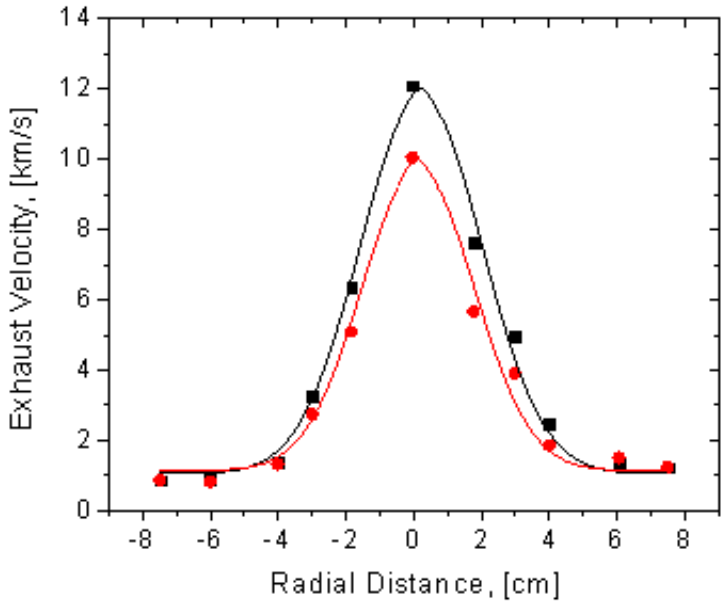

Figure 5.34: Radial velocity profiles (±50%) obtained at a current level of 7.3 kA.

5.7.2 Time of Flight Measurements

Axial velocity measurements were also made by using a pair of floating double probes. By fixing the distance between the probes (1 - 1.5 cm), local variations in the ion density can be used to calculate the ion velocity. By placing the probes perpendicular to the flow, it was found that the "distinguishing characteristics" used to calculate the velocity became much more prominent, particularly at the 12 and 18 cm positions (Fig. 5.35). Time of flight data was not taken at an axial position of 2 cm due to the lack of ion density fluctuations. The data was analyzed using the correlation analysis algorithm in Origin Pro.

The axial TOF measurements as a function of current is shown in Fig 5.36. The measured velocity decreases slightly with discharge current, however, the change mainly falls within the experimental error (30%). The experimental error is due mostly to the spread of data (precision error). Additionally, it is possible that a component of the ion acoustic wave motion may be superimposed on the plasma velocity. A comparison of the time of flight probe and time of flight measurements are shown in Fig 5.37.

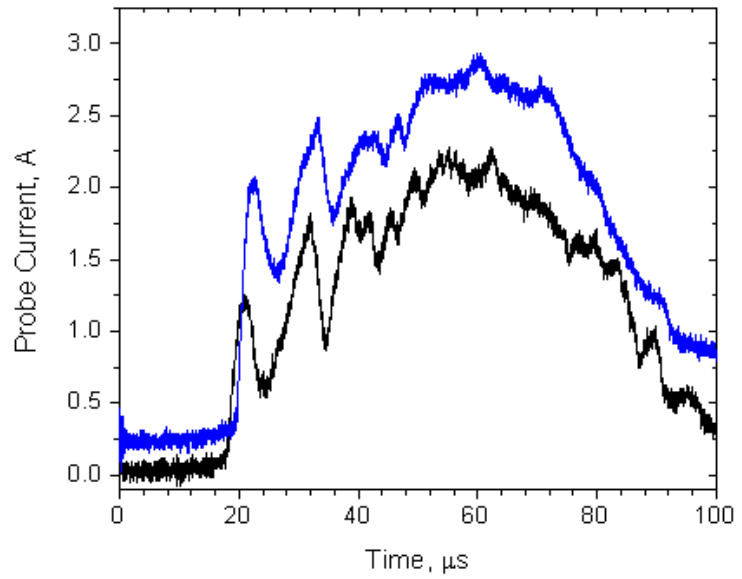

Figure 5.35: Perpendicular double probe traces obtained at an axial distance of 6 cm.

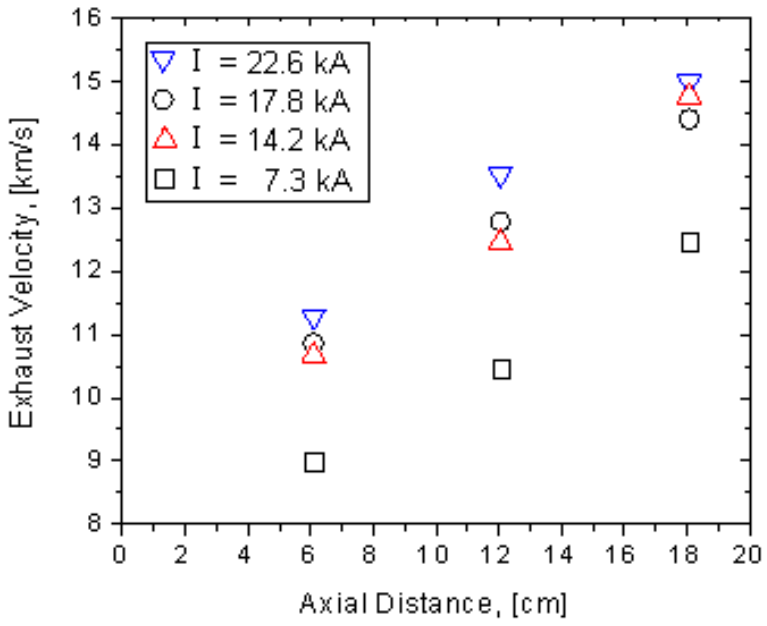

Figure 5.36: Axial TOF velocity data (±30%) for discharge currents in the range of 7.3 - 22.6 kA.

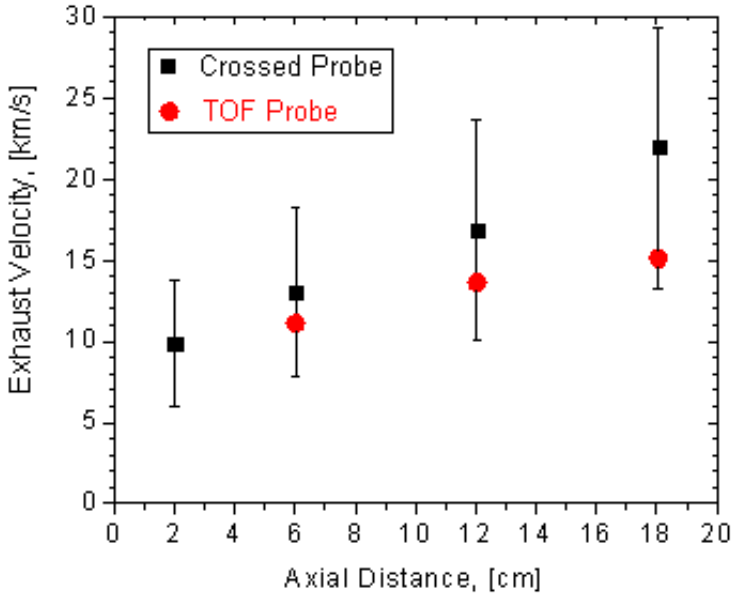

Figure 5.37: Comparison of crossed probe and TOF flight velocity measurements.

5.8 Comparison with Past Results

The trends in the measured electron temperatures and densities are in general accord with electromagnetic accelerators and experimental vacuum arc data. Tilley [37] used a triple probe to make radial measurements of the electron density and temperature for a 10 kW gas-fed MPD thruster. Temperatures in the range of 2 - 4 eV were found with densities on the order of 5 - 15 $\times 10^{18}$ m^{-3}. The temperature exhibited a flat radial profile which was largely invariant with the mass flow rate. The electron density slightly increased with the mass flow rate. These trends were also observed in MPD thrusters using spectroscopic measurements [54] and single probes [55].

Eckman et. al [38] used a triple probe to obtain radial and axial profiles of the electron temperature and density at energy levels of 5, 20, and 40 J in a Teflon PPT. Electron temperatures in the range of 2 - 4 eV were obtained, with electron densities in the range of $0.16 - 1.8 \times 10^{21}$ m^{-3}. Electron densities confirmed the asymmetry of the plume, while the electron density was found to vary little in the radial direction.

The electron density has been measured using infrared interferometry [56], electrostatic probes, and emission spectroscopy in vacuum arcs. The measurements generally show good agreement with each other with densities in the range of $10^{20} - 10^{22}$ m^{-3}. Puchkaraev [57] used floating probes placing within 0.1 to 0.5 mm for both Cu and W electrodes, and obtained an electron temperature of 4.6 - 5.8 eV. Sherman et. al [58] used a Langmuir probe for a 4.3 kA Cu arc to determine the electron temperature and density. Electron temperatures in the range of 4.5 to 6.0 eV were found near the cathode and anode, respectively. A spherical probe located in the center of the electrode gap found temperatures in the range of 2.9 - 3.7 eV.

5.9 Magnetic Field Measurements

Radial and axial magnetic field measurements were taken as a function of discharge current. Fig 5.38 shows a raw and integrated signal taken at a discharge current of 22.6 kA. A 0.1 μF capacitor was placed in parallel with the probe output to filter the high-frequency oscillations.

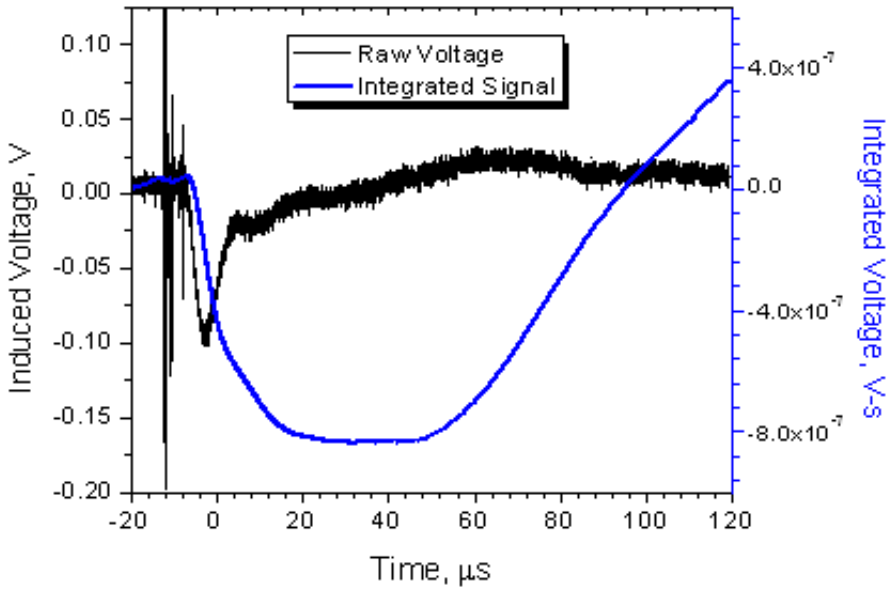

Figure 5.38: Raw and integrated magnetic field probe trace taken at a radial distance of 15 mm.

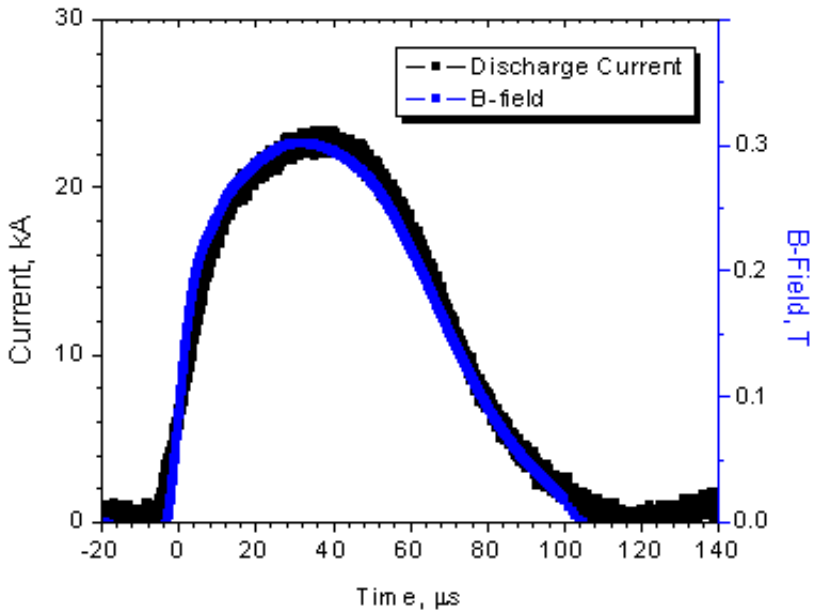

Figure 5.39: Discharge current and magnetic field probe trace.

Radial measurements were taken at a distance of ± 0, 4.35, 9.7, and 15 cm (Fig. 5.40). It was initially found that there was little variation in the amplitude of the radial measurements; this is likely due to the capacitance in coaxial cable. To minimize this effect, the oscilloscope was moved from the shielded screen room and mounted 1.5 feet from the chamber, thus cutting the total transmission line length from 26 ft to 2.5 ft.

From Maxwell's $\nabla \times \mathbf{B}$ relation, the self-induced field is purely azimuthal, with a radial magnetic field profile given by (assuming a uniform current density over the cathode surface)

$$B_\theta = \begin{cases} \frac{\mu_o I}{2\pi r_c^2} r & \text{for } r \leq r_c, \\ \frac{\mu_o I}{2\pi r} & \text{for } r \geq r_c. \end{cases} \tag{5.21}$$

Fig. 5.41 shows the radial profile of the magnetic field B_θ at a discharge current of $I = 22.6$ kA. The trends are consistent with Eqn. 5.21, and within 20%, the experimental error. The measured magnetic field is non-zero along the center-line, this is likely due to finite probe perturbation. The radial measurements were taken as a function of current, with the signals exhibiting the same trends and varying linearly with the current (Fig. 5.42).

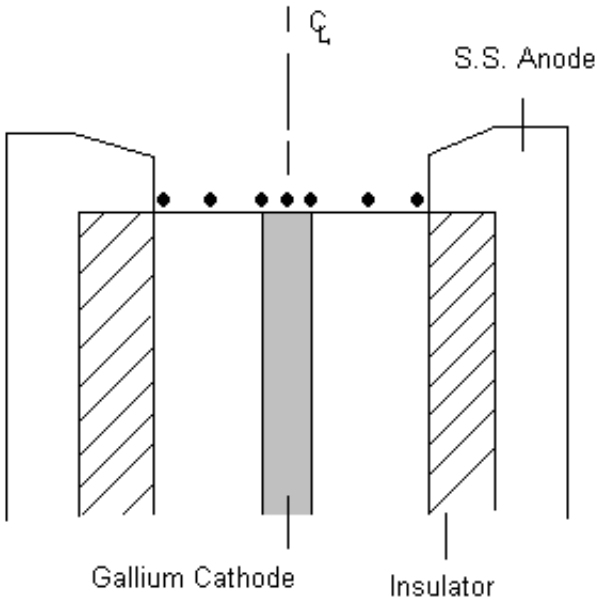

Figure 5.40: Radial magnetic field probe measurement locations.

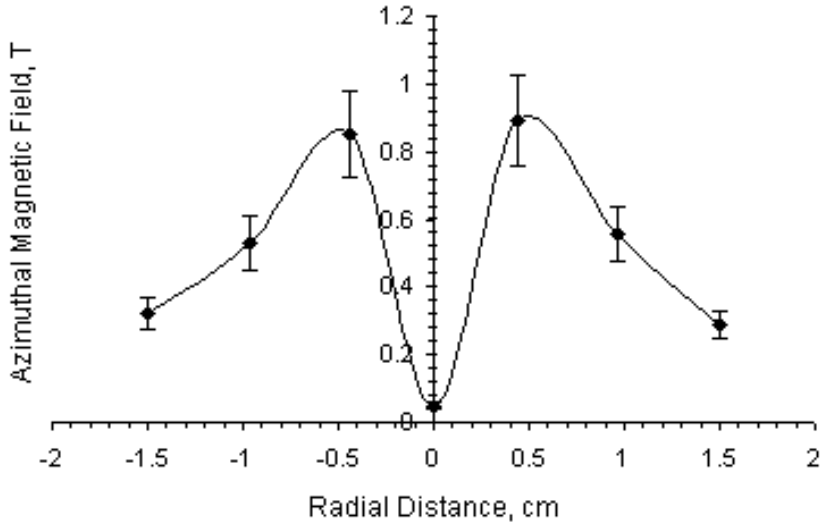

Figure 5.41: Radial magnetic field probe profile taken at $z = 0, I = 22.6$ kA.

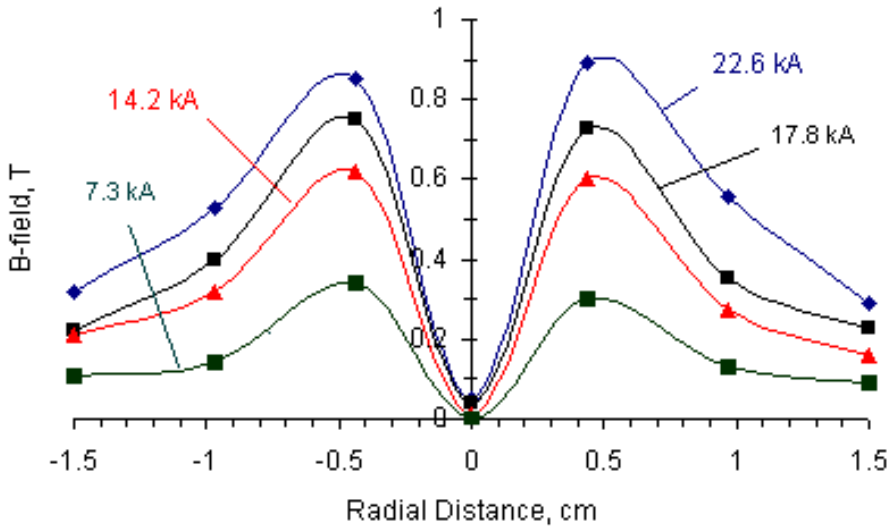

Figure 5.42: Radial magnetic field probe profile taken at $z = 0, I = 22.6$ kA.

5.10 Thruster Efficiency

In the absence of direct thrust measurements, several different methods can be used to estimate the thruster efficiency, which is defined as the ratio of jet kinetic power to input power

$$\eta = \frac{\dot{m}u_e^2}{2P_{in}} \tag{5.22}$$

The dynamic impedance is found through the relation ($I^2 Z_{dyn} = Tu_e$) and can be written as

$$Z_{dyn} = \frac{1}{4}L'u_e \tag{5.23}$$

Rewriting the exhaust velocity in terms of the known L' and measured mass bit m

$$u_e = \frac{1}{2}\frac{L'\psi}{m} \tag{5.24}$$

The thruster efficiency thus takes the form

$$\eta = \frac{Z_{dyn}}{Z_{arc}} = \frac{(L')^2\psi}{8mZ_{arc}} \tag{5.25}$$

Tests were initially conducted on a thruster possessing a radius ratio of 2.6, which yielded a computed efficiency of 21%. Increasing the diameter of the annular electrode resulted in an increase in the efficiency to 25%. Assuming the electrical characteristics and mass bit are roughly constant for a given discharge energy, the efficiency rises to 30% at a radius ratio of 5 (Fig. 5.43) with an exhaust velocity of 23 km/s.

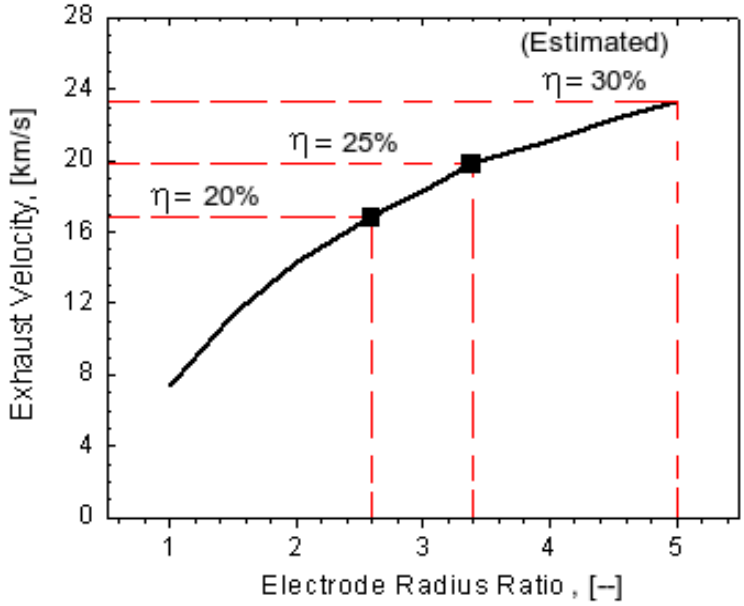

Figure 5.43: Exhaust velocity and thruster efficiency as a function of electrode radius ratio.

5.11 Uncertainty Analysis: Error Propagation

To estimate the experimental error in the triple probe measurements, we recall the equations used to calculate T_e, n_e, and the space potential ϕ_p

$$-I_1 = -A_p J_e \exp(\chi_1) + A_p J_i(\chi_1) \tag{5.26}$$

$$I_2 = -A_p J_e \exp(\chi_2) + A_p J_i(\chi_2) \tag{5.27}$$

$$I_3 = -A_p J_e \exp(\chi_3) + A_p J_i(\chi_3) \tag{5.28}$$

where

$$\chi \equiv \frac{e(\phi - \phi_p)}{kT_e} \tag{5.29}$$

The total uncertainty can be calculated from [59, 60]

$$U_i = \sqrt{B^2 + (t_{\nu,95}P)^2} \tag{5.30}$$

where B is the bias limit, P is the precision (repeatability) error, and $t_{\nu,95}$ is the t distribution. The degrees of freedom in the result is given by

$$\nu_T = \sum_{n=0}^{\infty} [\theta_i(P)_{X_i}] \tag{5.31}$$

where θ_i is defined as the sensitivity coefficient

$$\theta_i = \frac{\partial r}{\partial X_i} \tag{5.32}$$

Due to the non-linear and implicit nature of equations 5.26, the sensitivity coefficients are estimated using a finite difference method

$$\frac{\partial r}{\partial X_1} = \frac{\Delta r}{\Delta X_1} = \frac{r_{X_1+\Delta X_1, X_2, \ldots X_J} - r_{X_1, X_2, \ldots X_J}}{\Delta X_1} \tag{5.33}$$

The bias error includes the individual instrument errors. The instrument error for the Pearson probe is $\pm 1\%$ and $\pm 0.1\%$ for the Tektronix TDS 3034B oscilloscope. The diameter

and length of the probes were measured with a digital caliper with a resolution of 0.01 mm. Under most operating conditions, the applied floating voltages (ϕ_{12} and ϕ_{13}) are constant during the current pulse and within 0.4 V of the manufacturers specifications.

Ten measurements ($N_p = 10$) were taken at each location, thus the degrees of freedom in each measurement is $\nu = N_p - 1 = 9$. The precision error due to temporal variation is given by

$$P = \frac{S_T}{N_p^{1/2}} \tag{5.34}$$

where S_T is the standard deviation

$$S_T = \left[\frac{1}{N-1} \sum_{i=1}^{N} (X_i - \bar{X})^2 \right]^{1/2} \tag{5.35}$$

Additional sources of error have been discussed by Tilley et. al. [40], who examined the performance and applicability of the triple probe to MPD thruster plumes. For a finite cylinder in a two temperature Maxwellian plasma, the ion current has the functional form

$$J_i(\chi) = \Sigma_i J_{io} \vartheta \left(\chi, S_{\perp i}, \frac{r_p}{\lambda_D}, \frac{T_i}{Z_i T_e}, \frac{\lambda_{ii}}{r_p}, \tau, \frac{s}{\lambda_D}, \frac{R_L}{r_p} \right) \tag{5.36}$$

where ϑ is on the order of unity and is a correction factor to the random ion current J_{io}. The signals were found to be highly repeatable and noise-free so the precision error was low. The main source of error is thus the unknown atomic state, probe area, and probe alignment for the radial electron density measurements.

Chapter 6

Cathode Sheath Model

6.1 Introduction

In this section, the experimental discharge current, mass bit, and triple probe data are used to predict the cathode surface properties through use of Poisson's equation and an power density balance. Particular attention is paid to vacuum arc research using non-refractory metals, such as mercury and copper. The chapter begins with a review of MPD cathode erosion studies.

6.2 MPD Electrode Erosion

Electrode erosion is the primary lifetime issue for MPD thrusters and a great deal of research has been devoted to understanding its underlying mechanisms. Experiments have shown that appreciable electrode erosion is present under all operating conditions, indicating that it is inherent to MPD thruster operation. The erosion rate has been measured by weighing of the electrodes [51], use of quartz crystal microbalances [61], and surface layer activation using radioactive materials [62]. The three measurement methods generally show good agreement with each other, with erosion rates in the range of 4 -18 μg/C.

Schrade et. al [63] performed experiments on a steady-state MPD thruster with a thoriated tungsten cathode. It was found that different modes of erosion were present. During the start-up phase, highly unstationary spots were present on the cathode surface yielding high current densities (10^{12} A-m^{-2}) and relatively high erosion rates (E_r = 16.7 μg/C). During

the steady portion of the pulse, a diffuse current pattern formed (10^7 A-m^{-2}) and the erosion rate dropped by an order of magnitude ($E_r = 0.3$ μg/C).

6.3 Non-Refractory Electrodes

All of the work on MPD cathode erosion has been done on refractory metal electrodes. The major distinction between refractory metals and non-refractory metals, such as gallium, lies in the ability to support thermionic emission without strong melting or vaporization. A measure of this ability can be expressed by calculating the ratio of evaporation to thermionic emission for different metals [64]

$$\varphi = \frac{e\Gamma}{j_{tf}} = \frac{e\frac{P_v}{\sqrt{2\pi m_i k T_s}}}{AT_s \exp(-e\phi_w/kT_s)} \tag{6.1}$$

The vaporization is calculated using the Langmuir equation (discussed in detail below), and the thermionic emission is calculated using the Richardson equation. A plot of Eqn. 6.1 is plotted up to the boiling point of several different electrode materials and shown in Fig. 6.1. On the basis of this plot, one would expect the erosion rates of the lower melting point metals to be higher than those of the refractory metals. Table 6.3 shows the erosion rates for a wide range of metals utilized in vacuum arcs [35, 65]. The erosion rate is calculated by dividing the mass loss by the time integral of the current pulse. It has been found that the measured erosion rate depends on the particular operating conditions (arc current, pulse length, geometry, etc.), however, refractory metals generally exhibit lower erosion rates.

Table 6.1: Measured erosion rates for pure metals.

	Hg	**Ga**	Cu	Al	Fe	W	Zr
Er [mg/C]	600	**198**	130	120	73	55	53

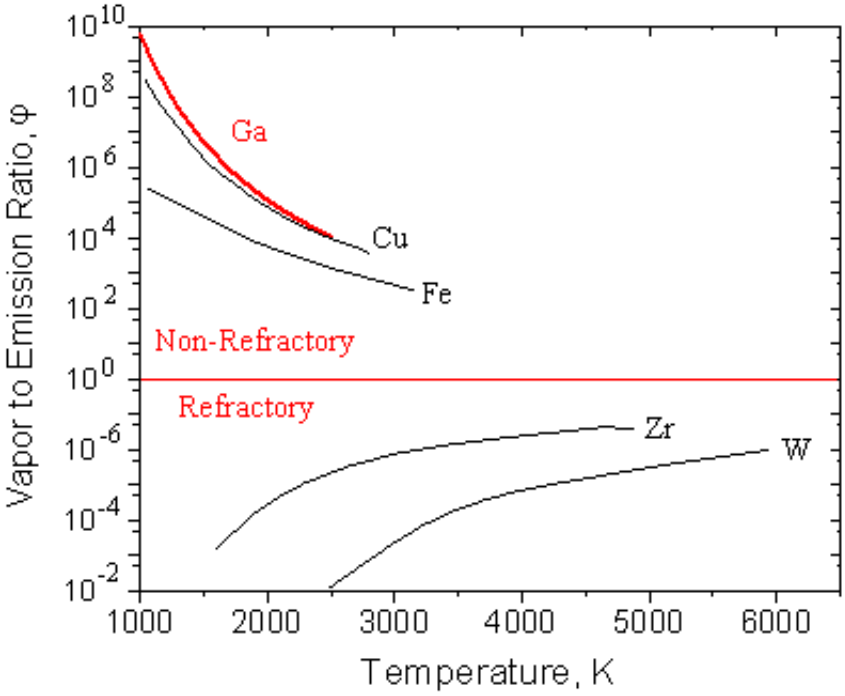

Figure 6.1: Comparison of vaporization to emission ratios for pure metals.

6.4 Cathode Spots

There is no data on the behavior of gallium in vacuum arc literature. It is therefore instructive to look at past vacuum arc data to estimate reasonable ranges for spot phenomena on gallium cathodes. The cathode spot in vacuum has two basic functions. It provides for the discharge medium by emission of matter into the gap, and for current continuity at the cathode by emission of matter into the gap. For non-refractory metals, beyond a certain temperature the global evaporation of the cathode is sufficient for maintaining the discharge medium. When both evaporation and thermionic emission satisfy the requirements of the discharge, a spotless arc that operates in a steady state has been observed [66].

Table 6.4, compiled by Harris [67], summarizes cathode spot currents for a wide range of materials. The spot current generally increases with the boiling point of the cathode, while Djakov and Holmes [68] have suggested that the thermal conductivity may also plays a role. Spot currents between 60 - 100 A have been observed with Ag electrodes, which appears to be a reasonable regime for gallium which has a boiling point of 2477 K.

Table 6.2: Average cathode spot current for various metals in vacuum arcs.

Cathode Material	Boiling Point [K]	Spot Current [A]
Mercury	630	0.4-0.7
Cadmium	1040	8-15
Zinc	1180	9-20
Bismuth	1833	3-5
Lead	2013	5-9
Indium	2273	15-18
Silver	2485	60-100
Aluminum	2740	30-50
Copper	2840	75-100
Chromium	2945	30-50
Iron	3134	60-100
Titanium	3560	70
Carbon	4098	200
Molybdenum	4885	150
Tungsten	5933	250-300

Post-mortem craters were observed experimentally through use of a scanning electron microscope (SEM). Three micro-photographs are shown in Figs. 6.2 - 6.4. The gallium cathode is characterized by microscopic fractures and protrusions prior to firing, as shown in Fig. 6.2. After a single shot, a fraction of the surface remains in the liquid state as shown in Fig. 6.3 . It also appears that the surface forms point peaks; these have been referred to as Taylor cones [69]. After several shots, 25 - 100 μm diameter craters are found on the gallium surface; these craters are accompanied by macroparticle ejection.

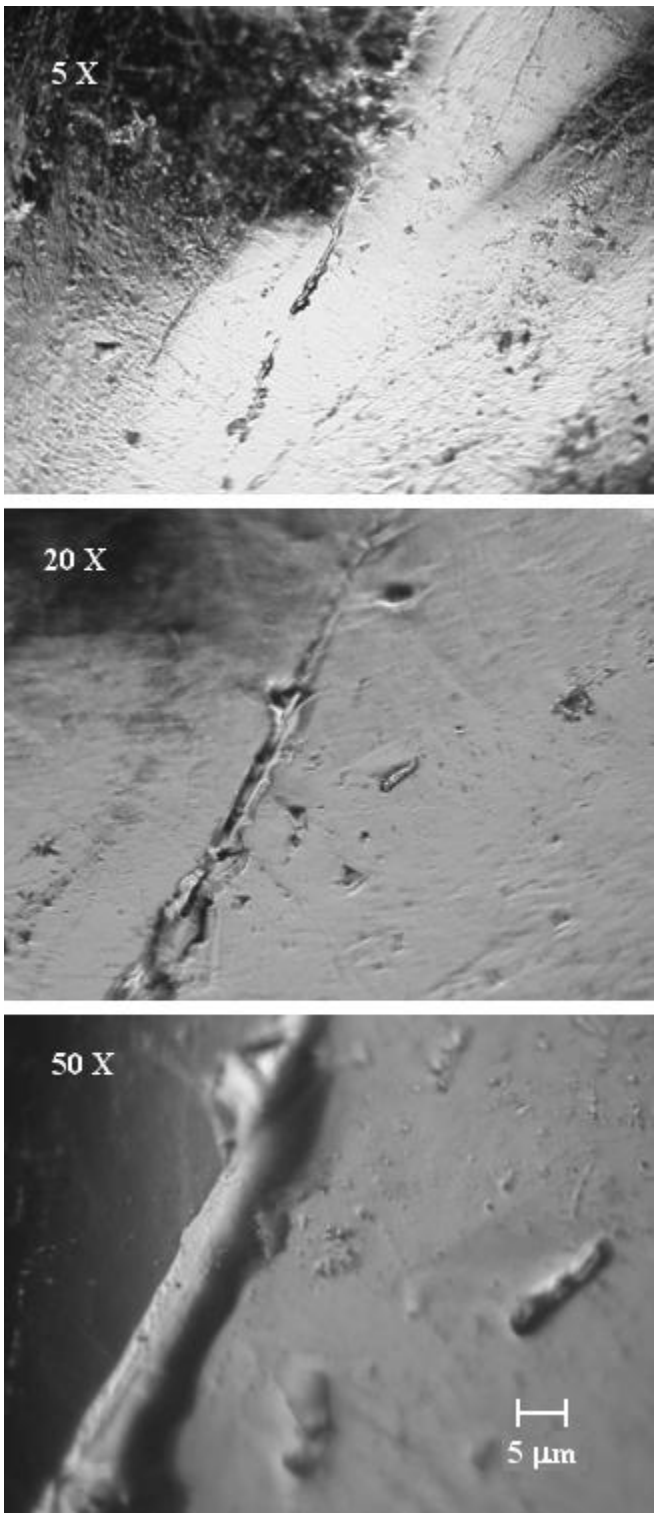

Figure 6.2: Microphotographs of gallium surface prior to tests.

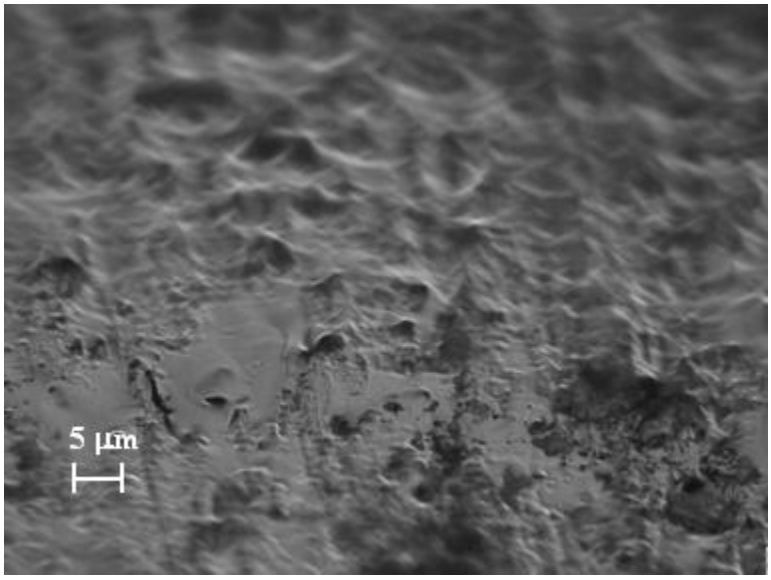

Figure 6.3: Taylor cones appear to form on the gallium surface due to the high electric field.

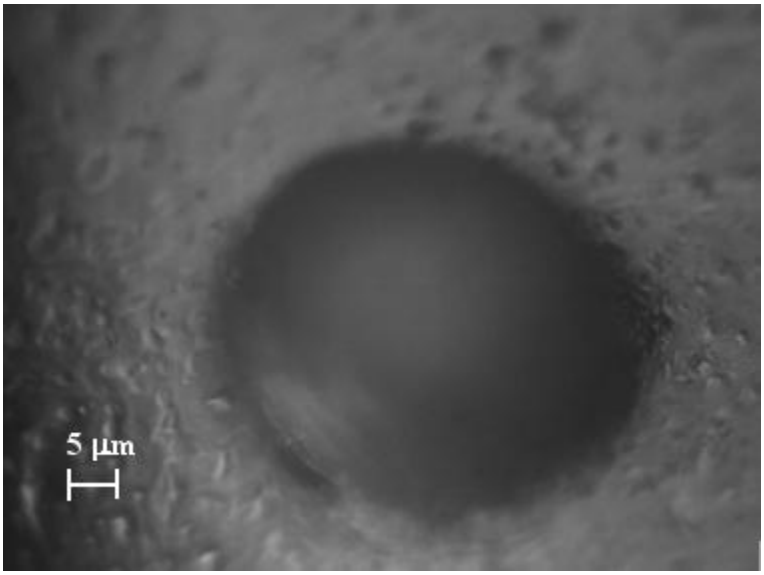

Figure 6.4: Post mortem crater left at a discharge current level of 22 kA utilizing a central anode.

6.4.1 Physical Model

In this section a cathode sheath model is coupled to the experimentally found mass flow rate to yield cathode surface properties. Similar calculations have been used to successfully

model vacuum arcs [35, 70], high-pressure arc systems [71] and steady-state arcjet thrusters [72, 73], as well as MPD thrusters utilizing a refractory cathode [74].

The physical model used by Coulombe and Meunier [71] is adopted in the current study (Fig. 6.5). The first zone is the cathode itself, which exists in a condensed state. At the cathode surface, electron emission, evaporation, and heat conduction are the dominant processes. Above the cathode surface is a collisionless cathode sheath region (a few Debye length thicknesses) which exhibits strong gradients in particle density and voltage. The strong electric field within the sheath accelerates electrons away from the cathode, and is also transversed by a flow of ions and electrons from the plasma. The ions are accelerated in the sheath region and provide the dominant source of cathode heating. The electrons undergo ionizing collisions with the neutral particles in the ionization region which results in a highly ionized plasma.

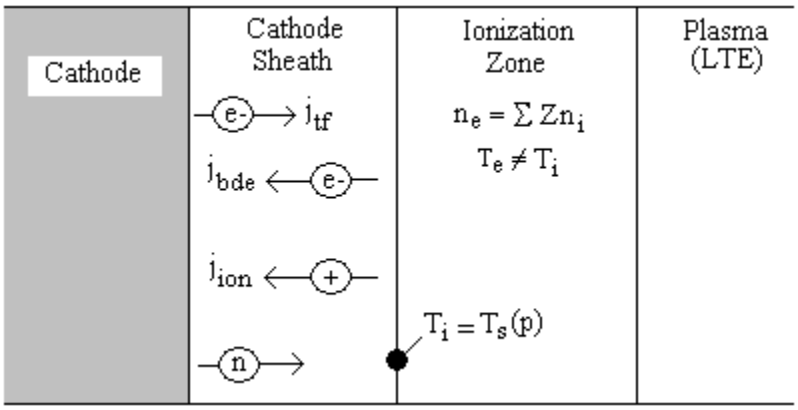

Figure 6.5: Cathode sheath and adjacent plasma used in cathode spot model.

The current densities shown in Fig. 6.5 represent the ion current density j_{ion}, the thermofield current density j_{th}, and the back diffusing electron density j_{bde}. It is assumed that at the sheath boundary the heavy particle temperature is equal to the surface temperature. The total current density at the cathode spot is the sum of the ion and electron currents

$$j_{tot} = j_{ion} + j_e = j_{ion} + j_{tf} - j_{bde} \tag{6.2}$$

The ion current density is calculated utilizing Bohm's criteria for sheath formation [75]

$$j_{ion} = \sum_i Z_i e n_i c_B \tag{6.3}$$

where c_B is a modified version of Bohm's sheath velocity [75], taking into account the flux of emitted thermofield electrons [76]

$$c_B = \left(\frac{kT_e}{m_i}\right)^{1/2} \left(\frac{1+\eta_s j_b}{1-j_b}\right)^{1/2} \tag{6.4}$$

where the non-dimensional parameters η_S and j_b are given by

$$\eta_s = eV_s/kT_e \tag{6.5}$$

$$j_b = j_{tf}/j_c \tag{6.6}$$

$$j_c = n_e e \left(\frac{kT_e}{me}\right)^{1/2} (2\eta_s)^{3/2} \tag{6.7}$$

The thermofield emission is due to the high electric field and temperature at the cathode surface

$$j_{tf} = e \int_{-\infty}^{\infty} N(T_s, \epsilon) D(E, \epsilon)\ \mathrm{d}\epsilon \tag{6.8}$$

where expressions for the electron supply function $N(T_s, \epsilon)$ and electron tunneling probability $D(E, \epsilon)$ are given in Ref. [77], and are discussed further in Appendix C. The thermofield current density for different surface temperatures is shown in Fig. 6.6.

The back-diffusing electron current density arises from the fraction of plasma electrons able to overcome the sheath potential

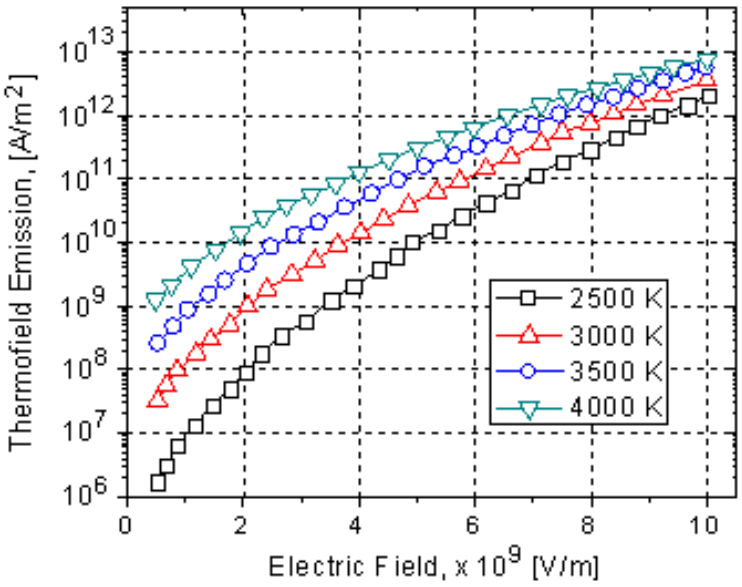

Figure 6.6: Thermofield emission as a function of surface electric field.

$$j_{bde} = \frac{1}{4} e n_e \sqrt{\frac{8kT_e}{\pi m_e}} \exp\left(\frac{-eV_s}{kT_e}\right) \tag{6.9}$$

The neutral particle flux Γ at the cathode surface is calculated by using the Langmuir vaporization equation [36]

$$\Gamma_n^{out} = \frac{p_v}{\sqrt{2\pi m_i k T_s}} \tag{6.10}$$

The surface temperature T_s and vapor pressure p_v are related through the Clausius-Clapeyron relation (in SI units)

$$\log p_v = 5.006 + A - \frac{B}{T_s} \tag{6.11}$$

where $A = 5.52$ and $B = 13798$ for gallium. Equation (6.10) is derived under the assumption of equilibrium (equal condensation and vaporization rates), however Langmuir argued that since the atomic emission process is not likely to be influenced by gas conditions in vacuum but rather only the surface temperature, Γ represents the gross atomic flux whether the system is in equilibrium or not. At higher pressures, atomic collisions near the surface

can lead to a flux of atoms returning to the surface (Fig. 6.7), lowering the evaporated flux calculated using equation 6.10. Knudsen [78] first addressed this non-equilibrium problem when studying the evaporation of Hg into vacuum. Later authors [79] expanded Knudsen's analysis and considered two regions near the cathode surface: 1) a non-equilibrium region with rare collisions (atom relaxation zone) and 2) a collision dominated region with hydrodynamic flow. These regions are illustrated in Fig. 6.7.

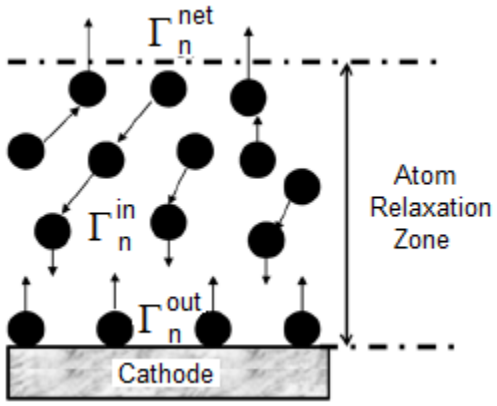

Figure 6.7: Schematic showing back-flow of neutral particles due to the high pressure build-up adjacent to the cathode surface.

The temperature, density, and velocity within the atom relaxation zone are found through integration of the Boltzmann equation

$$\frac{\partial f}{\partial t} + \mathbf{v}\frac{\partial f}{\partial r} = \left(\frac{\mathrm{d}f}{\mathrm{d}t}\right)_{coll} \tag{6.12}$$

where $\mathbf{r}$ is a spatial coordinate, $\mathbf{v}$ is the velocity vector, and f is the distribution function. Several authors have solved Eqn. (6.12) using various hydrodynamic and kinetic treatments, resulting in formulations similar to the Langmuir expression, but with a RHS coefficient ranging from 0.80-0.85 (i.e. 15-20% of the evaporated atoms return and condense on the surface). The aforementioned analyses assumes the neutral flux is expanding into a vacuum; for the present case the cathode surface is vaporizing into a high-pressure arc column. The stream of charged particles from the adjacent plasma leads to a highly ionized plasma close

to the cathode surface. The returning neutral particle flux can also be written in terms of the degree of ionization α

$$\Gamma_n^{in} = \frac{j_{ion}(1-\alpha)v}{4Ze\alpha c_B} \tag{6.13}$$

where v is the electron thermal velocity. Saha ionization calculations indicate a high degree of ionization near the sheath edge, so the returning neutral particle flux is deemed to be negligible compared to the incoming flux of charged particles, and the Langmuir equation is used to calculate the evaporated flux of gallium atoms from the cathode.

Poisson's equation governs the behavior inside the sheath. Mackeown [80] developed an expression for the charge distribution within the sheath, which was later extended by Prewett and Allen [76] to include back diffusing electrons. Following the analytical approach used in [71], Poisson's equation can be expressed as

$$\frac{\mathrm{d}^2V}{\mathrm{d}z^2} = -\frac{e}{\epsilon_o}\left(\sum_i Z_i n_i - n_{FT} - n_{bde}\right) \tag{6.14}$$

The thermofield electrons are emitted with an energy of $2kT_s$ and are accelerated within the sheath to a velocity of

$$v_{tf}(V) = \left(\frac{2e}{m_e}\left(\frac{2kT_s}{e} + V\right)\right)^{1/2} \tag{6.15}$$

The thermofield electron density as a function of the potential is thus given by

$$n_{tf}(V) = \frac{j_{tf}}{ev_{tf}(V)} \tag{6.16}$$

where the thermofield emission is calculated using Eqn. 6.8. The ion particle number density throughout the sheath can be through use of the continuity equation

$$n_i(V)v_{ion}(V) = (n_i v_{ion})_{\text{sheath edge}} \tag{6.17}$$

where the ion velocity within the sheath is given by

$$v_{ion} = \left(\frac{2e}{m_i} \left(\frac{m_i c_B^2}{2e} + Z_i(V_s - V) \right) \right)^{1/2} \tag{6.18}$$

The back-diffusing electron density is found assuming a Boltzmann distribution throughout the sheath

$$n_{bde} = n_e \exp\left(\frac{e(V - V_c)}{kT_e} \right) \tag{6.19}$$

Equation 6.14 can be integrated once to yield an analytic expression for the electric field, and the potential within the sheath can be found by utilizing the boundary conditions

$$\text{at z =0} \qquad \text{V(0) =0} \qquad \frac{\mathrm{d}V}{\mathrm{d}z} = E(0) \tag{6.20}$$

A power balance at the cathode surface can be expressed as

$$P_{ion} + P_{bde} = P_{vap} + P_{bde} + P_{cond} \tag{6.21}$$

where the terms on the left hand side represent heating terms, and the terms on the right hand side are cooling mechanisms. The heating due to ion bombardment is expressed as

$$P_{ion} = \sum_i j_i \left(\phi_s + \phi_i - \phi_{eff} + \frac{5kT_i}{2Ze} \right) \tag{6.22}$$

The terms on the RHS correspond to the kinetic energy gained in the cathode fall potential ϕ_s, the recombination energy based on the ionization potential ϕ_i diminished by the effective work function ϕ_{eff}, and impacting thermal ion energy. Similarly, the plasma electrons condensing on the cathode heat the surface

$$P_{bde} = j_{bde} \left(\phi_{eff} + \frac{5kT_e}{2e} \right) \tag{6.23}$$

The thermofield electrons leaving the cathode surface cool the surface

$$P_{tf} = j_{tf}(\varepsilon_{not}) \tag{6.24}$$

The expression for the Nottingham cooling potential is given in Appendix C. The power dissipated by material evaporation is given by

$$P_{vap} = \Gamma(h_{vap} + 2kT_s) \tag{6.25}$$

where h_{vap} is the enthalpy of vaporization. The radiative power, assuming a emissivity of 1 is given by

$$P_{rad} = \sigma T_s^4 \tag{6.26}$$

The equation of state is given by

$$p = \sum_i n_i k T_i + n_e k T_e \tag{6.27}$$

The Saha equation is used to resolve the particle number densities at the sheath edge

$$\frac{n_e n_i^{Z+1}}{n_i^Z} = 2\left(\frac{2\pi m_e k T_e}{h^2}\right)^{3/2}\left[\frac{Q_i^{Z+1}(T_e)}{Q_i^Z(T_e)}\right]\exp\left(-\frac{\epsilon_i}{kT_e}\right) \tag{6.28}$$

The power balance and Poisson's equation can be used to find the surface temperature and electric field, and resolve the particle densities within the sheath. The results are presented in the next section.

6.5 Model Results

Figures (6.8) - (6.10) show the spot temperature, electric field, pressure, and electron current fraction as a function of the spot current density for a discharge current level of 22.6 kA. The lower limit of 3.8×10^8 A/m^2 corresponds to a diffuse current mode; that is, an emission area that covers the entire cathode. An increase in the ion bombardment lead to an increase in the spot current density, which leads to an increase in both the spot temperature and pressure. The increased charged particle densities lead to stronger electric fields and thermofield emission. For the diffuse case, the ions carry the bulk of the current, while the electrons carry 85% of the current at a spot current density of 10^{10} A/m^2. The experimentally found mass flow rate (6 g/s) can be used to close the system of equations. The net mass flow rate is assumed to be the evaporated neutral flux minus the flux of ions that return and condense on the cathode surface

$$\dot{m}_{net} = \dot{m}_{out} - \dot{m}_{out} = \left(\Gamma - \sum_i \frac{j_i}{Z_i e} \right) m_i (I/j_{tot}) \tag{6.29}$$

This yields a current density of 5.0 $\times 10^9$ A/m^2, and is denoted by the dashed red line in each figure.

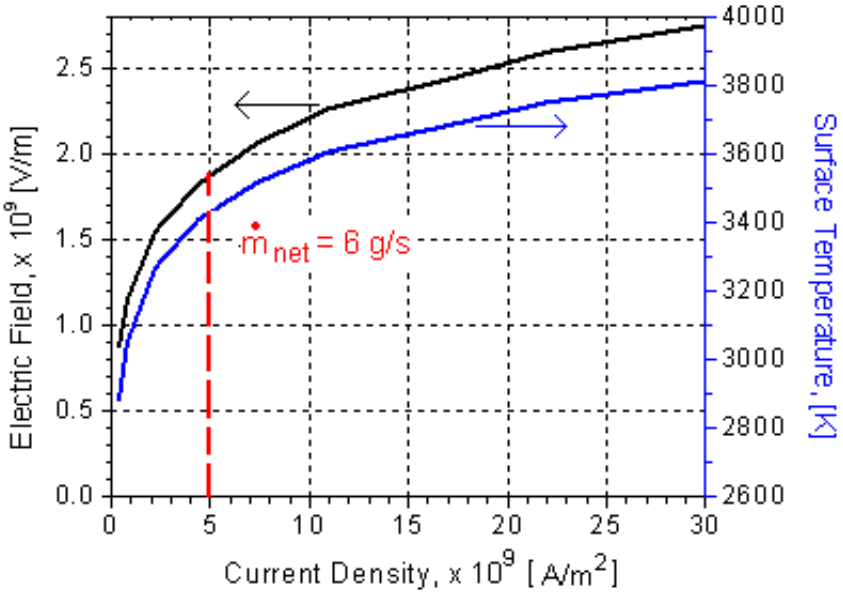

Figure 6.8: Spot temperature and electric field as a function of the spot current density.

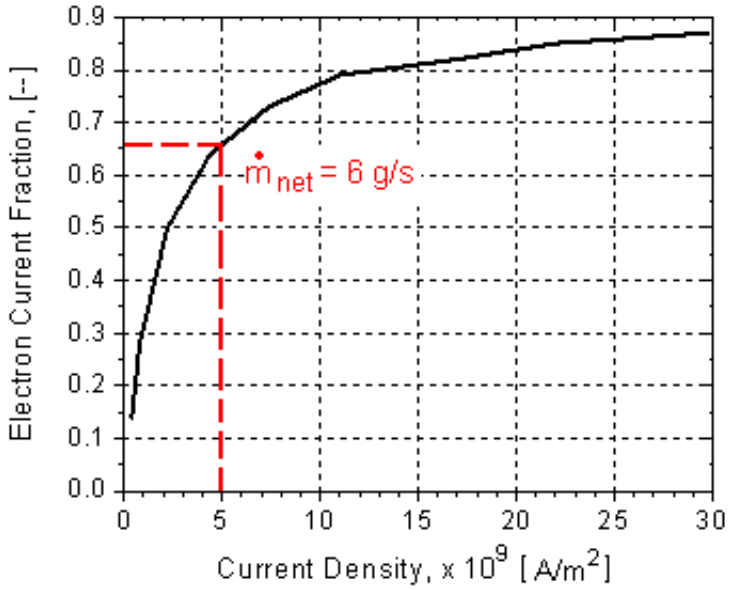

Figure 6.9: Electron current fraction as a function of the spot current density.

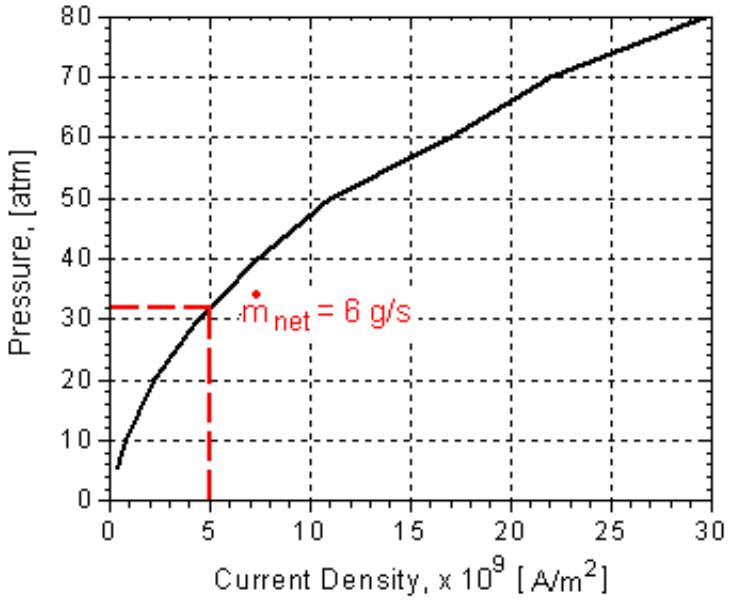

Figure 6.10: Pressure as a function of the the spot current density.

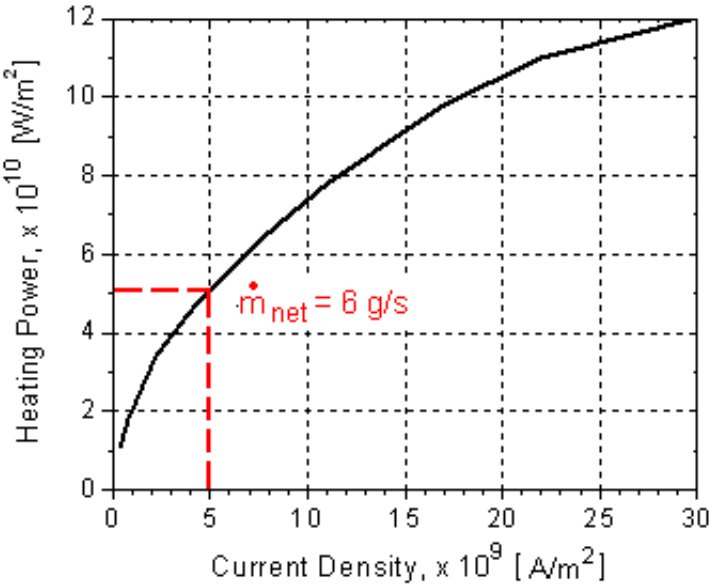

Figure 6.11: Input heating power due to ion and electron bombardment as a function of spot current density.

The results of the power balance are shown in Figs. (6.11) and (6.12). The surface heating is due primarily to ion bombardment as less than 1% of the plasma electrons are able to overcome the sheath potential. At lower current densities, heat conduction within the gallium cathode provides the dominant source of surface cooling, and decreases monotonically with current density. As the thermofield emission increases, it provides 60% of the cooling at a current density of 5×10^9 A/m^2.

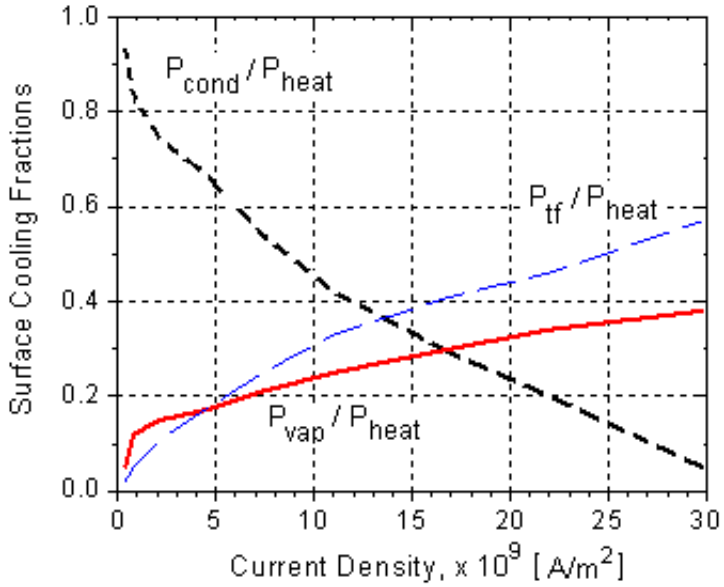

Figure 6.12: Conduction, vaporization, and thermofield cooling fractions as a function of spot current density.

The model predicts a sheath of a few Debye lengths as shown in Fig. 6.13. The sheath space charge is shown in Fig. 6.14. The space charge results from the electron density decaying at a much more frequent rate than the ion density as the distance towards the sheath edge increases, and reaches a peak value at roughly 1.7× the Debye length. .

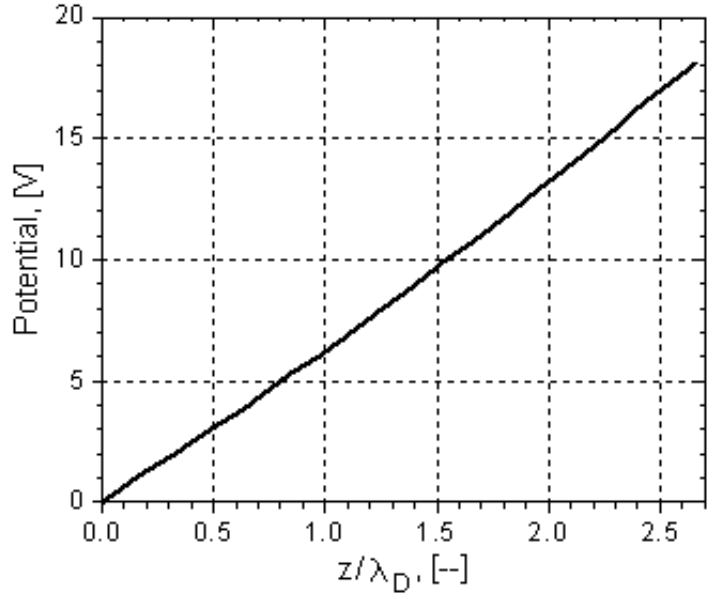

Figure 6.13: The sheath potential for a spot current density of 5×10^9 A/m2.

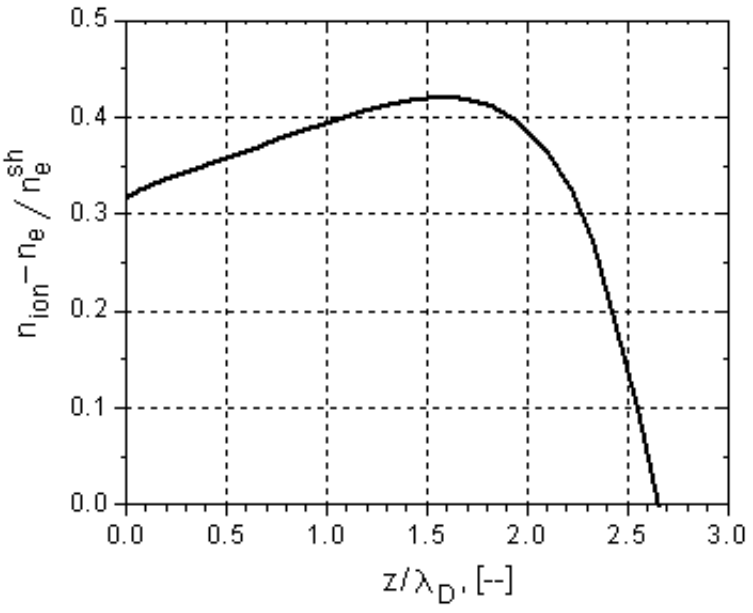

Figure 6.14: Space charge for a spot current density of 5×10^9 A/m2.

Chapter 7

Conclusions

7.1 Introduction

The experimental findings can be summarized as follows:

- A wide array of plasma diagnostics were successfully employed in the plume region of a high-current (6 -54 kA) gallium electromagnetic thruster. At these high currents and short pulse lengths, fast valves are not practical, and a method of mass injection such as evaporation presents itself as a viable alternative.

- A compact, 6 mΩ pulse forming network was designed and built to power the thruster. The impedance of the PFN is matched to the thruster arc impedance, resulting in a high energy transfer efficiency.

- MPD thrusters require short pulses in order to reduce PFN mass, while gas-fed MPDs cannot reliably achieve switching for valved pulses less than 1000 μs. The present experiment successfully injects propellant through cathode ablation for a PFN pulse length of 50 μs.

- Arc impedances in the range of 6-7 mΩ were measured from the discharge current and arc voltage. These low values compare favorably with prior electromagnetic thrusters and are required for high efficiency. Reversing the electrode polarity was observed to have little effect on the pulse current and voltage traces.

- Experiments were conducted at discharge currents in the range of 19-54 kA utilizing a

central gallium anode. The lack of high-frequency oscillations in the arc voltage trace implies a sufficient number of charge carriers were present in the discharge. Persistent macroparticle ejection led to the rejection of central anode operation.

- The measured mass bit follows a quadratic dependence on the discharge current. This yields a calculated exhaust velocity of 17 km/s and 20 km/s for radius ratios of 2.6 and 3.4. The exhaust velocity was experimentally measured using electrostatic probe techniques, which yielded on axis velocities in the range of 15 - 22 km/s. The velocity is found to be invariant with the discharge current.

- The mass bit varies quadratically with the discharge current. When using a central gallium anode, macroparticles were ejected at all energy levels tested. Macroparticle ejection was eliminated when using a central cathode with a diameter of 8.7 mm (3.4 electrode radius ratio).

- Emission spectroscopy was used to determine the species present in the discharge as a function of the discharge current. Ga I-III lines were present at all energy levels. The number of doubly ionized gallium and iron (from the outer electrode) lines increased as the current increased. It is suspected that Ga IV is present in the discharge, however no Ga IV data exists above 150 nm.

- Spatially resolved magnetic field probe data reveals a symmetric arc discharge with no evidence of the current spoking instability.

- The mass bit and arc impedance data yield a thruster efficiency of 25%, with ionization being the major loss mechanism. The velocity is invariant with the discharge current, so increasing the power level will not lead to performance gains. However, geometric optimization may lead to higher efficiencies.

- Utilizing experimental data, a sheath and a power balance model predicts: a cathode emission area of 5×10^9 A/m^2, which is in general accordance with vacuum arc data.

At this current density: the cathode temperature is 3400 K, the electric field is 1.8×10^9 V/m, and the electrons carry 65% of the current near the cathode surface.

7.2 Future Work Suggestions

The experiments have shown that electrode polarity and geometry plays a strong role in the current distribution and resulting mass ablation. A more detailed analysis of the anode and cathode regions, perhaps using embedded thermocouple and high-speed photography would permit more detailed numerical analysis of the cathode region. A geometric optimization is necessary for controlling the amount of gallium ablated per pulse. This would allow for control the exhaust velocity, and possibly raising the efficiency of the thruster.

Appendix A

Low Energy Proof of Concept Experiments

Experiments were initially conducted using a 20 J capacitor to characterize the electrical characteristics and determine the ionic species present in the discharge. The discharge current and arc voltage are shown in Figs. A.1 and A.2. A side and back view of the arc discharge is shown in Fig. A.3.

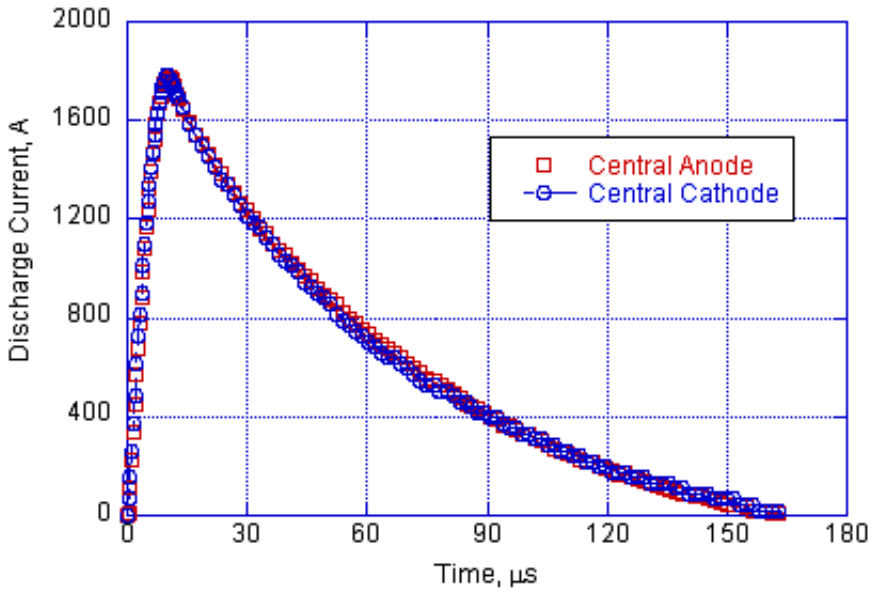

Figure A.1: Current pulse of 20 J pulser.

Two difficulties were initially encountered when operating the plasma source. The first was that the arc preferentially struck the exposed stainless steel on the inner electrode, as opposed to the gallium. This was verified both by examining the terminal voltage trace and through physical inspection of the inner electrode between firings. To remedy this, self-fusing silicone rubber tape was used as an insulator, leaving only metallic gallium exposed. Additionally, it was found that below a pressure of roughly 1 Torr, a discharge would not

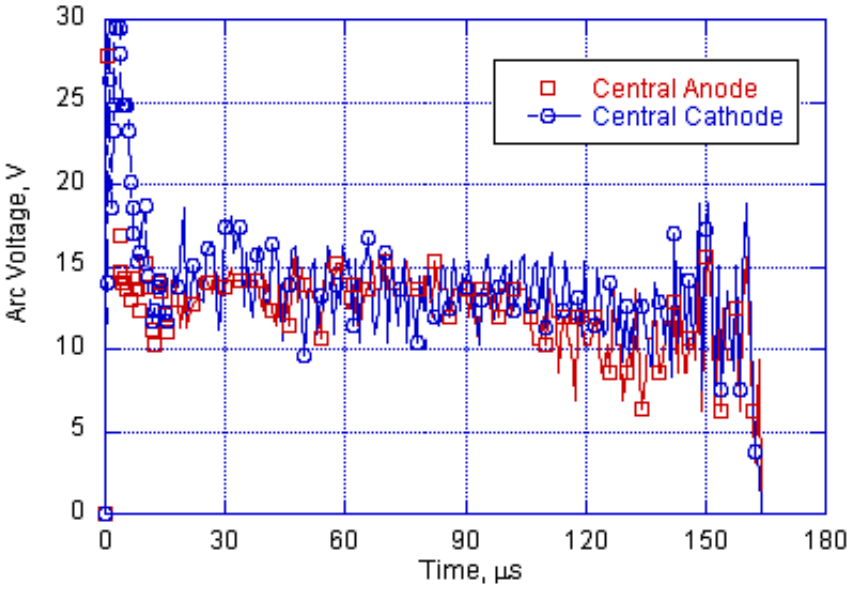

Figure A.2: Arc voltage traces taken with both a central anode and cathode.

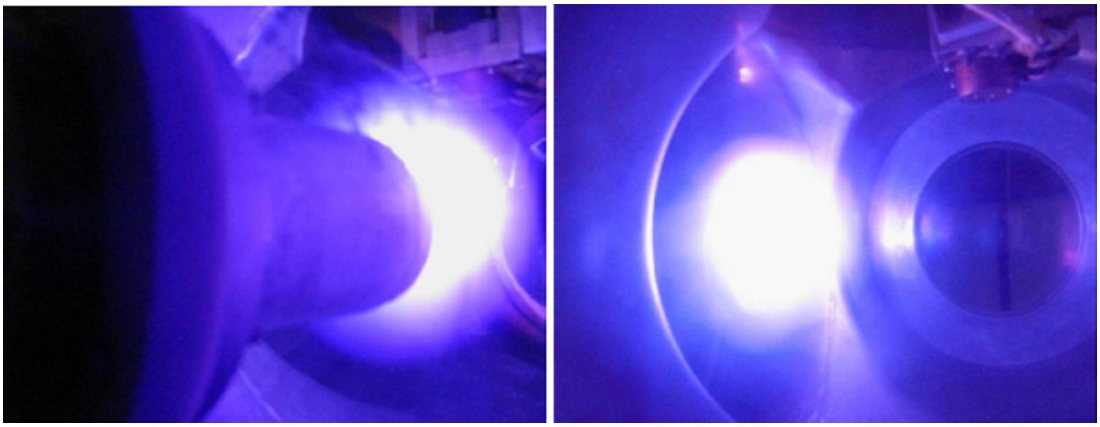

Figure A.3: Still photograph of 20 J pulser.

initiate due to the lack of initial charge carriers. This was addressed by bridging the anode and cathode with a thin layer of carbon graphite applied with a spray technique. This technique is commonly employed in vacuum arc thrusters, where the graphite serves as the initial conductive path between the anode and cathode, providing a means for Joule heating at the coating-cathode interface. Neither a trigger electrode nor a specific electrical trigger pulse generator is required; the method has therefore been dubbed trigger-less arc initiation [81]. Using this technique, the gallium plasma source can be operated at a background pressure of 5×10^{-5} Torr. The central cathode spectra is shown in Fig. A.4.

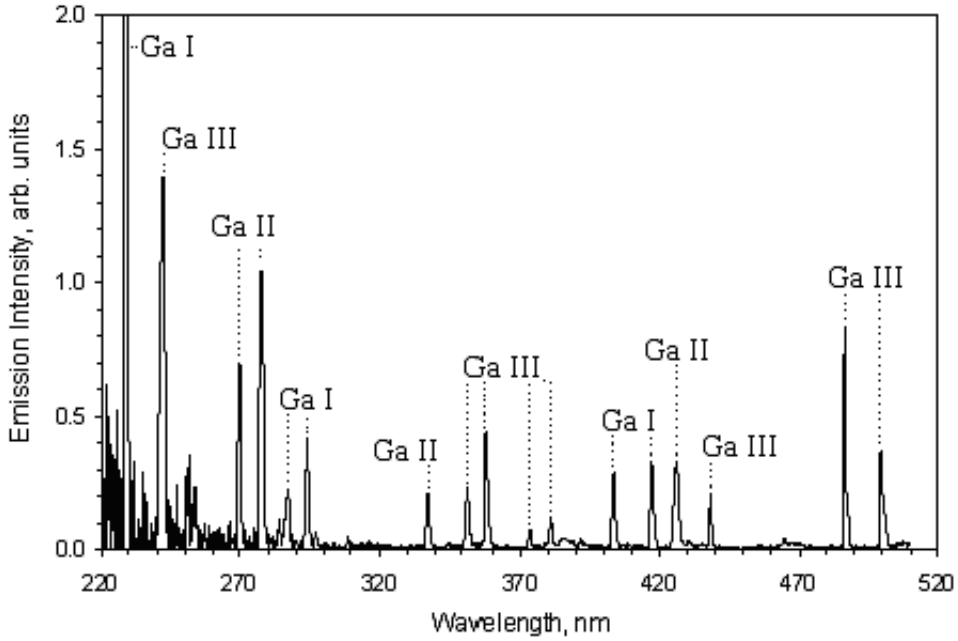

Figure A.4: 20 J cathode emission spectrum.

The emission spectrum at a background pressure of 1 Torr using a central anode is shown in Fig. A.5. A comparison with Fig. A.4 shows that the line strengths for the central anode configuration are slightly weaker, and that multiple Ga lines are absent in the 270-340 nm range. Additionally, in the central anode case, two neutral and two singly ionized Fe species lines are found in the discharge, suggesting slight erosion of the stainless steel outer electrode.

Data from experiments conducted at a background pressure of 5×10^{-5} Torr and performed using a graphite layer between the electrodes to facilitate discharge initiation are shown in Fig. 8. During these tests, the diameter of the exposed gallium was reduced from 12.7 mm to 5 mm using silicone tape. Approximately 0.2 grams of graphite bridged the two electrodes, which allowed the pulser to be fired 120 times before the graphite was expended. A comparison between Figs. 6 and 8 allows us to make some interesting observations. When the graphite layer is employed at lower background pressure, the peak intensities of the Ga lines are reduced and there are significant emissions from molecular carbon radicals above 430 nm (the so-called Swan bands [82]). This implies that energy directed into the production of gallium ions in Fig. 6 is shifted into the production of carbon ions and the excitation of

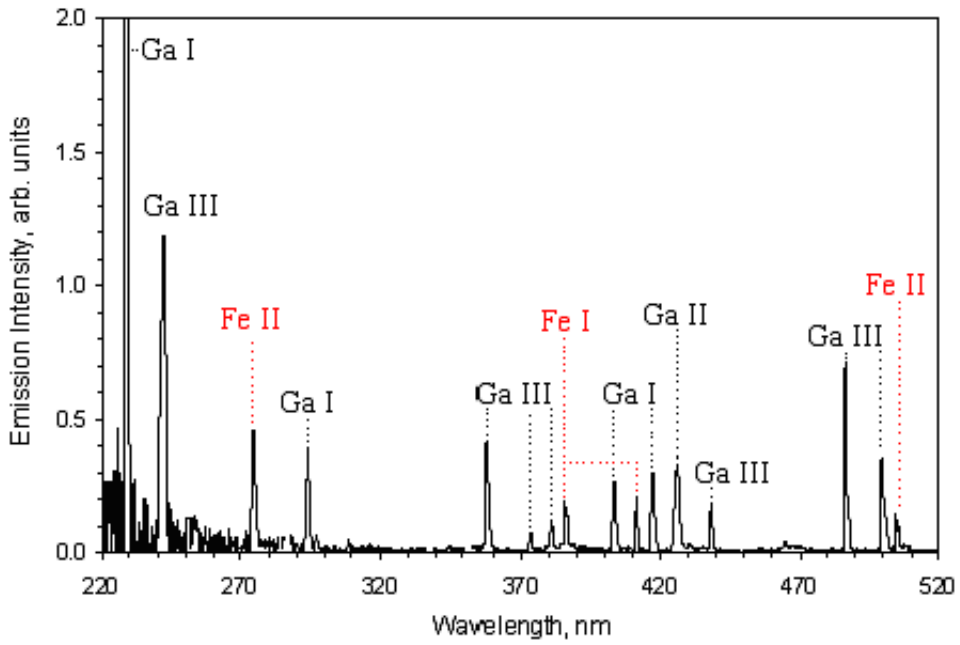

Figure A.5: 20 J anode spectrum.

molecular carbon states in the situation represented by Fig. A.6.

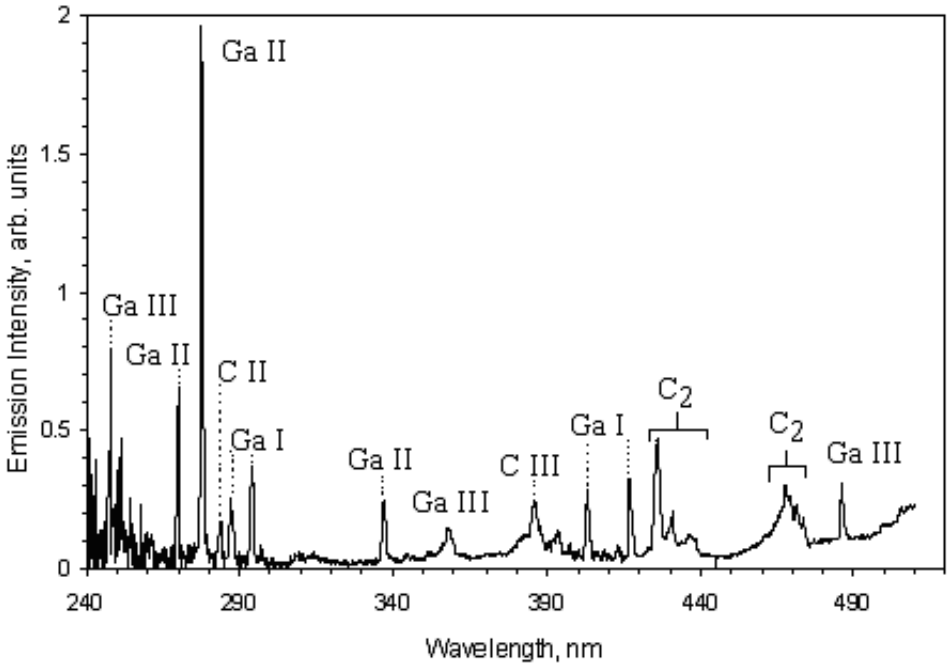

Figure A.6: Spectrum taken using a graphite bridge.

The spectroscopic data can be used to calculate an electron temperature. The concentra-

Table A.1: Neutral and ionic gallium species present in 1.8 kA arc discharge.

Specie	Wavelength [nm]	Upper Energy Level [cm^{-1}]	Lower Level	Upper Level
Ga I	229.419	43574.91	$4p^2P_{1/2}$	$6d^2F_{3/2}$
Ga I	229.786	44332.27	$4p^2P_{3/2}$	$8s^2F_{1/2}$
Ga I	287.424	34781.66	$4p^2P_{1/2}$	$4d^2F_{3/2}$
Ga I	294.364	34787.85	$4p^2P_{3/2}$	$4d^2F_{5/2}$
Ga I	294.417	34787.85	$4p^2P_{3/2}$	$4d^2F_{3/2}$
Ga I	403.298	24.788.53	$4p^2P_{1/2}$	$5s^2F_{1/2}$
Ga I	417.204	24788.53	$4p^2P_{1/2}$	5s $S_{1/2}$
Ga II	270.047	107720.56	$4p^2D_1$	p^2D_2
Ga II	277.997	135639.24	$4p^2D_1$	4f S_0
Ga II	299.265	137342.44	p^2D_2	$4f^1F_3$
Ga II	337.595	137333.33	p^2D_2	$4f^3F_3$
Ga II	425.593	137339.64	$4d^3D_3$	$4f^3F_4$
Ga III	241.787	185432.59	$4d^2D_{1/2}$	$4f^2F_{5/2}$
Ga III	373.110	187566.51	$5p^2P_{1/2}$	$6s^2S_{1/2}$
Ga III	380.660	187566.51	$5p^2P_{3/2}$	$6s^2S_{1/2}$
Ga III	499.378	160765.56	$5s^2S_{1/2}$	$5p^2P_{1/2}$

tion of each atomic and ionic species is related to the emission intensity through the relation [83]

$$I_{mr} = n_m A_{mr} h f_{mr} \tag{A.1}$$

where m and r are the upper and lower states of a transition, respectively, I_{mr} is the intensity, A_{mr} is the Einstein transition probability, h is Planck's constant, f_{mr} is the frequency, and n_m is the concentration of particles in the upper level. A quantitative spectroscopic analysis may be performed more readily under the conditions of local thermodynmaic equilibrium. Under the conditions of LTE, a single temperature describes the various energy distributions: electron velocity distribution, degree of ionization, and the distribution of the excited states [84]. The relevant temperature is that which describes the distribution function of the species domination the reaction rate, which in dense laboratory plasmas is the electron temperature

[85]. A check for the existence of LTE can be made by uising the Boltzmann relation [83]

$$\ln\left(\frac{I_{mr}}{g_m A_{mr} f_{mr}}\right) = \ln\left(\frac{n}{Q}\right) - \frac{E_m}{kT_e} \tag{A.2}$$

where k is the Boltzmann constant, E_m and g_m are the upper state energy and degeneracy, respectively, Q is the partition function, and T_e is the electron temperature. If the data points are sufficiently linear (i.e. follow LTE), the electron temperature can be found by plotting the quantity of the left hand side vs. the upper level energy. The slope of the resulting line has a slope of $1/kT_e$. Several approximations are necessary to include sets of overlapping lines. The relative emission intensity of each line is found by numerical integration of the spectral line width, and for the case of multiplets, the integrated intensity can be decomposed as the sum of two lines, e.g.:

$$I_{mr} = I_{294.417} + I_{294.424} \tag{A.3}$$

An additional relation is needed to resolve the two lines. In order to include the overlapping 294.417 nm and 294.424 nm lines, the following, the following approximation is used

$$\frac{I_{294.417}}{I_{287.424}} = \frac{(gAf)_{294.417}}{(gAf)_{287.424}} \tag{A.4}$$

The 287.424 line was used because it shares an upper state with the 294.417 line, which is necessary for Eqn. A.4 to hold. The relate the emission intensities of the other pairs of overlapping lines, it is assumed that the upper states of the two lines follow a Boltzmann distribution [84]

$$\frac{I_1}{I_2} = \frac{g_1 A_1 \lambda_2}{g_2 A_2 \lambda_1} \exp\left(-\frac{E_1 - E_2}{kT_e}\right) \tag{A.5}$$

Use of Eqn. A.5 to determine the intensity ratio necessitates an assignment of temperature, however the calculated intensities are insensitive to the choice in temperature for the range

in which we are interested (0.5-4 eV). While this relation may not rigorously hold, it does provide a reasonable first approximation. We observe that the data for each species does not fall on a straight line; therefore an assignment of an electron temperature cannot be made with confidence. It should be noted however, that this does not necessarily mean that the plasma is not in LTE. This is because the acquired spectrum represents spatially and temporally integrated emission; the averages obtained may deviate systematically from the local and instantaneous values. While the spatially and temporally averaged spectra don't allow us to definitively state the value of the electron temperature, the data and the presence of doubly ionized gallium are consistent with a value of Te in the 0.8-3 eV range.

Appendix B

Pulse Forming Network Design

B.1 Theory

In this section the design of the pulse forming network (PFN) is described. The general theory is described in Ref. [86] and is briefly reviewed here. A PFN is a series of inductors and capacitors which deliver a rectangular pulse of energy. For the purpose of circuit analysis, the capacitors can be replaced by a DC supply with a charging voltage of V_o and impedance of Z_o (Fig. B.1).

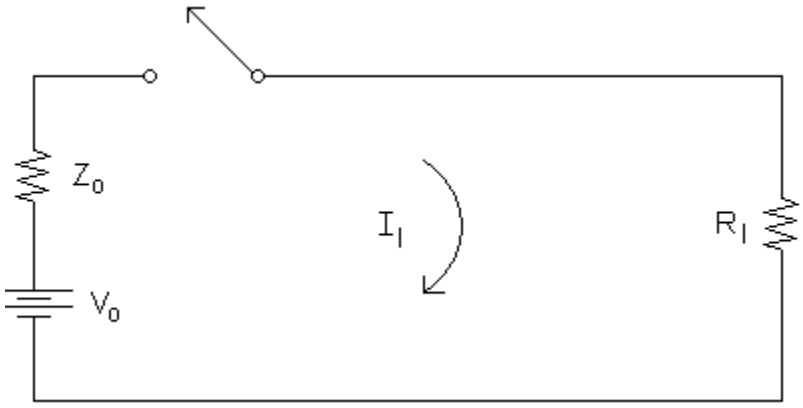

Figure B.1: Simplified equivalent circuit for PFN with a resistive load.

The current across the load is thus given by

$$I_l = \frac{V_o}{R_l + Z_o} \tag{B.1}$$

while the power and energy across the load is given by

$$P_l = \frac{V_o^2}{(R_l + Z_o)^2} R_l \tag{B.2}$$

$$W_l = P_l \tau = \frac{V_o^2}{(R_l + Z_o)^2} R_l \tau \tag{B.3}$$

The load resistance which yields the maximum power transfer if found through differentiation of Eqn. B.2

$$\frac{\mathrm{d}P_l}{\mathrm{d}R_l} = \frac{V_o^2}{(R_l + Z_o)^2} - \frac{V_o^2 R_l}{(R_l + Z_o)^2} = 0 \tag{B.4}$$

Maximum power is obtained when the impedance is matched, i.e. $R_l = Z_o$. This yields the following relations

$$I_l = \frac{V_o}{2Z_o} \; ; \; P_l = \frac{V_o^2}{4Z_o} \; ; \; W_l = \frac{V_o^2}{4Z_o} \tau \tag{B.5}$$

$$\tau = 2n\sqrt{LC} \tag{B.6}$$

where n is the number of stages and τ is the pulse length.

B.2 PFN Construction

When the load impedance is equal to the line impedance there are no reflections and all of the energy stored in the capacitors is dissipated in the load during the first pulse cycle. The three design parameters of particular interest are thus the PFN impedance, the current across the load and the pulse length necessary to establish quasi-steady operation. As discussed in Chapter 2, a 50 kA current pulse is necessary to keep the ion Larmor radius smaller than the dimensions of the outer electrodes (for singly ionized Ga). If we conservatively assume an arc impedance of 10 mΩ, this yields a minimum charging voltage of 1 kV. Electrolytic capacitors

have extensively been used in MPD thrusters (e.g. Ref. [87]) and are not capable of charging voltages in this range and are also characterized by having large internal resistances.

The capacitors chosen have a capacitance of 88 μF with a maximum charging voltage of 1200 V. These capacitors were chosen due to their relatively high capacitance (for an oil-filled dielectric) and their low cost. While oil-filled capacitors are characterized by low equivalent series resistance (ESR) values, they typically have high parasitic inductance values (e.g. $>$ 100 nH), which can have a detrimental effect on the current pulse rise time. This effect was minimized, to a certain degree, by connecting each PFN line in parallel as shown in Fig B.4. Copper rods with a diameter of 1/8" was used as the stage inductors. The inductance can be calculated from [88]

$$L = 0.002l\left(\log\frac{2l}{(rd)^{1/2}} + \frac{7}{8}\right) \tag{B.7}$$

where d is the separation distance between the copper rod and ground plane and l is the inductor length. The ground plane is constructed of a 4 $\times$ 3 ft copper sheet with punched holes to accommodate the terminals of the capacitor. Before running high-powered tests, it was decided to investigate operation with a charging voltage of 3 V. Two 1.5 V batteries connected in series were used to charge the capacitors, and the switch was made by using two copper sheets sandwiched with a insulating Teflon sheet. A nail was hammered through the copper and Teflon sheets, effectively shorting the terminal leads and creating a "fast switch". The results of the 3 V tests along with PSPICE simulations are shown in Fig. B.2. The PSPICE simulations along with an experimental current pulse are shown in Fig. B.3. It can be seen that the experimental discharge current is not quite flat; this was thought to be due to a skin depth effect in the inductors. However, adding a second copper rod did not have a noticeable effect on the discharge current.

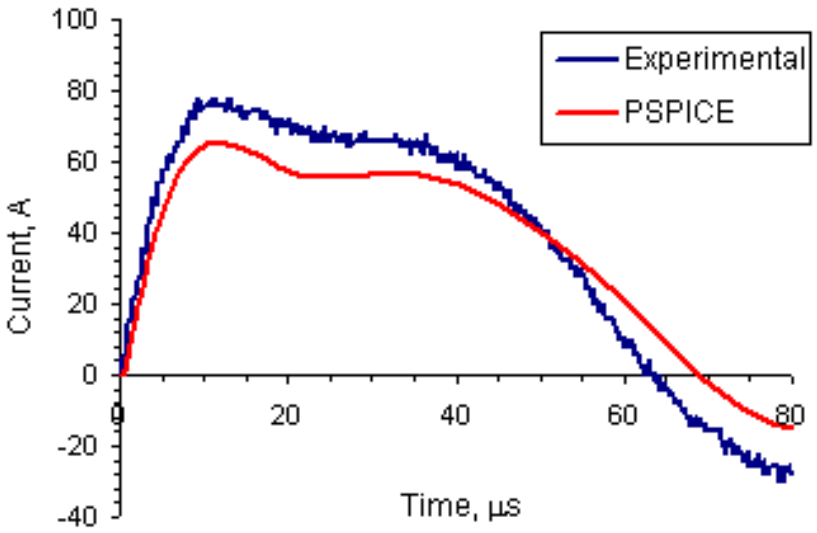

Figure B.2: Comparison of low energy PSPICE and experimental current pulse.

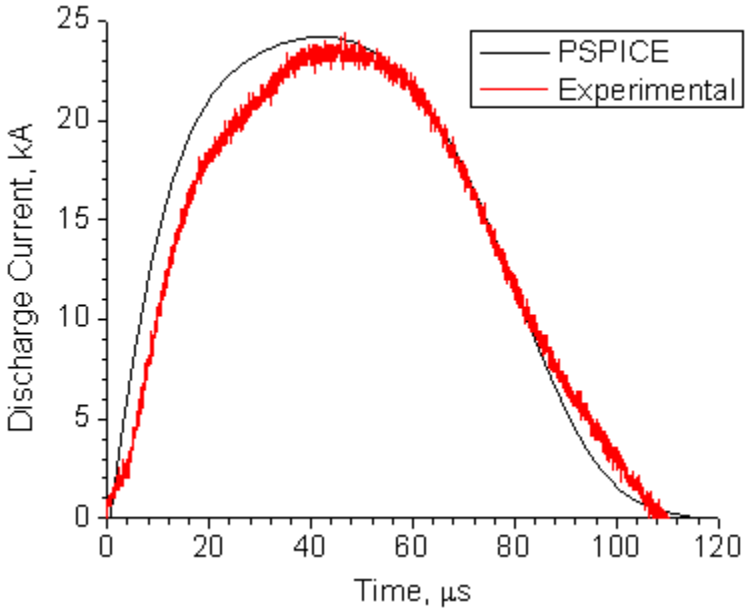

Figure B.3: Comparison of PSPICE and experimental current pulse for a charging voltage of 350 V.

The PSPICE circuit values used for the simulations are shown in Table B.2.

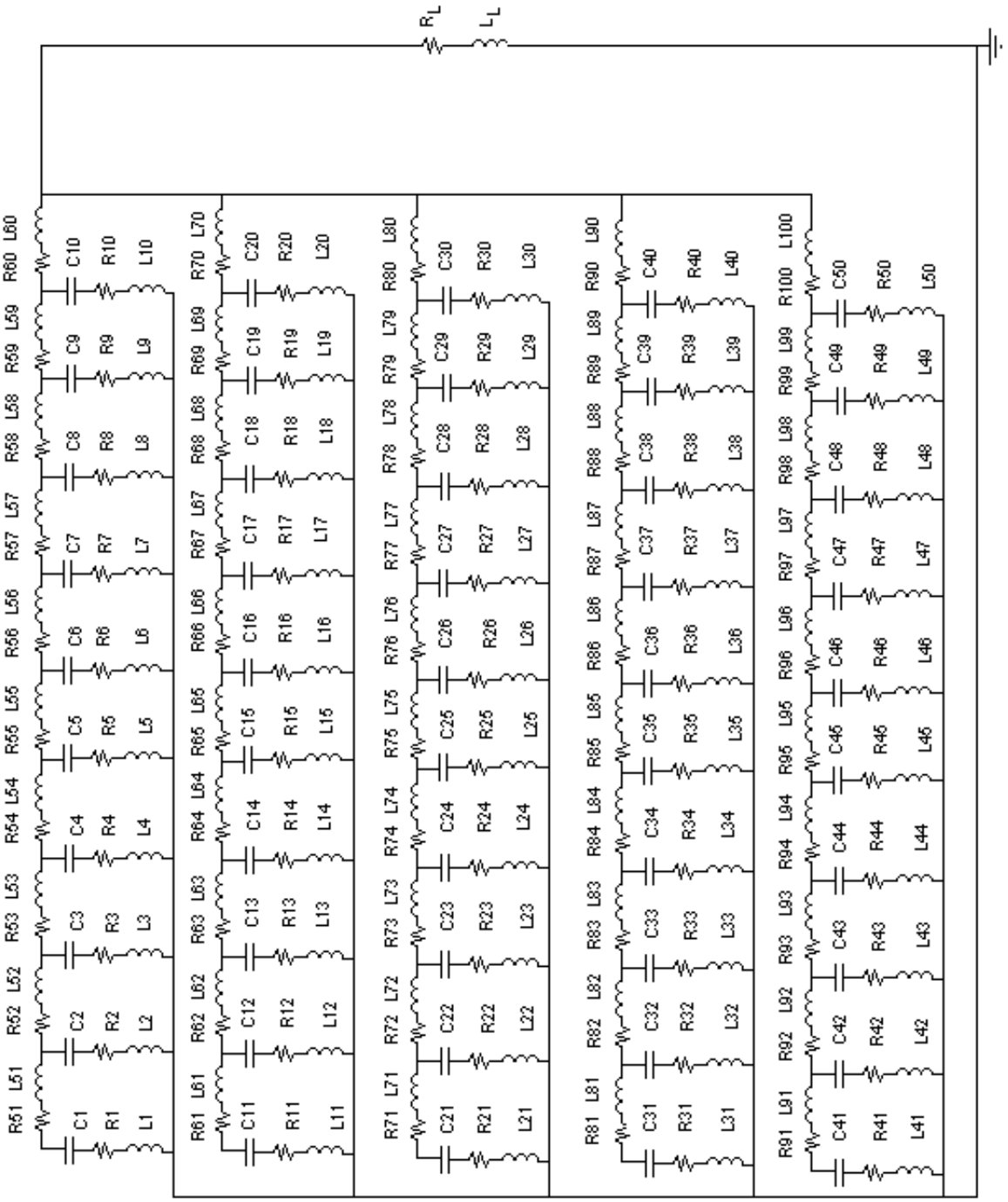

Figure B.4: PSPICE schematic of 5 parallel line PFN.

Table B.1: Numerical values of PSPICE circuit elements.

Component	Description	Value
C1 - C50	Capacitor Capacitance	88 μF
L1 - L50	Capacitor Inductance	160 nH
L51 - L100	Stage Inductance	90 nH
L_L	Thruster Inductance	80 nH
R1 - R50	Capacitor Resistance	2 mΩ
R51 - R100	Inductor Resistance	0.2 mΩ
R_L	Thruster Resistance	7 mΩ

Appendix C

Cathode Spot Model Equations

C.1 Thermofield Emission

In this chapter, the thermofield and heat conduction equations used in the cathode model are discussed. The thermofield current density j_{tf} in terms of the electric field E and surface temperature T_s is calculated using [77]

$$j_{tf} = e \int_{eV_{band}}^{\infty} N(T_s, \epsilon) D(E, \epsilon) \, \mathrm{d}\epsilon \tag{C.1}$$

where $N(T_s, \epsilon)$ is the electron supply function, $D(E, \epsilon)$ is the electron tunneling probability, and ϵ is the electron energy normal to the surface. In the limit of $T_s \to 0$, Eqn. (C.1) reduces to the often-used Richardson-Duschman equation

$$j_{RD} = \frac{4\pi m_e k^2 e}{h^3} T_s^2 \exp\left(-\frac{e\phi_{eff}}{kT_s}\right) \tag{C.2}$$

where the work function ϕ_w is modified by the Schottky potential

$$\phi_{eff} = \phi_w - \sqrt{\frac{eE}{4\pi\epsilon_o}} \tag{C.3}$$

In the limit of $T_s \to 0$, Eqn. (C.1) reduces to the Fowler - Nordheim equation

$$j_{FN} = \frac{e^3 F^2}{8\pi h \phi_w} \exp\left(\frac{-4\sqrt{2m_e\phi_w^3}}{3heE}\right) \tag{C.4}$$

The Fowler - Nordheim equation (low surface temperatures) is obviously not applicable to

studies involving cathode spots, and the Richardson-Duschman equation can lead to errors in the calculated thermofield current density, as shown in Fig. (). While the RD equation follows the same , it underpredicts the emitted density by a factor of two. Equation C.1 is therefore used to calculate the thermofield emission. The full mathematical theory of thermofield emission is given in Ref. [77]; the equations used are now presented.

$$\begin{aligned} j_{tf} &= e\int_{-\infty}^{\infty} N(T_s,\epsilon)D(E,\epsilon) \\ &= \frac{4\pi m_e e k T_s}{h^3}\int_{-\epsilon_a}^{\epsilon_l} \frac{\ln(1+\exp[(\phi_w-\epsilon)/(kT_s)])}{1+\exp\left(\frac{8\pi(2m_e)^{1/2}v(y)\epsilon^{1/2}}{3he}\right)} \\ &+ \frac{4\pi m_e e k T_s}{h^3}\int_{\epsilon_l}^{\infty} \ln(1+\exp[(\phi_w-\epsilon)/(kT_s)])\ \mathrm{d}\epsilon \end{aligned} \tag{C.5}$$

$$y \equiv \sqrt{\frac{e^3 E}{4\pi\epsilon}}\frac{1}{\phi_w} \tag{C.6}$$

where ϵ is the difference between the electron energy and the reference energy at the Fermi level. The electron supply function is expressed by $N(T_s,\epsilon)$, and $D(F,\epsilon)$ is the emission probability. The elliptical function $v(y)$ is numerically equal to

$$v(y) \approx \begin{cases} -\sqrt{\frac{y}{2}}[-2L(k_1)+(1+y)K(k_1)] & \text{if } y \geq 1, \\ \sqrt{1+y}[L(k_2)-K(k_2)] & \text{if } y \leq 1. \end{cases} \tag{C.7}$$

and

$$L(k) = \int_0^{\pi/2}(1-k^2\sin^2\theta)^{1/2}\ \mathrm{d}\theta \tag{C.8}$$

$$K(k) = \int_0^{\pi/2} (1 - k^2 \sin^2 \theta)^{-1/2} \, \mathrm{d}\theta \tag{C.9}$$

$$k_1 = \left(\frac{y-1}{2y}\right)^{1/2} \text{ and } \left(\frac{1-y}{1+y}\right)^{1/2} \tag{C.10}$$

C.1.1 Thermofield Cooling

The electrons emitted from the cathode surface have an average energy

$$\varepsilon_{not} = \frac{e}{j_{tf}} \int_{-\infty}^{\infty} \epsilon P(\epsilon, T_s, E, \phi_w) \, \mathrm{d}\epsilon + \phi_w \tag{C.11}$$

where

$$P(\epsilon, T_s, E, \phi_w) = \int_{-\infty}^{\epsilon} N(T_s, \epsilon) D(E, \epsilon) \, \mathrm{d}\epsilon \tag{C.12}$$

Paulini et. al [89] proposed fit formulas that reduce Eqn. C.11 to a simple analytical form for a wide range of temperatures, field strengths, and work functions. The results are in terms of T^*, the so-called inversion temperature. For surface temperatures below the inversion temperature the cathode is heated (high field strengths, low surface temperatures), whereas it is cooled for T_s ¿ T^*. For the conditions typically found in cathode spots, T_s ¿ $T*$, and the cathode is cooled by thermofield emission. The inversion temperature is given by

$$T^* = w_1 \frac{E^{w_2}}{\phi_w^{w_3}} \left(1 + \frac{w_4}{\phi_w^{w_5}} \left(1 + \tanh\left(w_6 \frac{E^{w_7}}{\phi_w^{w_8}} - w_9\right)\right)\right) \tag{C.13}$$

where the curve-fit parameters are given by

$$w_1 = 7.1130 \times 10^{-7} \quad w_2 = 0.98604$$
$$w_3 = 0.47483 \quad w_4 = 1.0296$$
$$w_5 = 0.91905 \quad w_6 = 4.8022$$
$$w_7 = 8.8832 \times 10^{-2} \quad w_8 = 0.15358$$
$$w_9 = 30.371$$

The approximation formula is

$$\varepsilon_{fit} = a\left(\frac{\pi^2 k}{e}\right)(T_s - T^*)(1-\vartheta) + \left(\frac{2k}{e}T_s + b\right)\vartheta \tag{C.14}$$

$$\vartheta = \frac{p^2}{1+p^s} \text{ and } p = c\left(\frac{T}{T_s} - 1\right) \tag{C.15}$$

where k is Boltzmann's constant, e is the fundamental charge and the parameters a, b, c, and s are given by

$$a = 1 - 1.03104 \times 10^{-2} E^0.193326/\phi_w^0.821433$$
$$b = \phi_w - 1.99435 \times 10^{-5} E^0.533739$$
$$c = 0.687365/\phi_w^0.0525966$$
$$s = 3.48481$$

References

[1] Jahn, R. G., *Physics of Electric Propulsion*, McGraw-Hill Book Company, 1968.

[2] Toki, K., Shimizu, Y., and Kuriki, K., "Application of MPD Thruster Systems to Interplanetary Missions," *Journal of Propulsion and Power*, Vol. 2, No. 6, 1986, pp. 508–512.

[3] Gilland, J., McGuire, M., Corle, T., and Clem, M., "Mission Performance of High-Power Electromagnetic Thruster Systems," *AIP Conference Proceedings*, No. 813, 2006, pp. 201–8.

[4] Jones, R., "Applications of an MPD Propulsion System," *SAE, and ASME, Joint Propulsion Conference*, 1980, pp. AIAA–1980–1225.

[5] LaPointe, M. and Pencil, E., "NASA GRC High Power Electromagnetic Thruster Program," *AIP Conference Proceedings*, No. 699, 2004, pp. 388–98.

[6] Kodys, A., Emsellem, G., Cassady, L., Polk, J., and Choueiri, E., "Lithium Mass Flow Control for High Power Lorentz Force Accelerators," *Proc. Space Tech. and Intnl Forum (STAIF) 2001, AIP Conf. Proc.,*, Vol. 552, 2001, p. 908.

[7] Connolly, D., Sovie, R., Michels, C., and Burkhart, J., "Low Environmental Pressure MPD Arc Tests," *AIAA Journal*, Vol. 6, No. 7, 1968, pp. 1271.

[8] Hyman, J., Bayless, J., Schnelker, D., Ward, J., and Simpkins, J., "Development of a Liquid Mercury Cathode Thruster System," *Journal of Spacecrafts and Rockets*, Vol. 8, No. 7, 1971, pp. 717.

[9] Kami, S., King, H., and Molitor, J., "System Concepts for a Liquid Mercury Cathode Thruster," *Journal of Spacecrafts and Rockets*, Vol. 5, No. 8, 1968.

[10] Collett, C., Dulgeroff, C., and Simpkins, J., *Cesium Microthruster System*, aiaa-1969-292 ed., 1969.

[11] Tajmar, M., Genovese, A., and Steiger, W., "Indium Field Emission Electric Propulsion Microthruster Experimental Characterization," *Journal of Propulsion and Power*, Vol. 20, No. 2, 2004, pp. 211.

[12] Tverdokhlebov, S., Semenkin, A., and Polk, J., "Bismuth Propellant Option for Very High Power TAL Thruster," *40th AIAA Aerospace Sciences Meeting*, 2002, pp. AIAA–2002–348.

[13] Sengupta, A. et al., "An overview of the VHITAL Program: a Two-Stage Bismuth Fed Very High Specific Impulse Thruster with Anode Layer," *29th International Electric Propulsion Conference*, 2005.

[14] Polzin, K. and Markusic, T., "Electromagnetic Pumps for Liquid Metal-Fed Electric Thrusters," *Journal of Propulsion and Power*, Vol. 23, No. 6, 2007.

[15] Doi, T., "A MPD Thruster with Liquid Metal Injection," Tech. rep., The Institute of Space and Astronautical Science, Report No. 610, 1984.

[16] Ducati, A. and Jahn, R., "Investigation of Pulsed Quasi-Steady MPD Arc Jets," Tech. rep., NASA Langley Research Center, 1971.

[17] Burkhardt, L. and Lovberg, R., "Current Sheet in a Coaxial Plasma Gun," *Phys. Fluids*, Vol. 5, 1962, pp. 341.

[18] Cheng, D., "Plasma Deflagration and the Properties of a Coaxial Plasma Deflagration Gun," *Nuclear Fusion*, Vol. 10, 1970, pp. 305–17.

[19] Laystrom, J. and Burton, R., "Geometric Optimization of a Coaxial Pulsed Plasma Thruster," *39th AIAA/ASME/SAE/ASEE Joint Propulsion Conference*, 2003, pp. AIAA Paper 2003–5025.

[20] Ziemer, J., Choueiri, E., and Birx, D., "Trends in Performance Improvements of a Coaxial Gas-Fed Pulsed Plasma Thruster," *25th International Electric Propulsion Conference*, 1997, pp. IEPC–97–040.

[21] Polk, J., Tikhonov, V., Semenikhin, S., and Kim, V., "Cathode Temperature Reduction by Addition of Barium in High- Power Lithium Plasma Thrusters," *AIP Conference Proceedings*, Vol. 504, 2000, p. 1556.

[22] Burton, R., Clark, K., and Jahn, R., "Measured Performance of a Multimegawatt MPD Thruster," *Journal of Spacecrafts and Rockets*, Vol. 20, No. 3, 1983, pp. 299–304.

[23] Paccani, G., Chiarotti, U., and Deininger, W., "Quasisteady Ablative Magnetoplasmadynamic Thruster Performance with Different Propellants," *Journal of Propulsion and Power*, Vol. 14, No. 2, 1998, pp. 254–60.

[24] Choueiri, E. and Ziemer, J., "Quasi-Steady Magnetoplasmadynamic Thruster Performance Database," *Journal of Propulsion and Power*, Vol. 17, No. 5, 2001, pp. 967–976.

[25] Boyle, M., Clark, K., and Jahn, R., "Flowfield Characteristics and Performance Limitations of Quasi-Steady Magnetoplasmadynamic Accelerators," *AIAA Journal*, Vol. 14, No. 7, 1976, pp. 955–962.

[26] Alfvén, H., "Collision between a Nonionized Gas and a Magnetized Plasma," *Rev. Mod. Phys.*, Vol. 32, No. 4, Oct 1960, pp. 710–713.

[27] Burton, R., "The Importance of Alfven's Critical Velocity for MPD Arcs," *8th AIAA Electric Propulsion Conference*, 1970.

[28] Turchi, P., "Another Look at Critical Speed for Self-Field Plasma Thrusters," *18th International Electric Propulsion Conference*, 1985, pp. AIAA–1985–2036.

[29] Choueiri, E., Kelly, A., and Jahn, R., "The Manifestation of Alfven's Hypothesis of Critical Ionization Velocity in the Performance of MPD Thrusters," *18th International Electric Propulsion Conference*, 1985, pp. AIAA–1985–2037.

[30] Clark, K. and Jahn, R., "Quasi-Steady Plasma Acceleration," *AIAA Journal*, Vol. 8, No. 2, 216-220 1970.

[31] Frus, J., "http://www.unisonindustries.com/ourproducts/turbineignition.html," Accessed 10 July 2010.

[32] Luebbers, P. and Chopra, O., "Compatibility of ITER candidate materials with static gallium," Tech. rep., Argonne National Lab., IL., 1995.

[33] Collier, R. and Scott, D., "Cathode Geometry and Spoke Mode Operation of MPD Accelerators," *AIAA Journal*, Vol. 13, 1975, pp. 944–5.

[34] Kribel, R., Eckdahl, C., and Lovberg, R., "Properties of the Rotating Spoke in an Unstable Pulsed MPD Arc," *AIAA Journal*, Vol. 9, 1971, pp. 893–899.

[35] Boxman, R. L., Haber, D., and Martin, P. J., *Handbook of Vacuum Arc Science & Technology: Fundamentals and Applications (Materials Science and Process Technology Series)*, Noyes Publications, 1995.

[36] Langmuir, I., "The Vapor Pressure of Metallic Tungsten," *Physical Review*, Vol. 2, No. 5, 1913, pp. 329–342.

[37] Tilley, D., Choueiri, E., Kelly, A., and Jahn, R., "Microinstabilities in a 10-Kilowatt Self-Field Magnetoplasmadynamic Thruster," *Journal of Propulsion and Power*, Vol. 12, 1996, pp. 381–389.

[38] Eckman, R., Byrne, L., Gatsonis, N., and Pencil, E., "Triple Langmuir Probe Measurements in the Plume of a Pulsed Plasma Thruster," *Journal of Propulsion and Power*, Vol. 17, No. 4, 2001, pp. 762–771.

[39] DelMedico, S. and Burton, R., "Application of a Quadruple Probe Technique to MPD Thruster Plume Measurements," *Journal of Propulsion and Power*, Vol. 9, No. 5, 1996, pp. 771–77.

[40] Tilley, D., Kelly, A., and Jahn, R., "The Application of the Triple Probe Method to MPD Thruster Plumes," *21st International Electric Propulsion Conference*, 1990, pp. AIAA–90–2667.

[41] Chen, S.-L. and Sekiguchi, T., "Instantaneous DirectDisplay System of Plasma Parameters by Means of Triple Probe," *J. Appl. Phys.*, Vol. 36, 1965, pp. 2363.

[42] Chen, S.-L., "Studies of the Effect of Ion Current on Instantaneous Triple Probe Measurements," *J. Appl. Phys.*, Vol. 42, 1971, pp. 406–412.

[43] Peterson, E. and Talbot, L., "Collisionless Electrostatic Single-Probe and Double-Probe Measurements," *AIAA Journal*, Vol. 8, No. 12, 1970.

[44] Laframboise, J., "Theory of Cylindrical and Spherical Langmuir Probes in a Collisionless Plasma at Rest," Tech. rep., ITIAS Report No. 100, 1966.

[45] Kanal, M., "Theory of Current Collection of Moving Cylindrical Probes," *J. Appl. Phys.*, Vol. 35, 1964, pp. 1697.

[46] Poissant, G. and Dudeck, M., "Velocity profiles in a rarefied argon plasma stream by crossed electrostatic probes," *J. Appl. Phys.*, Vol. 58, No. 5, 1985, pp. 1772–79.

[47] Bruce, C. and Talbot, L., "Cylindrical Electrostatic Probes at Angles of Incidence," *AIAA Journal*, Vol. 13, No. 9, 1975, pp. 1236–38.

[48] Kesaev, I., "Laws Governing the Cathode Drop and the Threshold Currents in an Arc Discharge on Pure Metals," *Sov. Phys. - Tech. Phys.*, Vol. 9, 1965, pp. 1146–54.

[49] Laud, B., *Electromagnetics*, New Age International Publishers, 1987.

[50] Boxman, R. and Goldsmith, S., "Macroparticle Contamination in Cathodic Arc Coatings. Generation, Transport and Control," *Surface and Coatings Technology*, Vol. 52, 1992, pp. 39–50.

[51] Kelly, A. and Jahn, R., "Cathode Phenomena in a Low Power, Steady State MPD Thruster," *AIAA-88-3206*, 1988.

[52] Ralchenko, Y., Kramida, A., and Reader, J., "http://physics.nist.gov/asd," Accessed 22 April 2009.

[53] Spitzer, L., *Physics of Fully Ionized Gases: Second Revised Edition*, Dover Books on Physics, 2006.

[54] Myers, R., "Energy Deposition in Low Power Coaxial Plasma Thrusters," *IEPC-88-024*, 1988.

[55] Maisenhalder, F. and Mayerhofer, W., "Jet Diagnostics of a Self-Field Accelerator with Langmuir Probes," *AIAA Journal*, 1974, pp. 1203–1209.

[56] Boxman, R., "Interferometric Measurement of Electron and Vapor Densities in a High-Current Vacuum Arc," *J. Appl. Phys.*, 1974, pp. 4835–4846.

[57] Puchkarev, V., "Estimating the Electron Temperature from Fluctuations in a Vacuum Arc Plasma: Cathode Spot Operation on a Contaminated Surface," *J. Phys. D: Appl. Phys.*, Vol. 24, 1991.

[58] Sherman, J., Webster, R., and Holmes, R., "Cathode Spot Motion in a High Current Vacuum Arc on Copper," *J. Phys. D: Appl. Phys.*, Vol. 8, 1975, pp. 696.

[59] Coleman, H. and Steele, W., *Experimentation and Uncertainty Analysis for Engineers*, Wiley-Interscience, 1989.

[60] Figliola, R. and Beasley, D., *Theory and Design for Mechanical Measurements*, John Wiley and Sons, Inc., 1991.

[61] Rowe, R., von Jaskowsky, W., Clark, K., and Jahn, R., "Erosion Measurements on Quasi-Steady MPD Thrusters," *AIAA-81-0687*, 1981.

[62] Polk, J., von Jaskowsky, W., Kelly, A., and Jahn, R., "Measurement of MPD Thruster Erosion Using Surface Layer Activation," *Journal of Propulsion and Power*, Vol. 3, 1987, pp. 33–37.

[63] Schrade, H., Auweter-Kurtz, M., and Kurtz, H., "Cathode Erosion Studies on MPD Thrusters," *AIAA Journal*, Vol. 25, 1987, pp. 1101–12.

[64] Meunier, J. and Coulombe, S., "Cold Cathode Arc Attachment: The Importance of the High Local Pressure," *Pure & Appl. Chem.*, Vol. 70, 1998, pp. 1175–1180.

[65] Kesaev, I., *Cathode Processes in the Mercury Arc*, New York: Consultants Bureau, 1964.

[66] Paranin, S., Polishchuk, V., Sychev, P., Shabashov, V., and Yartsev, I., "Thermal Conditions in a Hot Evaporating Cathode in a Stationary Vacuum Arc with Diffuse Cathode Emission," *High Temperature*, 1986.

[67] Harris, L., *Vacuum Arc, Theory and Application*, Wiley, 1980.

[68] Djakov, B. and Holmes, R., "Cathode Spot Division in Vacuum Arcs with Solid Metal Cathodes," *J. Phys. D: Appl. Phys.*, Vol. 4, 1971, pp. 504–9.

[69] Taylor, G., "Disintegration of Water Droplets in an Electric Field," *Proc. R. Soc. London Ser. A*, Vol. 280, 1964.

[70] Lee, T. and Greenwood, A., "Theory for the Cathode Mechanism in Metal Vapor Arcs," *J. Appl. Phys.*, Vol. 32, 1961, pp. 916–923.

[71] Coulombe, S. and Meunier, J., "Arc-Cold Cathode Interactions: Parametric Dependence on Local Pressure," *Plasma Sources Sci. Technol.*, Vol. 6, 1997, pp. 508–517.

[72] Lu, J., Krier, H., Burton, R., and Goodfellow, K., "Cathode Sheath Voltage Models for Hydrazine Arcjets," *Journal of Thermophysics and Heat Transfer*, Vol. 12, No. 2, 1998, pp. 230–238.

[73] Fujita, K., "Performance Computation of a Low-Power Hydrogen Arcjet," *AIAA-96-3183*, 1996.

[74] Subramaniam, V. and Hoyer, K., "Limits on Steady Diffuse Mode Operation of the Cathode in Magnetoplasmadynamic Thrusters," *Journal of Propulsion and Power*, Vol. 7, 1991, pp. 565–572.

[75] Bohm, D., *The Characteristics of Electrical Discharges in Magnetic Fields*, New York: MacGraw-Hill, 1949.

[76] Prewett, P. and Allen, J., "The Double Sheath Associated with a Hot Cathode," *Proc. R. Soc. A.*, Vol. 348, 1976, pp. 435.

[77] Murphy, E. and Good, R., "Thermionic Emission, Field Emission, and the Transition Region," *Physical Review*, Vol. 102, 1956, pp. 1464–1473.

[78] Knudsen, M., "Die maximale verdampfungsgeschwindigkeit des quecksilbers," *Ann. Phys. Chem.*, Vol. 47, 1915, pp. 511–525.

[79] Beilis, I. I., "Kinetics of Plasma Particles and Electron Transport in the Current-Carrying Plasma Adjacent to an Evaporating and Electron Emitting Wall," *IEEE Transactions on Plasma Science*, Vol. 34, No. 3, 2006, pp. 855–866.

[80] Mackeown, S., "The Cathode Drop in an Electric Arc," *Physical Review*, Vol. 34, 1929, pp. 611.

[81] Anders, A., Brown, I., MacGill, R., and Dickenson, M., "'Triggerless' Triggering of Vacuum Arcs," *J. Phys. D: Appl. Phys.*, Vol. 31, 1998.

[82] Pearse, R. and Gaydon, A., *The Identification of Molecular Spectra*, Chapman and Hall, 1976.

[83] Howatson, A., *An Introduction to Gas Discharges*, Pergamon Press, 1965.

[84] Yalcin, S., Crosley, D., and Faris, G., "Influence of Ambient Conditions on the Laser Air Spark," *Appl. Phys. B.*, Vol. 68, 1999, pp. 121–130.

[85] Griem, H., *Plasma Spectroscopy*, McGraw-Hill, 1964.

[86] Glascoe, G. and Lebacqz, J., *Pulse Generators*, McGraw-Hill, 1948.

[87] Wilbur, P., "Electrolytic Capacitor Current Pulse Networks for Quasi-Steady MPD Arcs," *AIAA Journal*, Vol. 9, 1971, pp. 1447–1451.

[88] Grover, F. W., *Inductance Calculations: Working Formulas and Table*, New York: Dover, 1962.

[89] Paulini, J., Klein, T., and Simon, G., "Thermo-field Emission and the Nottingham Effect," *J. Phys. D: Appl. Phys.*, Vol. 26, 1993, pp. 1310–15.